

## INFORMATION TO USERS

This material was produced from a microfilm copy of the original document. While the most advanced technological means to photograph and reproduce this document have been used, the quality is heavily dependent upon the quality of the original submitted.

The following explanation of techniques is provided to help you understand markings or patterns which may appear on this reproduction.

1. The sign or "target" for pages apparently lacking from the document photographed is "Missing Page(s)". If it was possible to obtain the missing page(s) or section, they are spliced into the film along with adjacent pages. This may have necessitated cutting thru an image and duplicating adjacent pages to insure you complete continuity.
2. When an image on the film is obliterated with a large round black mark, it is an indication that the photographer suspected that the copy may have moved during exposure and thus cause a blurred image. You will find a good image of the page in the adjacent frame.
3. When a map, drawing or chart, etc., was part of the material being photographed the photographer followed a definite method in "sectioning" the material. It is customary to begin photoing at the upper left hand corner of a large sheet and to continue photoing from left to right in equal sections with a small overlap. If necessary, sectioning is continued again — beginning below the first row and continuing on until complete.
4. The majority of users indicate that the textual content is of greatest value, however, a somewhat higher quality reproduction could be made from "photographs" if essential to the understanding of the dissertation. Silver prints of "photographs" may be ordered at additional charge by writing the Order Department, giving the catalog number, title, author and specific pages you wish reproduced.
5. PLEASE NOTE: Some pages may have indistinct print. Filmed as received.

**University Microfilms International**

300 North Zeeb Road  
Ann Arbor, Michigan 48106 USA  
St. John's Road, Tyler's Green  
High Wycombe, Bucks, England HP10 8HR

77-23,483

BAIRD, Ronald J., 1946-  
ANGULAR-DEPENDENT X-RAY PHOTOELECTRON  
SPECTROSCOPY OF SOLIDS.

University of Hawaii, Ph.D., 1977  
Chemistry, physical

**Xerox University Microfilms**, Ann Arbor, Michigan 48106

ANGULAR-DEPENDENT X-RAY PHOTOELECTRON  
SPECTROSCOPY OF SOLIDS

A DISSERTATION SUBMITTED TO THE GRADUATE DIVISION  
OF THE UNIVERSITY OF HAWAII IN PARTIAL FULFILLMENT  
OF THE REQUIREMENTS FOR THE DEGREE OF  
DOCTOR OF PHILOSOPHY  
IN CHEMISTRY  
MAY 1977

By

Ronald J. Baird

Dissertation Committee:

Charles S. Fadley, Chairman  
George Andermann  
Thomas T. Bopp  
Burton L. Henke  
Karl Seff

## ACKNOWLEDGEMENTS

I would like to acknowledge the assistance of P. F. Heden who carried out the initial design of the Hewlett-Packard compatible sample probe, J. Gulden who provided guidance and programming assistance in the computer interfacing, P. J. Feibelman and M. Sunjic who provided theoretical results used in the aluminum plasmon studies, J. D. Tuthill and R. E. Johnson in deriving the total intensity contours, and J. A. Schoeffel in performing LEED measurements on the gold single crystal.

I would also like to express my gratitude to the National Science Foundation for their support of this work through grants GP38640X and MPS7505055, to Professor C. S. Fadley for his guidance and encouragement, and to my colleagues in the Chemistry Department at the University of Hawaii.

ANGULAR-DEPENDENT X-RAY-PHOTOELECTRON  
SPECTROSCOPY OF SOLIDS

By

Ronald J. Baird  
Department of Chemistry

A Dissertation Submitted to the Graduate Division  
of the University of Hawaii in Partial Fulfillment of  
the Requirements for the Degree of  
Doctor of Philosophy

Abstract

The angular dependence of x-ray-photoelectron spectra has been investigated for both polycrystalline and single crystal samples. Also, certain instrumental aspects of performing such angle-resolved measurements are discussed.

All experimental spectra were obtained with a modified Hewlett-Packard 5950A photoelectron spectrometer. This spectrometer utilizes a monochromatized AlK $\alpha$  x-ray source and incorporates dispersion compensation for the x-ray linewidth. The instrument modifications which are discussed include: (1) The construction of a special sample probe that is compatible with the standard Hewlett-Packard inlet system, but which allows rotation of the sample about two axes. (2) The construction of a complete new sample inlet system which replaces the standard sliding-seal system with a bakeable all-metal bellows for linear motion. This sample inlet system allows for true ultrahigh vacuum operation as well as two-axis rotation of the sample and heating to 1200°C and cooling to liquid nitrogen temperatures. (3) The modification of the operation of the

electrostatic lens which forms part of the dispersion-compensating optics in order to improve resolution and sensitivity under certain operating conditions. This modification of the lens operation is part of a systematic study of the effects on resolution and sensitivity of variation of the sample position in a dispersion compensating spectrometer.

Several aspects of the enhancement of the surface sensitivity of x-ray photoelectron spectroscopy, by detecting electrons which escape at near-grazing angles are considered. In a series of experiments on aluminum diffraction gratings with oxide overlayers, the effect of periodic surface roughness on the enhancement of surface sensitivity was measured. The experimental results are found to be in good agreement with a theoretical model which considers only the variation of true electron escape angle from a rough surface and the presence of electron shading by surface contours. Also, the angular dependence of the relative intensities of the bulk and surface plasmon loss peaks associated with the Al2p core level was measured for clean, smooth, polycrystalline aluminum samples. At near-grazing angles of electron escape, a fourfold increase in the surface plasmon relative intensity is observed, while the bulk plasmon relative intensity is decreased by only 20%. For aluminum specimens with low coverages ( $\sim 0.15$  monolayer) of oxygen, only surface plasmon loss features were found associated with the O1s core level. The experimental results are compared to theoretical calculations based on a jellium model including both intrinsic and extrinsic effects.

In measurements of the angular dependence of the photoelectron spectra from a gold single crystal, two effects were studied. The angular dependence of the integrated intensity of the gold core and valence levels show pronounced fine structure. This fine structure is analyzed qualitatively in terms of a diffraction phenomena analogous to the Kikuchi bands observed in low energy electron diffraction and electron transmission experiments. In addition to the total intensity variations, the shapes of the Au5d valence-band spectra show changes which are related to the direction of emission. These changes in shape are analyzed in terms of a direct transition model in which the conservation of wave-vector limits the initial states which can contribute to photoemission in a given direction.

## TABLE OF CONTENTS

Acknowledgements. . . . .	.iii
Abstract. . . . .	iv
List of Tables. . . . .	ix
List of Figures . . . . .	x
I. INTRODUCTION. . . . .	1
II. THEORY. . . . .	10
1. General Photoemission Theory. . . . .	10
2. Macroscopic Effects . . . . .	15
A. Surface Enhancement . . . . .	15
B. Flat Surface Intensity Model. . . . .	17
C. Effect of Overlayers. . . . .	24
D. Effect of Surface Roughness . . . . .	26
E. Angular Dependence of Plasmon Loss Spectra. . . . .	30
3. Microscopic Effects . . . . .	35
A. General Considerations. . . . .	35
B. Total Peak Intensity Variations . . . . .	36
C. Angular Dependence of Valence Band Spectra. . . . .	37
III. EXPERIMENTAL. . . . .	50
1. Instrument Modifications. . . . .	50
2. Electron Optical Calculations . . . . .	52
IV. X-RAY PHOTOELECTRON ANGULAR DISTRIBUTIONS WITH DISPERSION-COMPENSATING X-RAY- AND ELECTRON-OPTICS. . . . .	78
1. Introduction. . . . .	78
2. Theory. . . . .	80
3. Experimental. . . . .	95
4. Results and Discussion. . . . .	.103
5. Conclusions . . . . .	.109
V. DIRECT OBSERVATION OF SURFACE-PROFILE EFFECTS ON X-RAY-PHOTOELECTRON ANGULAR DISTRIBUTIONS . . . . .	.140
VI. PLASMON LOSS EFFECTS. . . . .	.160
1. Introduction. . . . .	.160
2. Theory. . . . .	.163
3. Experimental. . . . .	.167
4. Results and Discussion. . . . .	.170
5. Conclusions . . . . .	.178

VII.	ANGULAR-DEPENDENT X-RAY-PHOTOELECTRON PEAK INTENSITIES FROM SINGLE-CRYSTAL GOLD. . . . .	.195
1.	Introduction. . . . .	.195
2.	Experimental Procedure. . . . .	.196
3.	Results and Discussion. . . . .	.198
	A. Energy Integrated Intensities and Kikuchi Effects . . .	.198
	B. Angular-Dependent Valence Fine Structure. . . . .	.203
4.	Conclusions . . . . .	.207
VIII.	ANGULAR DEPENDENCE OF XPS VALENCE SPECTRA FROM SINGLE-CRYSTAL GOLD. . . . .	.221
IX.	CONCLUSIONS . . . . .	.235

## LIST OF TABLES

Table	Page
III-1 Operating Potentials of Electrostatic Lens . . . . .	53
III-2 Angle of Acceptance and Magnification of Lens as a Function of Kinetic Energy. . . . .	55
IV-1 Physical Parameters of HP-5950A Photoelectron Spectrometer . .	113

## LIST OF FIGURES

II-1	Definition of Angles in XPS Equipment . . . . .	45
II-2	General Spectrometer Geometry . . . . .	47
II-3	An Arbitrary Rough Surface Profile. . . . .	49
III-1	Overall Schematic of Instrument . . . . .	61
III-2	Photograph of Inlet System. . . . .	63
III-3	Photograph of Specimen Probe. . . . .	65
III-4	Photograph of Two-Axis, Variable-Temperature Sample Probe . .	67
III-5	Trajectory Calculations for 1500 eV Electrons in the Electrostatic Lens . . . . .	69
III-6	Trajectory Calculations for 1000 eV Electrons . . . . .	71
III-7	Trajectory Calculations for 500 eV Electrons. . . . .	73
III-8	Trajectory Calculations for 200 eV Electrons. . . . .	75
III-9	Solid Angle of Acceptance of Electrostatic Lens as a Function of Kinetic Energy . . . . .	77
IV-1	Schematic Diagram of Electron- and X-Ray-Optics . . . . .	115
IV-2	Schematic Diagram of Electron Trajectories. . . . .	117
IV-3	A General Spectrometer Geometry . . . . .	119
IV-4	Photograph of Hewlett-Packard Compatible Sample Probe . . .	121
IV-5	Three Views of Sample Rotation Mechanism. . . . .	123
IV-6	Peak Shifts <u>vs.</u> Angle for Monochromator Misalignment. . . .	125
IV-7	X-Ray Flux Perpendicular to Mean X-Ray Propagation Direction.	127
IV-8	Theoretical and Experimental Cls Spectra for Lens Magnification = -5.0. . . . .	129
IV-9	Theoretical and Experimental Cls Spectra for Lens Magnification = -2.3. . . . .	131

IV-10	Variation of Cls Total Intensity with Angle . . . . .	.133
IV-11	Variation of Cls FWHM with Angle. . . . .	.135
IV-12	Variation of Au4f <sub>7/2</sub> Total Intensity with Angle for Various Cases of Monochromator Misalignment . . . . .	.137
IV-13	Cls/Au4f <sub>7/2</sub> Ratio <u>vs.</u> Angle for a Variety of Cases of Misalignment . . . . .	.139
V-1	Al2p(oxide)/Al2p(metal) Ratio <u>vs.</u> Angle for an Oxidized, 10° Blaze-Angle, Aluminum Diffraction Grating . . . . .	.153
V-2	Al2p(oxide)/Al2p(metal) Ratio <u>vs.</u> Angle for a 20° Blaze-Angle Grating . . . . .	.155
V-3	Al2p(oxide)/Al2p(metal) Ratio <u>vs.</u> Angle for a 43° Blaze-Angle Grating . . . . .	.157
V-4	Al2p(oxide)/Al2p(metal) Ratio <u>vs.</u> Angle for an Oxidized, Unidirectionally Polished Aluminum Sample . . . . .	.159
VI-1	Al2p and Associated Loss Peaks at Three Electron Escape Angles . . . . .	.184
VI-2	Theoretical and Experimental Bulk-Loss to No-Loss Peak Area Ratios. . . . .	.186
VI-3	Theoretical and Experimental Surface-Loss to No-Loss Peak Area Ratios. . . . .	.188
VI-4	O1s Spectra from 0.15 Monolayers of Oxygen Chemisorbed on Aluminum . . . . .	.190
VI-5	Theoretical One-Bulk-Plasmon Area Ratios as a Function of Emitter Depth . . . . .	.192
VI-6	Theoretical Ratio of Surface-to-Bulk-Plasmon-Loss as a Function of Emitter Depth . . . . .	.194
VII-1	Definition of XPS Experimental Angles . . . . .	.212
VII-2	XPS Total Peak Intensities as a Function of Polar Angle . .	.214
VII-3	Stereographic Projection of Angular Dependence of Au4f XPS Intensity Above a Gold Single Crystal . . . . .	.216

VII-4	Qualitative Predictions of Kikuchi-Band Theory for Au4f Intensity Distribution . . . . .	.218
VII-5	Gold Valence-Band Spectra for Various Emission Angles from a Gold Single Crystal. . . . .	.220
VIII-1	XPS Valence Spectra for Electron Emission Along Various Low-Index Directions from a Gold Single Crystal . . . . .	.232
VIII-2	Comparison of Theoretical and Experimental XPS Valence Spectra from Gold . . . . .	.234

## I. INTRODUCTION

Over the last twenty years, photoelectron spectroscopy has rapidly developed as an experimental technique for probing the electronic structure of matter. The basic experiment is founded on the photoelectric effect which was first explained by Einstein at the turn of the century<sup>1</sup>. In the photoelectron experiment, a nearly monoenergetic beam of photons with energy  $h\nu$  is directed onto the sample of interest. The photons interact with the electrons in the sample, and those electrons which are bound with an energy less than  $h\nu$  can be ejected with some kinetic energy  $E_{\text{kin}}$ . Conservation of energy requires that

$$h\nu = E_{\text{kin}} + E_{\text{b}}^{\text{V}} \quad (\text{I-1})$$

where  $E_{\text{b}}^{\text{V}}$  is the binding energy of the ejected photoelectron as referred to the vacuum level<sup>2</sup>.

Equation I-1 is valid only for gas phase samples and the vacuum level is a natural reference for such samples. For condensed samples in which the sample and spectrometer are in electrical contact, the difference in work function between the sample and the spectrometer must be accounted for. This is usually accomplished by referring the binding energies in solid samples to the Fermi level (electron chemical potential) rather than to the vacuum level. If the sample and spectrometer are in thermodynamic equilibrium, then their electron chemical potentials are equal and their Fermi levels are aligned. Since the work function,  $\phi$ , is defined as the energy difference between the vacuum level and the Fermi level, it can be seen that the appropriate

conservation equation for binding energies referred to the Fermi level,  $E_b^F$ , is given by

$$h\nu = E_{kin} + E_b^F + \phi_{spec} \quad (I-2)$$

where  $\phi_{spec}$  is the work function of spectrometer. The Fermi level reference has the advantage that only the work function of the spectrometer, which tends to remain constant, needs to be accounted for. The work function of the sample can be different for each sample, and for a given sample it tends to vary with sample surface condition. However, if the sample work function,  $\phi_s$ , is known, the binding energies of solid samples can be referred to the vacuum level since

$$E_b^V = E_b^F + \phi_s. \quad (I-3)$$

All of the binding energies in this thesis will be reported relative to the Fermi level and the superscript F will henceforth be dropped.

Historically, photoelectron spectroscopy has tended to be divided into two regimes depending upon the energy range of the exciting photons. Those experiments performed with photon energies of less than 40 eV are generally referred to as ultraviolet photoelectron spectroscopy (UPS), while measurements performed with photons of  $\sim 1000$  eV or more have been classified as x-ray photoelectron spectroscopy (XPS). These ranges of photon energies have been dictated primarily by the availability of monochromatic photon sources. In the UPS region windowed vacuum monochromators have been used below the LiF cutoff ( $\sim 11.6$  eV) and noble gas resonance lines have been used up to 40.8 eV. In the XPS region, the

$K_{\alpha}$  lines of Mg (1254 eV) and Al (1486 eV) are sufficiently intense and narrow ( $\sim 1$  eV) to be used as photon sources. Recent advances, especially the development of synchrotron radiation sources<sup>3</sup> and, to a lesser extent, the use of the Y M $\xi$  (132 eV) and other second transition series x-ray sources<sup>4,5</sup>, have extended the available range of lower energy monochromatic photon sources upward to  $\sim 300$  eV. These developments have tended to blur any clear distinction between XPS and UPS. All of the work done in this thesis will be limited to the XPS regime with AlK $\alpha$  excitation.

Within the XPS regime, a wide variety of information has been derived from analyzing photoelectron kinetic energy distributions,  $N(E_{kin})$ , and relating such distributions to the population of certain bound states and to various mechanisms of electron interaction within the sample. In particular, Fadley has pointed out in a recent review paper that the following types of information are available from  $N(E_{kin})$  distributions<sup>6</sup>:

- 1.) Core level peak intensities can be qualitatively and quantitatively related to the elemental composition of the sample.
- 2.) Shifts in core level binding energies can often be attributed to changes in the chemical environment of the elements in the sample.
- 3.) Certain splittings in core-levels, termed multiplet splittings, can reflect valence-level occupations and the strengths of core-valence interactions.

- 4.) Valence level spectra can be used to probe the energies and makeup of the higher-lying states of molecules or solids.
- 5.) Certain satellite peaks and peak broadening effects, including shake-up and shake off effects, can be used to investigate processes involving the breakdown of a simple one-electron transition model.
- 6.) Inelastic loss features at lower kinetic energies than the no-loss peak give information about low-lying excited states in the specimen.
- 7.) Observed peak widths may be related to vibrational or lifetime broadening effects.

There exists a considerable body of literature discussing the various applications of XPS and several thorough reviews of the subject have appeared<sup>2,7-17</sup>.

Prior to the work reported in this thesis, almost all XPS studies had been performed with a fixed experimental geometry so that the  $N(E_{kin})$  distributions were recorded at fixed angles of x-ray incidence and electron exit from the sample. Very few attempts had been made to measure the angular dependence of  $N(E_{kin})$  and to extract any additional information contained in such angular distributions. In the few prior angle-resolved XPS studies, Siegbahn et al.<sup>18</sup> and Fadley and Bergstrom<sup>19,20</sup> reported pronounced fine structure in the angular distribution of photoelectrons originating from core levels in single crystals of NaCl and Au, respectively. Also, Fadley and Bergstrom<sup>19,20</sup> reported the selective enhancement of the photoelectron signal from carbon overlayers

on gold by detecting those electrons which escaped from the sample at near grazing exit angles. These early angle-resolved measurements provided a strong impetus for attempting to further develop the instrumentation and the theoretical understanding necessary for the performance and interpretation of angle-resolved photoemission experiments.

Subsequent to the start of this work, several other workers have presented angle-resolved x-ray photoemission results<sup>21-25</sup> and Fadley has recently reviewed the current status of angle-resolved XPS<sup>6</sup>. The effects noted in these angle-resolved XPS experiments can in general be divided into microscopic and macroscopic phenomena. The microscopic effects, which include the fine structure noted in the angular dependence of core peak intensities in single crystals and the more recently noted angular dependence of valence band spectra of metal single crystals<sup>26,27</sup>, are related to the long-range crystalline order in the sample. The macroscopic effects are by contrast averages over crystalline orientation, and are manifested primarily in the enhancement of the surface sensitivity of the XPS technique at low angles of electron escape, an effect caused by the short inelastic mean free path for electrons in solids.

This thesis deals with both microscopic and macroscopic effects in XPS angular distribution (AD) studies. In section II, the basic theory necessary for explaining these effects is developed. Sections III and IV deal with various experimental details of high resolution XPS angular distribution studies. Sections V and VI discuss the investigation of macroscopic effects and Sections VII and VIII consider microscopic effects in photoemission from metal single crystals. Section IX summarizes the

results of this work, and evaluates the general importance of AD measurements in XPS.

REFERENCES  
SECTION I

- 1) A. Einstein, *Ann. Phys.* 17, 132 (1905).
- 2) K. Siegbahn et al., Electron Spectroscopy for Chemical Analysis, Nova Acta Regiae Soc. Sci. Upsaliensis, Almqvist and Wiksells, Uppsala, Sweden, 1967, or National Technical Information Service Report No. AD844315, U.S. Department of Commerce.
- 3) D. E. Eastman, in Vacuum Ultraviolet Physics, E. E. Koch, R. Haensel, and C. Kunz, Eds., Pergamon Press, New York, 1974.
- 4) M. O. Krause, *Chem. Phys. Letters* 10, 65 (1971).
- 5) M. S. Banna and D. A. Shirley, *J. Chem. Phys.* 63, 4759 (1975).
- 6) C. S. Fadley, in Progress in Solid State Chemistry, G. Somorjai and J. O. McCaldin, Eds. (Pergamon Press, New York, 1976).
- 7) C. S. Fadley, S. B. M. Hagström, J. M. Hollander, M. P. Klein, and D. A. Shirley, *Science*, 157, no. 3796, 1571 (1967); C. S. Fadley, S. B. M. Hagström, M. P. Klein, and D. A. Shirley, *J. Chem. Phys.* 48, 3779 (1968).
- 8) K. Siegbahn et al., ESCA Applied to Free Molecules, North Holland Publishing Co., Amsterdam, 1971.
- 9) D. A. Shirley, Ed., Electron Spectroscopy, North Holland, Amsterdam, 1972.
- 10) D. A. Shirley, in Advances in Chemical Physics, I. Prigogine and S. A. Rice, Eds., John Wiley, New York, 1973, Volume 23.

- 11) C. S. Fadley, in Electron Emission Spectroscopy, W. Dekeyser et al., Eds., Reidel, Dordrecht, Holland, 1973.
- 12) D. T. Clark, in Electron Emission Spectroscopy, W. Dekeyser et al., Eds., Reidel, Dordrecht, Holland, 1973.
- 13) C. S. Fadley and S. B. M. Hagström, in X-ray Spectroscopy, L. Azaroff, Ed., McGraw Hill, New York, 1974, Chapter 8.
- 14) Journal of Electron Spectroscopy, Volume 5 (1974) or Electron Spectroscopy - Progress in Research and Applications, R. Caudano and J. Verbist, Eds., Elsevier, Amsterdam, 1974.
- 15) C. R. Brundle, J. Vac. Sci. and Tech. 11, 212 (1974).
- 16) D. M. Hercules, Anal. Chem. 44, 106R (1972); W. E. Schwartz, Anal. Chem. 45, 789A (1973); D. M. Hercules and J. C. Carver, Anal. Chem. 46, 133R (1974).
- 17) C. D. Wagner, Anal. Chem. 44, 1050 (1972).
- 18) K. Siegbahn, U. Gelius, H. Siegbahn, and E. Olsen, Phys. Letters 32A, 221 (1970).
- 19) C. S. Fadley and S. Å. L. Bergström, Phys. Letters 35A, 375 (1971).
- 20) C. S. Fadley and S. Å. L. Bergström, in Electron Spectroscopy, D. A. Shirley, Ed., North Holland, Amsterdam, 1972, p.233.
- 21) B. L. Henke, Phys. Rev. A 6, 94 (1972).
- 22) W. A. Fraser, J. V. Florio, W. N. Delgass, and W. D. Robertson, Surf, Sci. 36, 661 (1973).
- 23) J. Brunner and H. Zogg, J. Electron Spectroscopy 5, 911 (1974).

- 24) J. M. Hill, D. R. Royce, C. S. Fadley, and F. Grunthaner, Chem. Phys. Letters 44, 225 (1976) and J. M. Hill, M. S. thesis, Department of Chemistry, University of Hawaii, 1975.
- 25) R. S. Swingle, R. P. Groff, and B. M. Monroe, Phy. Rev. Letters 35, 452 (1975).
- 26) R. J. Baird, L. F. Wagner, and C. S. Fadley, Phys. Rev. Letters 37, 111 (1976).
- 27) F. R. McFeely, J. Stöhr, G. Apai, P. S. Wehner, and D. A. Shirley, Phys. Rev. B 14, 3273 (1976).

## II. THEORY

### 1. General Photoemission Theory

In this section, a qualitative discussion of the various theoretical models used to discuss photoemission is presented. In subsequent sections, certain specializations of these models germane to this thesis are discussed in more detail.

One of the first derivations of a theoretical expression for the energy distribution of photoelectrons excited by photons well above threshold energies was carried out by Berglund and Spicer in 1964<sup>1</sup>. In their theoretical model, they divided the photoemission event into two steps. The first step, which was treated quantum mechanically, involved bulk optical excitation of electrons into states of higher energy. The second step involved transport of the excited electrons to the surface and escape through the surface into the vacuum. This second step (which was, itself, subsequently divided into the two steps of transport and escape) was treated semi-classically. This model became the basis for the semi-classical three-step model for photoemission which has been used with considerable success in interpreting photoemission results.

Within this model, the optical excitation step was treated via a perturbative formalism in which the initial and final states of the electron were taken to be wave functions of the unperturbed solid. In this way, the measured photoelectron energy distributions were thought to reflect in some way the band structure of the solid material under study. The description of the transport step was restricted by the assumptions that: 1) the excited electrons were emitted isotropically,

2) only inelastic scattering was significant, 3) inelastic scattering could be described by a classical mean-free-path, and 4) inelastic scattering was isotropic. The escape step required only that the electron possess sufficient momentum perpendicular to the surface to overcome the surface barrier.

Despite the successes of the three-step model in accounting for many photoemission results, recent theoretical developments have challenged the somewhat arbitrary division of the photoemission process into discrete steps. Caroli et al.<sup>2</sup> have pointed out that, in a more exact treatment, the final states used in calculating the transition matrix elements in the optical excitation must actually account for the presence of the surface and for the matching of the final state in the solid to the outgoing electron wave function in the vacuum. In an earlier paper, Adawi<sup>3</sup> considered the matching conditions and showed that for the surface photo-effect the final state (outgoing wave) was identical to the initial state (incoming wave) in low energy electron diffraction (LEED). Mahan<sup>4</sup> later generalized this result to the case of bulk photoemission from a nearly-free-electron metal in the presence of a surface.

Mahan was the first to consider the angular distribution of the emitted photoelectrons. In his description of the optical transition step, the photon provides the additional energy for the excitation of an electron to a higher energy state, while the crystal potential provides the additional momentum that the electron needs to reach the excited state. Since the crystal potential has the periodicity of the lattice,

the additional momentum can only be supplied in multiples of a reciprocal lattice vector  $\vec{G}$ . It is this quantization of the momentum or, more correctly, wave-vector change that gives rise to the angular dependence of the emitted photoelectrons in Mahan's model. In particular, the simultaneous conservation of energy and wave vector requires that within the crystal all photoelectrons of the same energy be emitted in conical distributions centered on reciprocal lattice vectors. These cones of intensity may be distorted in traversing the surface since the momentum parallel to the surface must be conserved to within the parallel component of a reciprocal lattice vector. This additional conservation requirement gives rise to secondary cones of intensity outside of the crystal.

While Mahan's model does not arbitrarily separate the photoemission process into discrete steps, it still contains certain limitations. In particular, this model does not account for inelastic scattering except in the introduction of a classical mean-free-path into the expression for the photocurrent. Also, the model is directed to the case of a nearly-free-electron metal and the crystal potential is taken to be the sum of screened potentials located on each lattice site. Schaich and Ashcroft<sup>5</sup> have presented a theoretical description of photoemission based on quadratic response theory which they demonstrated to be equivalent to Mahan's formulation. They showed that their results for the photocurrent at a given energy in a given direction could be expressed in a Golden-Rule form in which the photocurrent is expressed as a transition rate from an initial to a final state<sup>6</sup>. The complication in applying their

expression arose in the definition of the final state. Despite this complication, they presented calculations based on several different models of the electronic structure of metals and concluded that photoemission experiments could provide a sensitive test of these models.

More recently Caroli et al.<sup>2</sup> have presented an exact many-body formulation of the photoemission process. In their formalism they utilize non-equilibrium many-body theory to describe the photoemission event and provide the capability of including electron-electron interactions to any order. In this way, it is possible to include inelastic effects directly in the description of the photoemission process. In an attempt to make contact between this theory and experimental measurements, Feibelman and Eastman<sup>7</sup> have focused on the lowest-order application of the formalism by Caroli et al., which corresponds to photoemission from an independent-electron-solid. They have shown that this lowest order approximation can be reduced to a Golden-Rule formula in which the electron final state wave functions are equivalent to the wave functions used in LEED calculations (as was earlier shown by Adawi for the surface photoeffect<sup>3</sup>). Furthermore, they have shown that for sufficiently weak electron damping, i.e., long electron mean-free-path, the Golden-Rule formula that they have derived can be reduced to the semi-classical three-step model. This reduction is possible since the matrix elements for photon excitation in the bulk become the same matrix elements that govern the bulk optical properties of the solid. This ability to recover the three-step model for certain experimental conditions is important in discussion macroscopic effects in XPS

angular distributions which tend to average over any periodicity in the sample.

Also, the distinction that Feibelman and Eastman draw between the UPS or 'band structure' regime and the XPS or weighted 'density of states' regime is significant in describing the microscopic effects observed in angle-resolved XPS experiments. They define the band structure regime to be that region of electron kinetic energy in which the final state momentum broadening (which is inversely proportional to the electron escape depth) is less than the average separation of the available final states. In this regime the electron excitations arise from interband transitions and the energy distribution of emitted electrons reflects the electron joint density of states (EJDOS) which is given by a convolution of the occupied states below the Fermi-level with unoccupied states above the vacuum level. In the XPS limit, the electron-mean-free paths in the solid are large so that momentum broadening is small, however, the density of final states becomes so great at higher energies that final states are available for excitation from essentially all initial states. Each of these transitions will be weighted by a matrix element, and if emission from a polycrystalline specimen is considered, the net result is an energy distribution curve that is a weighted total density of states of the solid. In an approximate calculation for angle-integrated photoemission from a polycrystalline nearly-free-electron solid, they conclude that the transition from the UPS to the XPS regime occurs for photon energies of between 20 eV to 40 eV. However, they are careful to point out that angle-resolved

measurements or measurements on single crystal specimens would greatly reduce the available final state phase space. Thus, band structure effects can persist at higher energies in angle-resolved measurements from single crystals.

Despite these recent theoretical advances, it is still difficult to make useful calculations with the more exact theories due to the need for accurate wave functions and an accurate description of the crystal potential. For example, Schaich and Ashcroft<sup>5</sup> conclude their paper by pointing out that "The results that we have presented above indicate the difficulty of a realistic calculation, even in the independent-particle approximation, of the photoemission from real metals." Therefore, it is still useful to make use of the three-step model, especially in discussing the macroscopic effects in angle-resolved XPS, and to treat the microscopic effects in lowest order by neglecting scattering in calculating band structure effects.

## 2. Macroscopic Effects in Angular Distributions

### A. Surface Enhancement

The basic surface sensitivity of XPS and the possibility for enhancing this sensitivity in angle-resolved XPS are both based on the short inelastic mean-free-path,  $\Lambda_e$ , of low energy electrons in solids. Powell<sup>8</sup> has recently made a compilation of measured electron mean-free-paths for electron energies of less than 2 keV. From this compilation, it can be seen that  $\Lambda_e$  in the kinetic energy region usually encountered in XPS (500 eV - 1500 eV) ranges from about 10 Å to about 40 Å for a wide variety of solid materials. Thus, the elastic or no-loss peak

corresponding to emission normal to the sample surface will be made up of electrons which originated, on the average, from within one mean-free-path or 5 to 15 atomic layers from the surface. However, in the usual approximation of an isotropic or angle-independent attenuation length, the no-loss signal corresponding to emission at near grazing angles will originate on the average from within only  $\Lambda_e \sin\theta$  of the surface, where  $\theta$  is the angle between the electron escape direction and the surface. Thus, for an electron escape angle of  $10^\circ$ , the no-loss signal will originate mostly within the top 2 or 3 atomic layers.

This surface enhancement effect can be treated more quantitatively in terms of a model first presented by Henke<sup>9</sup>, later extended by Fraser et al.<sup>10</sup> and most recently expanded by Fadley et al.<sup>11,12,13,14</sup> to include certain instrumental effects and the influence of surface roughness. This treatment is based on the three-step model of photoemission, and the surface enhancement at low electron emission angles comes about from the inclusion of a classical mean-free-path in the electron transport step. Figure II-1 defines certain angular parameters used in the formulation of the model. The angle  $\theta$  is defined to be the angle between the electron propagation direction outside the sample and the sample surface. The angle  $\phi_x$  is the angle of x-ray incidence on the sample. The angle between the x-ray incidence and the electron propagation-directions is designated  $\alpha$  in this nomenclature. An additional angle  $\phi$  defines the azimuthal orientation of the sample and is important only in samples such as single crystals in which there are anisotropies parallel to the sample surface.

In most current experimental systems, the variation of the angular parameters is accomplished by simply rotating the sample on one, or perhaps two, distinct axes. The axis of rotation for concurrent variation of  $\theta$  and  $\phi_x$  is taken to lie in the sample surface and to be perpendicular to the plane containing the x-ray incidence direction, the electron escape direction and the surface normal,  $\vec{A}$ . In most experimental geometries, the angle  $\alpha$  is fixed by the overall analyzer design, so that rotation of the sample about the axis defined above varies  $\theta$  and  $\phi_x$  simultaneously and it can be seen that  $\phi_x = \pi - \alpha - \theta$ . A second axis for azimuthal rotations is taken to be the surface normal  $\vec{A}$ .

#### B. Flat Surface Intensity Model

In terms of a three-step model it is possible to write an expression for the number of photoelectrons which originate from a given energy level,  $k$ , within a differential volume element,  $dx dy dz$ , and are finally detected at an angle  $\theta$  as the product of the probabilities for each step. Following the nomenclature of Fadley et al.<sup>11</sup> such an expression has the form:

$$dN(k, \theta, \phi_x, x, y, z) = \left[ \begin{array}{l} \text{X-ray flux} \\ \text{at depth } z \end{array} \right] \cdot \left[ \begin{array}{l} \text{Number of atoms in} \\ \text{volume element} \end{array} \right] \quad (\text{II-1})$$

$$\cdot \left[ \begin{array}{l} \text{Probability for } k \\ \text{emission into } \Omega' \end{array} \right] \cdot \left[ \begin{array}{l} \text{Fraction reaching sur-} \\ \text{face in no-loss peak} \end{array} \right]$$

$$\cdot \left[ \begin{array}{l} \text{Electron flux change} \\ \text{in crossing surface} \end{array} \right] \cdot \left[ \begin{array}{l} \text{Instrumental} \\ \text{detection efficiency} \end{array} \right]$$

in which the first three factors on the right of equation II-1 govern the optical excitation step, the fourth and fifth factors are related to the transport and escape steps, respectively, and the final term is

included to relate the observed number of electrons to the number actually escaping from the sample. In order to put this expression into a more quantitative form, it is necessary to define certain experimental parameters and to relate the terms in equation II-1 to the physical properties of the specimen.

Figure II-2 presents a general experimental geometry for the development of equation II-1. In particular, the incident x-ray excitation flux is allowed to be non-uniform across the sample surface (a plane on which any point can be uniquely specified by the coordinates  $\theta$ ,  $x$ , and  $y$ ) and the intensity distribution is given by  $I(\theta, x, y)$ . If it is further assumed that the interaction of the x-rays with the sample can be described by classical electromagnetic theory, then the reflection and refraction of the x-rays at the surface can easily be calculated and the attenuation of the x-rays in the material can be accounted for by a simple x-ray mean-free-path,  $\Lambda_x$ . Henke<sup>9</sup> has carried out detailed calculations in which he demonstrates the validity of such an assumption. The x-ray flux at a depth  $z$  is then given by

$$\left[ \begin{array}{l} \text{X-ray flux} \\ \text{at depth} \end{array} \right] = \left[ I(\theta, x, y)(1 - R_x) \frac{\sin\phi_x}{\sin\phi_x'} \exp(-z/\Lambda_x \sin\phi_x') \right] \quad (\text{II-2})$$

in which  $R_x$  is the fraction of x-rays reflected at the surface,  $\sin\phi_x/\sin\phi_x'$  accounts for the refraction of x-rays from an angle  $\phi_x$  outside the sample to an angle  $\phi_x'$  inside the sample, and the exponential term accounts for the attenuation of the x-rays in traveling a distance  $z/\sin\phi_x'$  within the sample.

At this point, it is worth noting that x-ray reflection and refraction effects become significant only for x-ray incidence angles near a certain critical angle,  $\phi_c$ , for total x-ray reflection. For  $AlK_{\alpha}$  radiation with an energy of  $\sim 1500$  eV, the critical angle is on the order of  $1-3^\circ$  for most materials. Also,  $\Lambda_x$  for x-rays in this energy range is on the order of  $10^3\text{\AA} - 10^5\text{\AA}$  and is thus much greater than  $\Lambda_e$ . As a result of the relative magnitudes of these parameters it is possible in most experimental geometries for which  $30^\circ < \alpha < 75^\circ$  to disregard the effects of the variation of  $\phi_x$  while performing measurements in the range  $90^\circ < \theta < 0^\circ$ . The physical situation arising in this angle range is that all portions of the specimen from which no-loss electrons can originate are illuminated by the same x-ray flux  $I(\theta, x, y)$ . Conversely, the effects of the variation of  $\phi_x$  occur over a very small range of angles near  $\phi_c$  so that it is possible to neglect the effects of varying  $\theta$  when investigating the effects of varying  $\phi_x$ <sup>15</sup>.

The number of atoms in the differential volume element is given simply by

$$\left[ \begin{array}{l} \text{Number of atoms in} \\ \text{volume element} \end{array} \right] = \rho(z) dx dy dz \quad (\text{II-3})$$

in which  $\rho(z)$  is the z-dependent density of atoms associated with the k level in number/unit volume. The probability for k emission into the internal solid angle  $\Omega'$  is given by

$$\left[ \begin{array}{l} \text{Probability for k} \\ \text{emission into } \Omega' \end{array} \right] = \frac{\overline{d\sigma}_k}{d\Omega'} \Omega' (E, E_0, \theta, x, y) \quad (\text{II-4})$$

in which  $\frac{\overline{d\sigma}_k}{d\Omega'}$  is the average differential cross section for k emission into the internal solid angle  $\Omega'$ , E is the initial energy of the electron

and  $E_0$  is the energy at which the electron is detected. It has been pointed out<sup>14</sup> that this use of an average differential cross section is only valid for analyzer systems with a small, well-defined solid angle of electron acceptance.

The fraction of the electrons reaching the surface in the no-loss peak is given by a simple exponential attenuation law

$$\left[ \begin{array}{l} \text{Fraction reaching surface} \\ \text{in no-loss peak} \end{array} \right] = \exp(-z/\Lambda_e(E) \sin\theta') \quad (\text{II-5})$$

and the flux change in crossing the surface is

$$\left[ \begin{array}{l} \text{Electron flux change} \\ \text{in crossing surface} \end{array} \right] = (1 - R_e) \frac{\sin\theta'}{\sin\theta} \quad (\text{II-6})$$

In equation II-6  $R_e$ , which is the fraction of electrons reflected at the surface, depends on the energy of the exiting electron, its angle of incidence at the surface and the height and shape of the surface potential barrier. For electrons in the kinetic energy range 500 eV - 1500 eV, Fadley<sup>14</sup> has shown that for  $\theta \geq 10^\circ - 15^\circ$ , the effects of electron reflection and refraction become negligible. However, for very low angles of electron escape these effects can become significant.

If the detection efficiency is given as some energy-dependent function  $D_0(E, E_0)$  equation II-1 can be written as

$$\begin{aligned} dN(k, \theta, \phi_x, x, y, z) = & \left[ I(\theta, x, y) (1 - R_x) \frac{\sin\phi_x}{\sin\phi_x'} \exp(-z/\Lambda_x \sin\phi_x') \right]^{(\text{II-7})} \\ & \cdot \left[ \rho(z) dx dy dz \right] \cdot \left[ \frac{d\sigma_k}{d\Omega'} \Omega'(E, E_0, \theta, x, y) \right] \\ & \cdot \left[ \exp(-z/\Lambda_e(E) \sin\theta') \right] \cdot \left[ (1 - R_e) \frac{\sin\theta'}{\sin\theta} \right] \\ & \cdot D_0(E, E_0). \end{aligned}$$

Integration of equation II-7 over the proper limits with the substitution of appropriate functional forms for  $\rho(z)$ ,  $I(\theta, x, y)$ ,  $\Omega'$  ( $E, E_0, \theta, x, y$ ) and  $D_0(E, E_0)$  will give the desired measurable photoelectron intensity.

If  $\rho(z)$  is taken to be a constant (that is, if the atoms or molecules that give rise to the  $k$  level are taken to be homogeneously distributed in the sample), then equation II-7 can easily be integrated over the volume of a sample of thickness  $t$  to give the number of photoelectrons detected from such a sample. The result is

$$\begin{aligned}
 N_t(k, \theta, \phi_x) &= (1 - R_x) \left( \frac{\sin \phi_x'}{\sin \phi_x} \right) \rho(\overline{d\sigma}_k/d\Omega') (1 - R_e) \left( \frac{\sin \theta'}{\sin \theta} \right) \quad (\text{II-8}) \\
 &\cdot D_0(E, E_0) \left[ \int_A I(\theta, x, y) \Omega'(E, E_0, \theta, x, y) dx dy \right] \\
 &\cdot \left[ \frac{1}{\Lambda_x \sin \phi_x'} + \frac{1}{\Lambda_e(E) \sin \theta'} \right]^{-1} \\
 &\cdot \left[ 1 - \exp \left\{ -t \left( 1/\Lambda_x \sin \phi_x' + 1/\Lambda_e(E) \sin \theta' \right) \right\} \right]
 \end{aligned}$$

Equation II-8 can be greatly simplified by the introduction of several reasonable assumptions. If electron reflection and refraction are neglected, which is reasonable for XPS energies and  $\theta' \geq 10^\circ$ , then  $\theta = \theta'$ ,  $R_e = 0$  and  $\Omega = \Omega'$ . If the further assumption is made that  $\phi_x \gg \phi_c$ , then  $\phi_x' = \phi_x$ ,  $R_x = 0$ , and  $\Lambda_x \sin \phi_x' > \Lambda_e \sin \theta'$ . In this case, equation II-8 becomes

$$\begin{aligned}
 N_t(k, \theta) &= \rho(\overline{d\sigma}_k/d\Omega) \cdot D_0(E, E_0) \left[ \int_A I(\theta, x, y) \Omega(E, E_0, \theta, x, y) dx dy \right] \quad (\text{II-9}) \\
 &\cdot \Lambda_e(E) \sin \theta \cdot \left[ 1 - \exp(-t/\Lambda_e(E) \sin \theta) \right]
 \end{aligned}$$

In equation II-9 only  $D_o(E, E_o)$  and the integral over  $x$  and  $y$  are dependent on the spectrometer. Therefore, it is possible to define a spectrometer system response function  $R_k(E, E_o, \theta)$  for a peak  $k$  by

$$R_k(E, E_o, \theta) = D(E, E_o) \sin\theta \int_A I(\theta, x, y) \Omega(E, E_o, \theta, x, y) dx dy \quad (II-10)$$

The factor of  $\sin\theta$  is included to give the convenient result that  $R_k(E, E_o, \theta)$  is constant for a certain ideal geometry. In particular, if the x-ray flux is assumed to have a constant value  $I_o$  across the sample and if the acceptance solid angle is characterized by  $\Omega_o(E, E_o)$  within an entrance aperture of area  $A_o$  (the conditions shown by the dotted curves in figure II-2) then the response function is given by

$$R_k(E, E_o, \theta) = D(E, E_o) I_o \Omega_o(E, E_o) A_o \quad (II-11)$$

so long as the specimen fills the entrance aperture  $A_o$ . Under these conditions the effective surface area of the sample is given by  $A_o/\sin\theta$  and equation II-11 applies. However, if  $\theta$  is less than some angle  $\theta_{\min}$  at which the illuminated area of the sample just ceases to fill the entrance aperture, then the effective surface area is given by  $A_o/\sin\theta_{\min}$  and the equation for the response function becomes

$$R_k(E, E_o, \theta) = D(E, E_o) I_o \Omega_o(E, E_o) \cdot A_o \cdot \frac{\sin\theta}{\sin\theta_{\min}} \quad (II-12)$$

If equation II-10 is substituted into II-9, the expression for  $N_t(k, \theta)$  becomes

$$N_t(k, \theta) = \frac{R_k(E, E_o, \theta)}{\sin\theta} \rho(\bar{d}\sigma_k/d\Omega) \Lambda_e(E) \sin\theta \quad (II-13)$$

$$\cdot \left[ 1 - \exp(-t/\Lambda_e(E) \sin\theta) \right]$$

and for  $\theta > \theta_{\min}$  the  $\sin\theta$  factors cancel. For an infinitely thick sample equation II-13 thus reduces to

$$N_{\infty}(k, \theta) = R_k(E, E_0, \theta) \rho (\overline{d\sigma}_k/d\Omega) \Lambda_e(E). \quad (\text{II-14})$$

Two important results can be deduced from equation II-14. First, for an ideal spectrometer geometry as defined above, it can be seen that  $N_{\infty}(k, \theta)$  is independent of  $\theta$  for  $\theta > \theta_{\min}$ , a result that has been verified experimentally by Henke<sup>9</sup> and by Fraser et al.<sup>10</sup>. Second,  $R_k(E, E_0, \theta)$  can be determined from angular distribution measurements on a clean thick sample provided that  $\overline{d\sigma}/d\Omega$ ,  $\rho$ , and  $\Lambda_e(E)$  are known. Furthermore, if it possible to separate the solid angle function into an energy-dependent part and an energy-independent part and if the energy-dependent part merely scales the acceptance solid angle with energy, then the expression for  $\Omega$  can be written as

$$\Omega(E, E_0, \theta, x, y) = F\left(\frac{E_0}{E}\right) \Omega(\theta, x, y). \quad (\text{II-15})$$

$R_k$  then becomes

$$R_k(E, E_0, \theta) = D(E, E_0) F(E_0/E) \sin\theta \int_A I(\theta, x, y) \Omega(\theta, x, y) dx dy \quad (\text{II-16})$$

which allows a response function dependent on  $\theta$  only to be defined as

$$R(\theta) \equiv \sin\theta \int_A I(\theta, x, y) \Omega(\theta, x, y) dx dy \quad (\text{II-17})$$

It is this form of the response function that will be used in section IV in discussing the operation of a dispersion compensating electron spectrometer in angle-resolved measurements.

### C. Effects of Overlayers

Equations II-13 and II-14 can easily be applied to the situation of a thin overlayer of thickness  $t'$  on an infinitely thick substrate. If the overlayer quantities are noted by primes and emission is taken to be from a level  $\ell$  in the overlayer and a level  $k$  in the substrate, then the angular dependence of the number of photoelectrons from the overlayer will be given by equation II-13 directly as

$$N_{t'}(\ell, \theta) = R_{\ell}(E^{\ell}, E_o^{\ell}, \theta) \rho' (\overline{d\sigma}_{\ell}'/d\Omega) \Lambda_e'(E^{\ell}) \cdot \left[ 1 - \exp(-t'/\Lambda_e'(E^{\ell}) \sin\theta) \right] \quad (\text{II-18})$$

and the number of photoelectrons detected from the substrate will be given by equation II-14 with the addition of a term to account for attenuation in the overlayer

$$N_{\infty, t'}(k, \theta) = R_k(E_o^k, E^k, \theta) \rho (\overline{d\sigma}_k/d\Omega) \Lambda_e(E^k) \cdot \exp(-t'/\Lambda_e'(E^k) \sin\theta) \quad (\text{II-19})$$

The ratio of the overlayer to substrate intensity is then given by

$$R_{\ell/k}(\theta) \equiv \frac{N_{t'}(\ell, \theta)}{N_{\infty, t'}(k, \theta)} = \frac{R_{\ell}(E^{\ell}, E_o^{\ell}, \theta) \rho' (\overline{d\sigma}_{\ell}'/d\Omega) \Lambda_e'(E^{\ell})}{R_k(E^k, E_o^k, \theta) \rho (\overline{d\sigma}_k/d\Omega) \Lambda_e(E^k)} \cdot \left[ 1 - \exp(-t'/\Lambda_e'(E^{\ell}) \sin\theta) \right] \exp(t'/\Lambda_e'(E^k) \sin\theta) \quad (\text{II-20})$$

Subject to the assumptions of equation II-15, equation II-20 can be written

$$R_{l/k}(\theta) = \frac{D(E^l, E_o^l) F(E_o^l/E^l) \rho' (\overline{d\sigma}_l'/d\Omega) \Lambda_e'(E^l)}{D(E^k, E_o^k) F(E_o^k/E^k) \rho (\overline{d\sigma}_k/d\Omega) \Lambda_e(E^k)} \quad (\text{II-21})$$

$$\cdot \left[ 1 - \exp(-t'/\Lambda_e'(E^l) \sin\theta) \right] \cdot \exp(t'/\Lambda_e'(E^k) \sin\theta).$$

in which the angle-dependent response function  $R(\theta)$  cancels in the ratio. This result demonstrates that meaningful angular distribution studies can be performed without a detailed knowledge of  $R(\theta)$  so long as the assumptions implicit in equation II-15 are valid and only relative intensity measurements are made at a given angle.

If the angle-independent terms of equation II-21 are gathered together in a constant  $K$ , such that

$$K = \frac{D(E^l, E_o^l) F(E_o^l/E^l) \rho' (\overline{d\sigma}_l'/d\Omega) \Lambda_e'(E^l)}{D(E^k, E_o^k) F(E_o^k/E^k) \rho (\overline{d\sigma}_k/d\Omega) \Lambda_e(E^k)}, \quad (\text{II-22})$$

then

$$R_{l/k}(\theta) = K \left[ 1 - \exp(-t'/\Lambda_e'(E^l) \sin\theta) \right] \cdot \exp(t'/\Lambda_e(E^k) \sin\theta). \quad (\text{II-23})$$

Furthermore, if the kinetic energies of the two peaks are nearly equal then  $\Lambda_e'(E^l) \approx \Lambda_e(E^k)$  and

$$K \approx \frac{\rho' \cdot (\overline{d\sigma}_l'/d\Omega) \cdot \Lambda_e'(E^l)}{\rho \cdot (\overline{d\sigma}_k/d\Omega) \cdot \Lambda_e(E^k)} \quad (\text{II-24})$$

while

$$R_{l/k}(\theta) = K \left[ \exp(t'/\Lambda_e'(E) \sin\theta) - 1 \right]. \quad (\text{II-25})$$

Equation II-25 can be rewritten as

$$\ln \left[ R_{\ell/k}(\theta)/K + 1 \right] = \frac{t'}{\Lambda_e'(E)} \cdot \frac{1}{\sin\theta} \quad (\text{II-26})$$

so that a plot of the left-hand side of equation II-26 vs.  $1/\sin\theta$  should give a straight line of slope  $t'/\Lambda_e'(E)$ . It was in terms of such an analysis that Hill et al.<sup>16</sup> examined the validity of this model for angle-resolved photoemission from thick silicon substrates with thin oxide overlayers.

#### D. Effects of Surface Roughness

Implicit in the foregoing discussion was the assumption that the sample surface was atomically flat so that the angles  $\phi_x$  and  $\theta$  could everywhere be measured relative to the planar sample surface. A more realistic description of the sample surface must allow for the presence of surface roughness. Figure II-3 presents a generalized rough surface and illustrates some additional effects that are introduced by surface roughness. These effects arise basically from two mechanisms: shading of some points on the sample surface from either x-ray incidence or electron escape by adjacent surface features, and variation of the true local angles  $\phi_x^t$  and  $\theta^t$  from the experimental angles  $\phi_x$  and  $\theta$ .

The presence of shading effects will reduce the effectiveness of some areas of the sample in producing photoelectrons. Several particularly simple limiting cases of shading effects which are physically realistic can be envisioned. If the dimensions of the surface contours are large relative to the electron mean-free-path (which will often be the case since  $10 \text{ \AA} < \Lambda_e < 40 \text{ \AA}$ ), then the shading of electrons can be

assumed to be perfect or complete for the region obscured by an adjacent surface feature. Similarly, if the dimensions of the surface contours are either very large or very small relative to  $\Lambda_x$ , then x-ray shading can be assumed to be either complete or absent, respectively. For many samples x-ray shading can be neglected since  $10^3 \text{ \AA} \leq \Lambda_x \leq 10^5 \text{ \AA}$ , so that  $\Lambda_x$  is large relative to the contours on, for instance, a highly polished sample.

In addition to shading effects, the variation of  $\phi_x^t$  and  $\theta^t$  from the experimental  $\phi_x$  and  $\theta$  must be accounted for. This can be done in the limit of perfect shading by treating each differential element of the rough surface area  $dA^R$  as a separate sample characterized by angles  $\phi_x^t$  and  $\theta^t$  and then by integrating over only those areas that are unshaded for both x-rays and electrons. The superscript R will be used to distinguish rough-surface values. If this is done, an expression equivalent to II-8 can be derived

$$N_t^R(k, \theta, \phi_x) = \rho (\overline{d\sigma_k/d\Omega}) D(E, E_0) \quad (\text{II-27})$$

$$\cdot \left[ \int_{A^R(\theta)} (1 - R_x) \left( \frac{\sin \phi_x^t}{\sin \phi_x^{t'}} \right) (1 - R_e) \left( \frac{\sin \theta^{t'}}{\sin \theta^t} \right) I(\theta, x, y) \Omega'(E, E_0, \theta, x, y) \right. \\ \cdot \left. \left[ \frac{1}{\Lambda_x \sin \phi_x^{t'}} + \frac{1}{\Lambda_e(E) \sin \theta^{t'}} \right]^{-1} \right. \\ \cdot \left. \left[ 1 - \exp \left\{ -t' (1/\Lambda_x \sin \phi_x^{t'} + 1/\Lambda_e(E) \sin \theta^{t'}) \right\} \right] dA^R(x, y) \right]$$

in which the integration over  $dx dy$  is replaced by a rough surface area element  $dA^R(x,y)$  and a new  $z'$  coordinate is defined perpendicular to  $dA^R$ . The integration over  $A^R(\theta)$  includes all unshaded surface elements at the angle  $\theta$  and the intensity is from a layer of thickness  $t'$  parallel to the rough surface. If the average value of a given quantity  $Q$  over the unshaded area of the rough surface is defined as

$$\langle Q \rangle = \left[ \int_{A^R(\theta)} Q dA^R \right] / A^R(\theta) \quad (\text{II-28})$$

and if  $I(\theta,x,y)$  and  $\Omega'(E,E_0,\theta,x,y)$  vary slowly over the characteristic dimensions of the surface roughness, then an equation equivalent to II-9 can be written provided that the assumptions of negligible x-ray and electron refraction and reflection are met

$$N_{t'}^R(k, \theta) = \rho (\overline{d\sigma_k} / d\Omega) D(E, E_0) \left[ \int_A I(\theta,x,y) \Omega(E,E_0,\theta,x,y) dx dy \right] \quad (\text{II-29})$$

$$\cdot (A^R(\theta)/A) \Lambda_e(E) \cdot \left\langle \left[ 1 - \exp(-t' / \Lambda_e(E) \sin\theta^t) \right] \cdot \sin\theta^t \right\rangle$$

In this equation,  $A$  is the area of a planar surface of the same outside dimensions as the rough surface. The term  $A^R(\theta)/A$  accounts for phenomena associated with rough-surface area changes relative to a flat surface and effects due to deviations from the average exit angle are contained in the term enclosed in brackets  $\langle \dots \rangle$ . The instrument-dependent parameters in II-29 are the same as those in the flat surface model, so combining II-10 with II-29 gives

$$N_{t'}^R(k, \theta) = \frac{R_k(E, E_o, \theta)}{\sin\theta} \rho (\overline{d\sigma}_k/d\Omega) \Lambda_e(E) (A^R(\theta)/A) \quad (\text{II-30})$$

$$\cdot \left\langle \left[ 1 - \exp(-t'/\Lambda_e(E) \sin\theta^t) \right] \sin\theta^t \right\rangle$$

and for an infinitely thick rough sample with a clean surface

$$N_{\infty}^R(k, \theta) = \frac{R_k(E, E_o, \theta)}{\sin\theta} \rho (\overline{d\sigma}_k/d\Omega) \Lambda_e(E) (A^R(\theta)/A) \langle \sin\theta^t \rangle \quad (\text{II-31})$$

An equation entirely analogous to equation II-20 can be written for the overlayer/substrate ratio for a rough sample in which the overlayer follows the contours of the roughness and is of a uniform thickness  $t'$  perpendicular to  $dA^R$ :

$$R_{l/k}^R(\theta) \equiv \frac{N_{t'}^R(l, \theta)}{N_{\infty, t'}^R(k, \theta)} = \frac{R_l(E^l, E_o^l, \theta) \rho' (\overline{d\sigma}_l/d\Omega) \Lambda_e'(E^l)}{R_k(E^k, E_o^k, \theta) \rho (\overline{d\sigma}_k/d\Omega) \Lambda_e(E^k)} \quad (\text{II-32})$$

$$\frac{\left\langle \left[ 1 - \exp(-t'/\Lambda_e'(E^l) \sin\theta^t) \right] \cdot \sin\theta^t \right\rangle}{\left\langle \exp(-t'/\Lambda_e'(E^k) \sin\theta^t) \cdot \sin\theta^t \right\rangle}$$

It is in terms of equation II-32 that the predictions of this rough surface model are tested in section V.

A further point worth noting with regard to equation II-31 is that in the limit of no x-ray shading and perfect electron shading, the projection of the unshaded rough surface in the direction of electron detection,  $\int_{A^R(\theta)} \sin\theta \, dA^R$ , must equal the projection of the planar area in the same direction,  $(\sin\theta)A$ . Along with the definition of  $\sin\theta^t$  (equation II-28), this equality implies that

$$\frac{\langle \sin\theta^t \rangle}{\sin\theta} \cdot \frac{A^R(\theta)}{A} = 1 \quad (\text{II-33})$$

so that in equation II-31  $N_{\infty}^R(k, \theta) \propto R(E, E_0, \theta)$  and the response function can be determined from a rough sample. This result is useful in the experimental determination of the system response function in section IV.

#### E. Angular Dependence of Plasmon Loss Spectra

The first evidence for plasmon excitation by energetic electrons moving in free-electron-like metals was provided by electron transmission and electron reflection experiments<sup>17,18,19</sup>. Subsequently, many investigations have been made of the characteristic energy loss features in energy distributions of electrons transmitted or reflected by a variety of materials<sup>20</sup>. In 1953 Bohm and Pines correctly attributed these energy loss features to collective oscillations of the valence electrons in the metal<sup>21</sup>. In these collective oscillations, the nearly free valence electrons behave like a plasma and move in a correlated fashion relative to the fixed positive charge distribution of the metal-ion cores. Powell<sup>22</sup> carried out electron reflection experiments on solid and liquid metal surfaces and found that the loss features associated with the excitation of two-dimensional surface-plasmons were greatly enhanced for electrons which were reflected at near grazing angles.

Plasmon loss peaks have also been observed in XPS<sup>23,24</sup>, UPS<sup>25</sup>, and Auger electron spectra<sup>26</sup> as extra structure on the low-kinetic-energy side of the no-loss peaks. This extra structure contains contributions from both three-dimensional bulk-plasmon excitations and two-dimensional surface plasmons. Angular dependent XPS provides a promising method for separating the surface and bulk contributions since, as shown in previous sections, varying the angle of electron emission with respect to the

surface changes the effective sampling depth.

In the case of the free-electron-like metals such as Na, K, Mg, and Al, the valence electrons are bound very weakly to the ion-cores. Thus, a classical calculation assuming that each valence electron moves under the influence of a macroscopic electric field caused by the collective motion of this electron 'gas' relative to the ion-cores provides a very good description of the plasma oscillations. For such a free-electron gas the classical plasma frequency is given by<sup>27</sup>

$$\omega_p = \sqrt{\frac{4 \pi n e^2}{m}} \quad (\text{II-34})$$

in which  $\omega_p$  is angular frequency of the bulk plasmon,  $e$  is the electron charge,  $m$  is the mass of the electron and  $n$  is the valence-electron concentration. As a result of the imposition of additional boundary conditions at the metal-vacuum interface, the frequency of the two-dimensional surface plasmon,  $\omega_s$ , is given by

$$\omega_s = \omega_p / \sqrt{2} \quad (\text{II-35})$$

Both of these oscillations are capable of wavelike propagation and are longitudinal in character; that is, they consist of charge density waves with planar contours of equal density perpendicular to the direction of propagation. For aluminum with a density of  $2.70 \text{ g-cm}^{-3}$  and three valence electrons per atom, the classical plasma frequencies are  $\omega_p = 2.40 \times 10^{16} \text{ rad sec}^{-1}$  and  $\omega_s = 1.70 \times 10^{16} \text{ rad sec}^{-1}$  so that the plasmon energies are  $\omega_p = 15.8 \text{ eV}$  and  $\omega_s = 11.2 \text{ eV}$ . These classical values are in fairly good agreement with Powell and Swan's

transmission measurement<sup>20</sup> ( $\omega_p = 15.3$  eV,  $\omega_s = 10.3$  eV) and Pollak's XPS results<sup>24</sup> ( $\omega_p = 15.7$  eV,  $\omega_s = 10.4$  eV).

It is also possible to calculate the mean-free-path for excitation of a bulk plasmon by a moving electron of kinetic-energy  $E$  from the classical theory. The mean-free-path is given by<sup>28</sup>

$$\lambda_{pl}(E) = \frac{2a_0 E}{\hbar \omega_p} \left( \ln \frac{k_c v}{\omega_p} \right)^{-1} \quad (\text{II-36})$$

where  $a_0$  is the Bohr radius,  $v$  is the electron velocity,  $E$  is the electron energy and  $k_c$  is a cutoff wave vector characterizing the shortest-wavelength plasmons that can be excited in the electron gas. For 1400 eV electrons in aluminum  $\lambda_{pl} = 37.7 \text{ \AA}$ .

However, this value of the mean-free path is not quantitatively meaningful in interpreting XPS results because it neglects both the presence of the surface and the core hole left behind in the photoionization event. Feibelman<sup>28</sup> has pointed out that the surface and bulk plasma modes are orthogonal, so that the probability for exciting bulk plasmons decreases near the surface, while the probability for surface plasmon excitation is maximized at the surface and decays with increasing depth into the solid. This depth dependence of the probability of exciting bulk and surface plasmons must be accounted for in any theoretical description of the plasmon loss spectra in XPS experiments. Also, the core hole presents another problem not accounted for by the classical theory. The formation of the core hole can itself couple to the plasma field and result in the emission of so-called 'intrinsic' plasmons distinct from the 'extrinsic' plasmons emitted by the moving

electron<sup>29</sup>. It is also possible for the intrinsic and extrinsic effects to interfere with each other, resulting in virtual plasmons emitted by one mechanism being absorbed by the other mechanism.

As a result of these complications, the simple three-step model for photoemission breaks down when applied to the description of the plasmon loss spectrum in XPS. A proper theoretical description must account for the position dependence of the probability of plasmon emission as it affects the transport step and for the coupling of the core hole to the plasmon field which makes the optical excitation step a many-electron process. Chang and Langreth<sup>30</sup>; Šunjić, Šokčević, and Lucas<sup>31</sup>; and Feibelman<sup>28,32</sup> have all formulated models based on many-body theory which correctly describe plasmon excitations in the XPS experiment. Chang and Langreth's theory is a full many-body treatment of the inelastic loss problem, but its computational complexity makes it difficult to generate results which can be compared directly to experiment. Šunjić's and Feibelman's theories are somewhat simpler and allow for the calculation of theoretical results directly comparable to experiment. These theories use a jellium (free-electron) model for the metal and introduce the metal-vacuum interface as a step discontinuity in the electron density. Both theories provide for the calculation of the probability of plasmon emission as a function of the depth of the photoemitter below the surface, the angle of electron emission, and the number of plasmons of each type emitted. This probability  $P_{p\ell}(E_0; E_{mn}, \ell, \theta, \omega_p, \omega_s, \gamma)$  is given by

$$P_{p\ell}(E_0; E_{mn}, \ell, \theta, \omega_p, \omega_s, \gamma) = P_0 \frac{Q_S}{n!} \frac{Q_B}{m!} \quad (\text{II-37})$$

where:  $E_0$  is the initial energy of the photoelectron,  $E_{mn} = m\hbar\omega_p + n\hbar\omega_s$  is the energy loss associated with exciting  $m$  bulk and  $n$  surface plasmons,  $\ell$  is the depth of the photoemitter,  $\theta$  is the angle of emission relative to the surface,  $\omega_p$  and  $\omega_s$  are the bulk and surface plasmon frequencies, respectively, and  $\gamma$  is the inverse lifetime of the core hole. The factors  $Q_B$  and  $Q_S$  are the probability of exciting one bulk or surface plasmon, respectively, and

$$P_0 = e^{-(Q_S + Q_B)} \quad (\text{II-38})$$

so that the right side of equation II-37 is just the Poisson distribution for the probability of exciting  $n$  surface and  $m$  bulk plasmons. The probabilities for single plasmon excitation result from the full many-body theory and are given in Šunjić's model by<sup>31</sup>

$$Q_S = \frac{e^2 \omega_s}{\hbar} \int_0^{\frac{\pi}{\phi}} \frac{d\phi}{\pi} \int_0^{k_c} dk \left\{ \frac{k^2 v_{\perp}^2}{D_s^2} + e^{-2\ell k} \frac{(a_s - \omega_s)^2 + (kv + \gamma)^2}{4D_s b_s} \right. \\ \left. - e^{-k\ell} \frac{kv}{D_s^2 b_s} \left[ \cos \frac{a_s \ell}{v_{\perp}} (kv_{\perp} b_s + \gamma D_s) + \sin \frac{a_s \ell}{v_{\perp}} (\omega_s D_s - a_s b_s) \right] \right\} \quad (\text{II-39})$$

$$Q_B = \frac{e^2 \omega_p}{\hbar} \int_0^{\frac{\pi}{\phi}} \frac{d\phi}{\pi} \int_0^{k_c} dk \left\{ \frac{k}{D_p} \ell + \frac{(a_p - \omega_p)^2 + (\gamma - kv)^2}{2b_p D_p} \right\} - 2Q_S \text{ (with } \omega_s \rightarrow \omega_p) \quad (\text{II-40})$$

in which:

$$a_{s,p} = \omega_{s,p} + kv_{\parallel} \cdot \cos \theta;$$

$$D_{s,p} = a_{s,p}^2 + k^2 v_{\perp}^2 \quad ;$$

$$b_{s,p} = \omega_{s,p}^2 + \gamma^2 \quad .$$

The velocity of the electron is denoted by  $v$ , and  $v_{\perp}$  and  $v_{\parallel}$  are the velocity components perpendicular and parallel to the surface, respectively. The integration over plasmon wave vector  $k$  is carried out only up to some wave-vector  $k_c$  termed the plasmon wave-vector cutoff. This cutoff is introduced into the theory to avoid an unphysical divergence of the integral that arises from including long wave vector plasmons which do not actually propagate in the metal<sup>23,30,31</sup>.

In generating theoretical curves for this thesis, it was not necessary to evaluate the  $Q$ 's since they had been provided to us by both Feibelman<sup>32</sup> and Šunjić<sup>33</sup>. Therefore, equation II-37 could be used directly to calculate the probability of multiple plasmon emission as a function of depth and angle. When these probabilities were corrected for short-range inelastic effects as described in section VI and integrated over emitter depth, it was possible to evaluate the relative intensities of the various plasmon loss peaks as a function of angle.

### 3. Microscopic Effects

#### A. General Considerations

In addition to macroscopic effects which average over crystalline order, XPS angular distributions from single crystal specimens show pronounced structure which is directly related to the periodicity of the

crystal lattice. These single crystal effects, which can be classified as microscopic in nature, can also be discussed in terms very close to the three-step model of photoemission.

The two pronounced microscopic effects which have been observed are the variation of total (or energy-integrated) peak intensities with angle<sup>16,34-36</sup> and the angular dependence of the shapes of the valence band spectra of metal crystals<sup>37-39</sup>. The variations in the valence band spectra can be thought of as arising in the optical excitation step of the photoemission process. In this step direct transition effects<sup>37,39</sup> and/or matrix element variations<sup>38</sup> can modify the observed shapes of the valence bands. The modulation of the integrated peak intensity with angle then occurs during the transport step in which the exiting electrons interact with and are scattered by the crystal lattice. Separating the microscopic effects in this way greatly simplifies the discussion of the observed results, even though a more complex one-step picture is no doubt more rigorously correct.

#### B. Total Peak Intensity Variations

The total peak intensity variations in XPS angular distributions can be described qualitatively in terms of the Kikuchi band phenomena observed in high-energy electron transmission experiments<sup>40</sup> and in LEED experiments<sup>41-43</sup>. Such effects require a diffuse source of nearly monoenergetic electrons within the crystal. In electron transmission and LEED experiments, these diffuse electrons are provided by inelastic scattering out of the primary and secondary beams. In XPS, the photoelectrons are the diffuse source. The Kikuchi bands appear as bands

of excess intensity bordered by deficiency bands in the diffuse emission from the crystal. The excess bands are centered on projections of the crystal planes and have a width of  $\sim 2 \theta_{hkl}(E)$ , where  $\theta_{hkl}(E)$  is the Bragg angle for diffraction of electrons of kinetic energy  $E$  from the crystal planes with Miller indices  $h, k, l$ . The deficiency bands arise from the diffraction of electrons out of trajectories which cross a set of planes at approximately the Bragg angle. These deficiency bands are then located  $\sim \theta_{hkl}(E)$  on either side of the projection of the  $hkl$  planes. The intensity diffracted out of the deficiency bands in turn appears in the excess band. It is in terms of this type of qualitative description that the results of section VII are discussed.

### C. Angular Dependence of Valence Band Spectra

The angular dependence of the valence band spectra of metal crystals can be described by a model which includes both direct-transition effects and also matrix-element effects in the bulk optical excitation step of the photoemission process. Different investigators have focused on different aspects of this model, with some emphasizing the matrix-element effects<sup>38</sup>, and other emphasizing the direct-transition aspect<sup>37,39</sup> of the excitation step. In this thesis such angular-dependent valence-band spectra for gold are interpreted using a direct-transition model similar to that used previously in interpreting angular-dependent UPS spectra<sup>44</sup>.

The direct-transition model requires, in addition to energy conservation, the simultaneous conservation of wave-vector. The initial and final electron states,  $\phi^i(\vec{r})$  and  $\phi^f(\vec{r})$ , can be written as Bloch

functions in the crystal so that  $\phi^i(\vec{r}) = e^{i\vec{k}^i \cdot \vec{r}} u_{\vec{k}^i}(\vec{r})$  and  $\phi^f(\vec{r}) = e^{i\vec{k}^f \cdot \vec{r}} u_{\vec{k}^f}(\vec{r})$ . The two conservation equations can then be written as:

$$E^f = E^i + h\nu \quad (\text{II-41})$$

and

$$\vec{k}^f = \vec{k}^i + \vec{k}_{h\nu} + \vec{g} \quad (\text{II-42})$$

where  $E^f$  and  $E^i$  are the final and initial electron energies,  $\vec{k}^f$  and  $\vec{k}^i$  are the final and initial electron wave vectors,  $h\nu$  is the photon energy,  $\vec{k}_{h\nu}$  is the photon momentum, and  $\vec{g}$  is a reciprocal lattice vector. The photoelectron energy distribution  $N(E, h\nu)$  is then given by<sup>38,45</sup>

$$N(E, h\nu) \propto \sum_i \int_{\vec{k}^f} d^3k^f |\langle \phi^f(\vec{r}) | \vec{A} \cdot \vec{\nabla} | \phi^i(\vec{r}) \rangle|^2 \cdot \delta(\vec{k} - \vec{k} - \vec{k} - \vec{g}) \quad (\text{II-43})$$

obs.

$$\cdot \delta(E^f - E^i - h\nu) \cdot \delta(E - E^i)$$

in which  $\vec{A} \cdot \vec{\nabla}$  represents the perturbation due to electromagnetic radiation and the other terms are as defined above. The summation is over occupied states in the crystal and the integration is over only those final state wave vectors which are within the solid-angle cone of acceptance of the analyzer. The delta functions represent wave vector and energy conservation and the factor  $|\langle \phi^f(\vec{r}) | \vec{A} \cdot \vec{\nabla} | \phi^i(\vec{r}) \rangle|^2$  contains any matrix element effects.

If the matrix elements are assumed to be equal for all transitions, then the simplest direct transition model is recovered, and  $N(E, h\nu)$  is proportional to the density of initial states from which allowed transitions can occur. The conical acceptance of the analyzer can be shown in the XPS limit to restrict the observed  $\vec{k}^f$  values to a planar

disk in an extended zone scheme in  $\vec{k}$ -space. The photon momentum  $\vec{k}_{h\nu}$  is furthermore known so that for each point on the disk, a unique  $\vec{g}$  vector can be determined which will project that point into the reduced zone to a unique value of  $\vec{k}^i$ . A knowledge of the band structure  $E^i(\vec{k}^i)$  then permits determining the density of initial states for comparison to spectra. In this way the wave vector conservation limits the initial states which can contribute to the observed spectrum at a given angle.

The effect of matrix element variations would be to modulate the relative intensities of the various contributions to the final spectrum. However, good initial and final state wave functions are needed to accurately evaluate the matrix elements, although a certain degree of agreement has been obtained between XPS experiments and theory by using a simple plane wave final state, and neglecting any restrictions imposed by wave vector conservation<sup>38</sup>. A clear resolution of the degrees of accuracy of these two limiting uses of the same basic model awaits further experimental and theoretical verification.

REFERENCES  
SECTION II

- 1) C. N. Berglund and W. E. Spicer, Phys. Rev. 136, A1030 (1964).
- 2) C. Caroli, D. Lederer-Rozenblatt, B. Roulet, and D. Saint-James, Phys. Rev. B8, 4552 (1973).
- 3) I. Adawi, Phys. Rev. 134, A788 (1964)
- 4) G. D. Mahan, Phys. Rev. B2, 4334 (1970).
- 5) W. L. Schaich and N. W. Ashcroft, Phys. Rev. B3, 2452 (1970).
- 6) See, for instance, Chapter 20 of E. Merzbacher, Quantum Mechanics, John Wiley and Sons, Inc., New York (1961) for a discussion of Fermi's Golden-Rule of time-dependent perturbation theory and its application to the calculation of transition rates.
- 7) P. J. Feibelman and D. E. Eastman, Phys. Rev. B10, 4932 (1974).
- 8) C. J. Powell, Surf. Sci. 44, 29 (1974).
- 9) B. L. Henke, Phys. Rev. A6, 94 (1972).
- 10) W. A. Fraser, J. V. Florio, W. N. Delgass, and W. D. Robertson, Surf. Sci. 36, 661 (1973).
- 11) C. S. Fadley, R. J. Baird, W. Wiekhaus, T. Novakov, and S. Å. L. Bergstrom, J. Electron Spectrosc. 4, 93 (1974).
- 12) C. S. Fadley, J. Electron Spectrosc. 5, 725 (1974).
- 13) C. S. Fadley, Faraday Discussion No. 60, 18 (1975).
- 14) C. S. Fadley, Progress in Solid State Chemistry, G. Somorjai and J. McCaldin, Eds., Pergamon Press,
- 15) M. Mehta and C. S. Fadley, Physics Letters 55A, 59 (1975).

- 16) J. M. Hill, M.S. Thesis, Department of Chemistry, University of Hawaii, 1975; and J. M. Hill, D. R. Royce, C. S. Fadley, and F. J. Grunthaner, Chem. Phys. Letters 44, 225 (1976).
- 17) E. Rudberg, Proc. Roy. Soc. (London) A127, 111 (1930).
- 18) E. Rduberg, Phys. Rev. 50, 138 (1936).
- 19) G. Ruthemann, Ann. Phys. 6, 113 (1948).
- 20) C. J. Powell and J. B. Swan, Phys. Rev. 115, 869 (1959), and references therein.
- 21) D. Bohm and D. Pines, Phys. Rev. 92, 609 (1953).
- 22) C. J. Powell, Phys. Rev. 175, 972 (1968).
- 23) See for example: Y. Baer and G. Busch, Phys. Rev. Lett. 30, 280 (1973); S. A. Flodstrom, R. Z. Bachrach, R. S. Bauer, J. C. McMenamain and S. B. M. Hagstrom, to appear in J. Vac. Sci. Tech., Proc. of Chicago Meeting, 1976.
- 24) R. A. Pollak, L. Ley, F. R. McFeely, S. P. Kowalczyk, and D. A. Shirley, J. Electron Spectrosc. 3, 381 (1974).
- 25) See for example: N. V. Smith and W. E. Spicer, Phys. Rev. Lett. 23, 769 (1969); and I. Lindau, H. Löfgren, and L. Walldén, Phys. Lett. 36A, 293 (1971).
- 26) See for example: L. H. Jenkins and M. F. Chung, Surf. Sci. 28, 409 (1971); and A. Barrie and F. J. Street, J. Electron Spectrosc. 7, 1 (1975).
- 27) C. Kittel, Introduction to Solid State Physics, 4th Ed., 269-277, John Wiley & Sons, Inc., New York (1971).
- 28) P. J. Feibelman, Phys. Rev. B7, 2305 (1973).

- 29) D. C. Langreth, Phys. Rev. Lett. 26, 1229 (1971).
- 30) J. J. Chang and D. C. Langreth, Phys. Rev. B5, 3512 (1972);  
Phys. Rev. B8, 4638 (1973).
- 31) M. Šunjić, D. Šokčević, and A. Lucas, J. Electron Spectrosc.  
5, 963 (1974).
- 32) P. J. Feibelman, private communication.
- 33) M. J. Šunjić, private communication.
- 34) K. Siegbahn, U. Gelius, H. Siegbahn and E. Olsen, Phys. Letters  
32A, 221 (1970).
- 35) C. S. Fadley and S. Å. L. Bergstrom, Phys. Letters 35A, 375 (1971).
- 36) C. S. Fadley and S. Å. L. Bergstrom, in Electron Spectroscopy,  
D. A. Shirley, Ed., North Holland, Amsterdam, 1972, p. 233.
- 37) R. J. Baird, L. F. Wagner, and C. S. Fadley, Phys. Rev. Lett.  
37, 111 (1976).
- 38) F. R. McFeely, J. Stohr, G. Apai, P. S. Wehner, and D. A. Shirley,  
Phys. Rev. B14, 3273 (1976).
- 39) L. F. Wagner, Z. Hussain, C. S. Fadley and R. J. Baird, to appear  
in Solid State Communications.
- 40) E. Uggerhøj and J. U. Andersen, Canadian J. of Phys. 46, 543 (1968).
- 41) E. G. McRae and C. W. Caldwell, Surf. Sci. 2, 509 (1964).
- 42) J. L. Robins, R. L. Gerlach, and T. N. Rhodin, Appl. Phys. Lett.  
8, 12 (1966).
- 43) R. Baudoing, R. M. Stern, and H. Taub, Surf. Sci. 11, 255 (1968).
- 44) N. V. Smith and M. N. Traum, Phys. Rev. Lett. 31, 1247 (1973);  
M. M. Traum, N. V. Smith and F. J. DiSalvo, Phys. Rev. Lett. 32,

1241 (1974).

- 45) L. F. Wagner, Z. Hussain, and C. S. Fadley, to appear in *Solid State Communications*.

Figure II-1 - Definitions of the various angles involved in the XPS experiment. The angle  $\alpha$  is held fixed in most present instruments. The radiation is assumed to be randomly polarized.

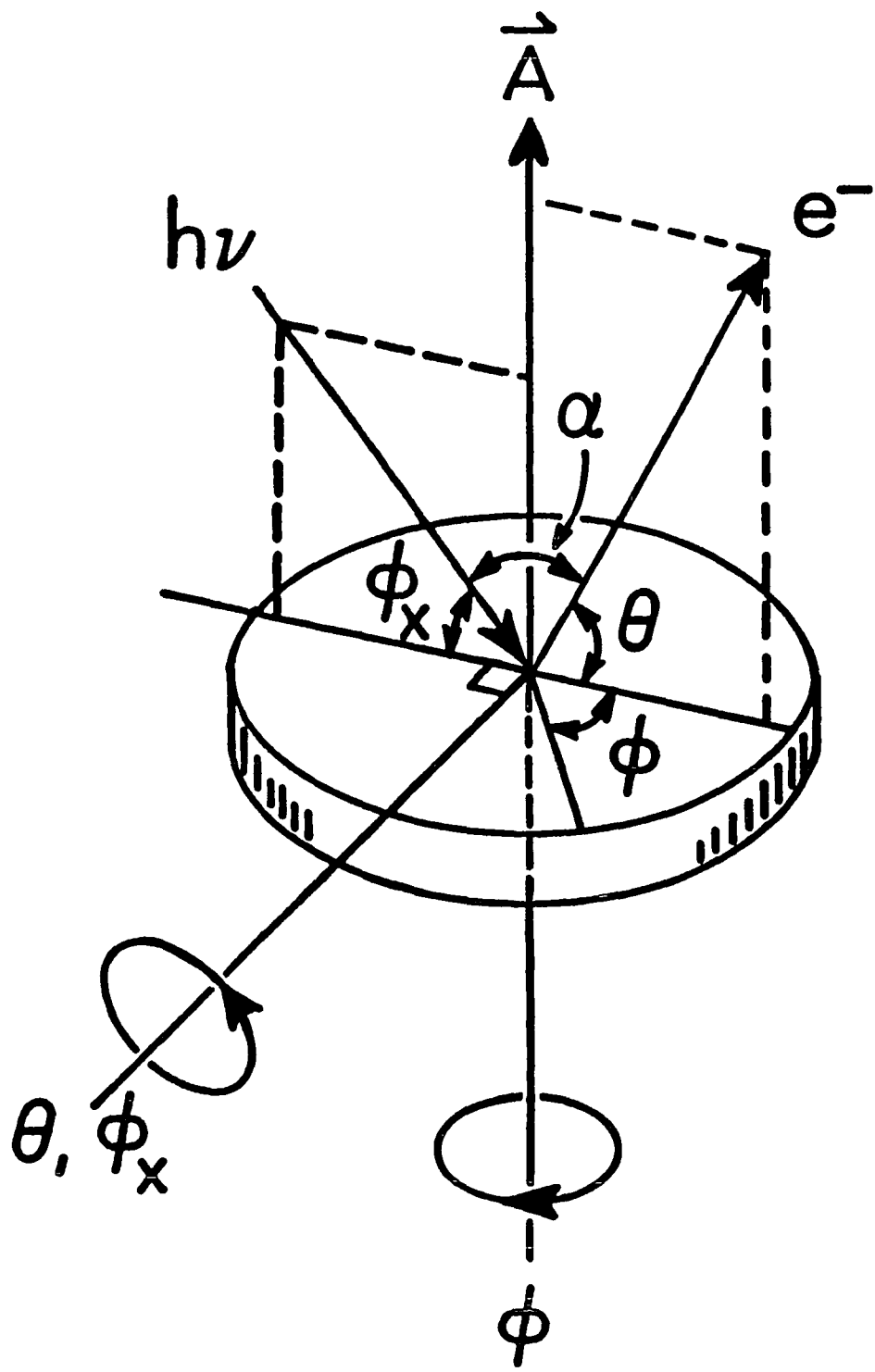


Figure II-2 - A general spectrometer geometry. The various quantities noted are defined in detail in the text (see in particular Section II.2.A)

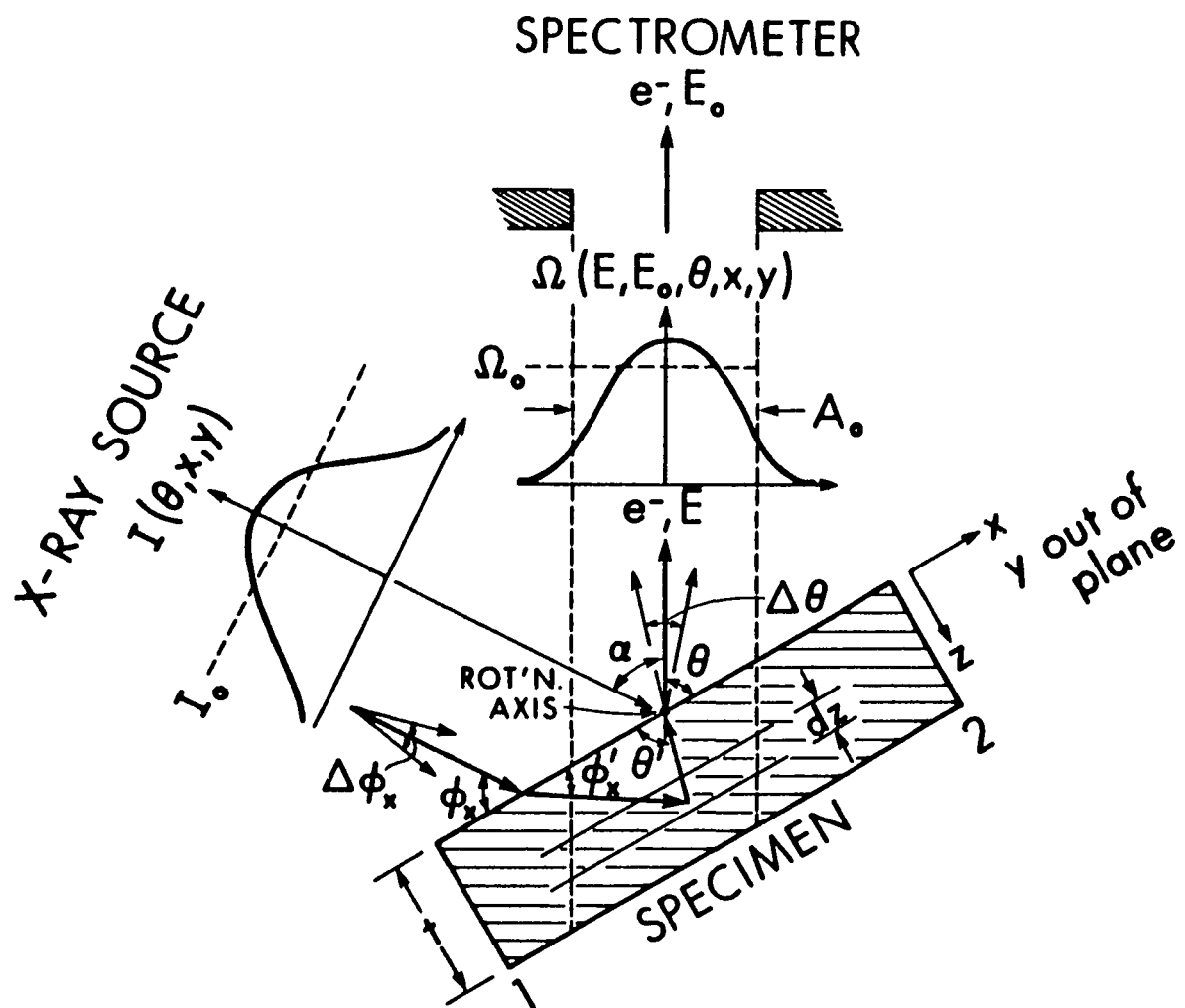
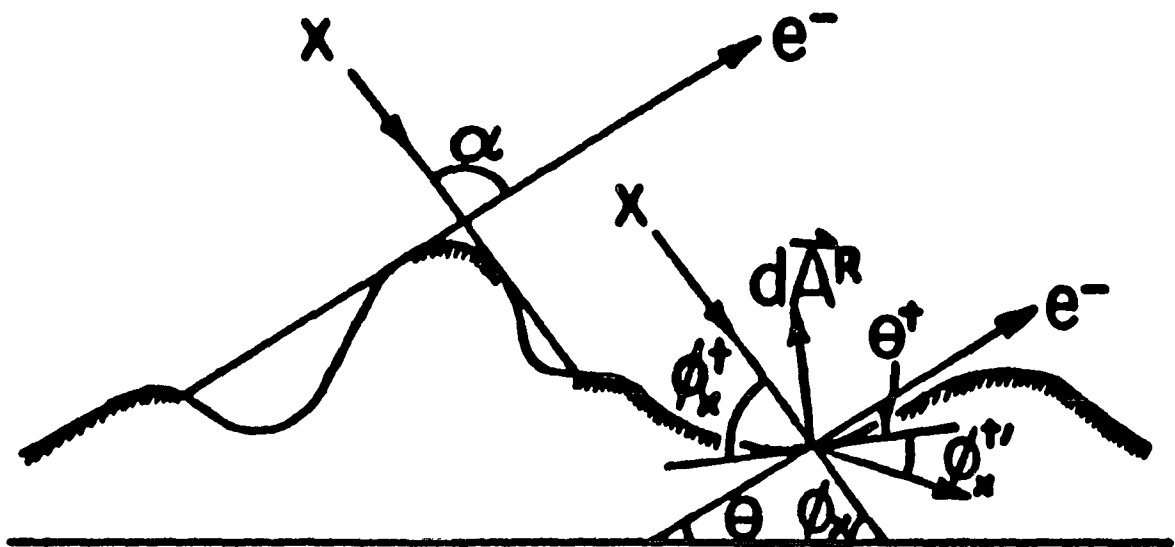


Figure II-3 - The profile of an arbitrary rough surface, defining both the gross experimental angles  $\theta$  and  $\phi_x$  and the true angles of  $\theta^t$ ,  $\phi_x^t$ , and  $\phi_x^{t'}$  for emission from a differential element of area  $dA^R$ . Complete shading of both x-rays and electrons is assumed, so that only surface area shown with cross-hatching is active in producing photoelectrons.



### III. EXPERIMENTAL

#### 1. Instrument Modifications

All of the XPS experiments reported in this thesis were carried out with a Hewlett-Packard 5950A photoelectron spectrometer modified so as to permit in situ sample rotation. Two different sample holder/inlet systems were used in these studies. The first sample probe was fully compatible with the standard Hewlett-Packard sliding-seal inlet system, but vacuum capability was limited to  $2-4 \times 10^{-9}$  torr (the same as the standard unit) by leakage of the sliding seals. This first probe is described completely in section IV.

In order to improve vacuum conditions and to provide more flexibility in sample handling, a second probe was designed by C. S. Fadley in cooperation with others which eliminated the sliding seals. This probe consists of a heavy stainless steel specimen support tube mounted inside a long-travel all-metal bellows as shown in figures III-1 and III-2. The external end of the probe terminates in a six-way cross which provides five ports for the introduction of electrical-, motion-, and liquid-nitrogen-feedthrus. The specimen end of the probe internal to the vacuum chamber provides for the loading of up to three samples. Two of these samples can be rotated so as to vary  $\theta$ , and the third can be rotated on two axes so as to alter both  $\theta$  and  $\phi$ . The two-axis sample holder is further fitted with a heater and also has provision for liquid-nitrogen cooling so that the sample temperature can be varied from  $-195^{\circ}\text{C}$  to  $1000^{\circ}\text{C}$ . Figure III-3 shows the specimen end of the support tube and the sample holders. Figure III-4 shows a more

detailed view of the two-axis sample mount. This device is connected by two concentric driveshafts to a precision rotary- and linear-motion feedthru mounted on the six-way cross (see figures III-1 and III-2). The linear motion actuates a clutch mechanism that, in two different manually set positions, permits effecting either  $\theta$  or  $\phi$  variation with the rotary motion of the feedthru. The clutch appears on the right in figure III-4. The rotary motion is in turn driven by a precision stepping motor that was interfaced as part of this thesis to an on-line HP 2100A computer. Thus, either polar or azimuthal angular distributions can easily be obtained with an angular accuracy of  $\pm 1^\circ$ .

During the course of this work, several other modifications and additions were made to the spectrometer system by the author and various co-workers in order to improve its reliability, versatility, and vacuum capability: 1) the alignment arm in the analyzer (see figure III-1) which engages the end of the specimen support tube was fitted with a beryllium-copper sleeve to eliminate galling of the probe tip. 2) The isolable sample preparation chamber was fitted with a quadrupole mass spectrometer (Uthe Model 100C), a gas inlet system, an ion gun (PHI Model 20-005F), and an ultra-high-vacuum compatible deposition unit (designed by J. M. Hill). 3) The pumping speed of the system was increased by replacing the 30  $\ell$ /sec ion pump on the sample preparation chamber with a 60  $\ell$ /sec ion pump and a titanium sublimation pump (TSP #2 in figure III-1), and by adding a titanium sublimation pump to the main spectrometer chamber (TSP #1 in figure III-1). 4) A box-like demountable oven (designed by L. F. Wagner) and an ultrahigh vacuum roughing system

for use during pumpdown and bakeout were also added. 5) A final major improvement made by the author was the interfacing of the HP2100A mini-computer to a much more versatile PDP11/45 system in the Chemistry Department, thereby permitting direct data transfers and various types of data analyses to be performed.

In preparation for ultrahigh-vacuum operation, the main spectrometer chamber was baked at 150°C according to the manufacturer's limit. The sample preparation chamber was baked at 250°C. After several days of bakeout at these temperatures, the vacuum system reached a base pressure of  $5 \times 10^{-11}$  torr after cooling. After sample cleaning and/or other gas exposures, the operating pressure of the system was generally in the range of  $1-3 \times 10^{-10}$  torr.

## 2. Electron Optical Calculations

As shown in figure III-1, the analyzer of the Hewlett-Packard 5950A spectrometer includes an electrostatic lens which serves both to project an image of the sample into the entrance plane of a hemispherical analyzer and to retard the photoelectrons to a constant mean energy of analysis. The full role of the lens in the operation of the dispersion-compensating x-ray- and electron-optics of the analyzer is discussed in section IV. In this section, the results of some electron trajectory calculation are presented which allow the solid angle of acceptance, the magnification, and the focal properties of the lens to be investigated as a function of electron kinetic energy.

The electron trajectory calculations were carried out using a standard electron-optics computer program<sup>1</sup> and the lens dimensions

supplied by H. Weaver of the Hewlett-Packard Co.<sup>2</sup>. Calculations were performed for the kinetic energy range 200-1500 eV for both the standard mode of lens operation and for a lower-magnification mode that was developed as part of this thesis and found to be useful in AD studies.

The lens system in the analyzer is a four-element, cylindrically symmetric, electrostatic lens fitted with an internal diaphragm located within the third element to limit its angular acceptance. The overall geometry of the lens is given by the outlines in figures III-5 - III-8, on which the vertical scale has been expanded by 2.5x for clarity. A similar lens system for electron transport and image formation has been discussed by Kurepa and co-workers<sup>3</sup>. The operating potentials of the lens elements are given in table III-1 with the potentials numbered as in figure III-5b.

Table III-1

## Operating Potentials of the Electrostatic Lens

	Standard Magnification	Low Magnification
$V_1$	0V	0V
$V_2$	+1250V	+1250v
$V_3$	.897( $V_4 + 90$ )V	.987( $V_4+1076$ )V
$V_4$	(115 - $E_{kin}$ )V	(115 - $E_{kin}$ )V

Figures III-5 - III-8 show representative trajectory calculations at kinetic energies of 1500, 1000, 500, and 200 eV for both modes of lens operation. In these figures one-half of a plane passing through the axis of symmetry of the lens is shown. The horizontal axis is the distance along the axis of symmetry (optic axis) of the lens and the vertical axis is the radial distance from the optic axis. The trajectories originate at one on-axis and one off-axis specimen point at the left and are directed toward the right where the entrance plane of the hemispherical analyzer is located at 155.0 on the horizontal axis. Five trajectories equally spaced in initial emission angle emanate from each source point; those with the largest angles relative to the optic axis are chosen such that they just pass through the diaphragm aperture. Those trajectories which cross the optic axis are reflected at the axis in the calculation to keep them within the half-plane that is shown in the figures. Reasonably good point-to-point focusing between the source and the analyzer entry plane is evident for kinetic energies from 500-1500 eV, but the trajectories at lower values such as 200 eV exhibit significant defocusing.

Quantitative results derived from families of such trajectories for the half-angle of acceptance  $\theta_{1/2}$  (which defines the acceptance cone), the corresponding solid angle  $\Omega$ , and the magnification  $M$  are given in table III-2. As can be seen from this table, the magnification of the lens varies less than 10% over the kinetic energy range 500-1500 eV for either mode of lens operation. The negative sign on the magnification indicates the lens forms an inverted image of the sample, as can be

seen in figures III-5 - III-8. The lens magnifications found from the trajectory calculations are somewhat smaller in absolute value

Table III-2

Conical half-angle of acceptance ( $\theta_{1/2}$ ),  
solid angle of acceptance ( $\Omega$ ),  
and lens magnification (M) as  
a function of electron kinetic energy.

$E_{kin}$ (eV)	Standard Magnification			Low Magnification		
	$\theta_{1/2}$ ( $^{\circ}$ )	$\Omega$ (steradians) $\times 10^2$	M	$\theta_{1/2}$ ( $^{\circ}$ )	$\Omega$ (steradians) $\times 10^2$	M
200	10	-	-	10	-	-
400	7.50	5.38	-	5.75	3.16	-
500	6.29	3.42	-5.0	4.75	2.16	-1.6
600	5.25	2.64	-5.0	4.15	1.65	-1.7
700	4.76	2.19	-	3.75	1.35	-
800	4.50	1.94	-4.7	3.53	1.19	-1.7
900	4.25	1.-3	-	3.38	1.09	-
1000	4.05	1.57	-4.6	3.40	1.11	-1.8
1100	3.95	1.49	-	3.10	0.92	-
1200	3.80	1.38	-4.7	3.00	0.86	-1.8
1300	3.75	1.35	-	2.98	0.85	-
1400	3.68	1.30	-4.7	2.88	0.79	-1.8
1500	3.60	1.24	-4.7	2.80	0.75	-1.8

than the magnifications determined from experimental measurements of the image size along the y (out of plane) coordinate in the multichannel

detector at the exit plane of the hemispherical analyzer. The experimental values for these magnifications are -5.0 for the standard mode of operation and -2.3 for the low-magnification mode. The discrepancy between these two sets of values may be caused by distortions of the image introduced between the entrance plane of the hemispherical analyzer and its final display as the output of a videcon camera.

Unlike the lens magnification, the solid angle of acceptance of the lens is a strong function of electron kinetic energy as shown in figure III-9. The angle of acceptance is greatly increased at low kinetic energies by the strong acceleration in the first lens gap which tends to gather in a very large cone of trajectories. However, for kinetic energies less than  $\sim 400$  V, the first lens becomes too strongly focusing, thus resulting in poor image formation at the entrance plane of the analyzer, as can be seen in figure III-8. As a result of the large angle of acceptance and poor focal properties at low kinetic energies, the internal lens aperture no longer limits the angular acceptance, and the entrance aperture of the hemispherical analyzer (a rectangular opening  $\sim 2.5$  cm x 0.6 cm) becomes the limiting aperture.

The solid angles of acceptance in table III-2 can be related to the energy-dependent factor  $F(E_0/E)$  in the spectrometer response function given by equation II-16, in which  $E$  is the kinetic energy upon leaving the specimen and  $E_0$  is the energy of analysis. One of the principal effects incorporated into  $F(E_0/E)$  is any change in overall sensitivity due to retardation; estimates of such effects for a few idealized non-absorbing geometries have been made in the past using Abbe's sine law<sup>5</sup>

and the more approximate Lagrange-Helmholtz equation<sup>6</sup>. For the present more complex case with an absorbing diaphragm, if it is assumed that the solid angle of acceptance of the lens is independent of  $x$  and  $y$  (as has been verified by trajectory calculations) and that all trajectories passing through the diaphragm (and thus contributing to the image) continue uninterrupted by collisions with the hemispheres to the detector, then  $F(E_0/E)$  will simply be proportional to the solid angle of acceptance over the range of energies for which focusing occurs and the lens diaphragm limits the acceptance<sup>4</sup>. However, for this case, the separation of energy-dependent factors in equation II-15 is not complete due to the energy dependence of the lens magnification which in turn causes the effective area of the sample to vary with kinetic energy. The overall intensity of photoelectrons detected from the sample will not necessarily scale directly with this area change due to the non-uniform peaked character of the x-ray flux across the sample. But since the magnification changes are small, the angular acceptances given here should provide a good estimate of  $F(E_0/E)$  for later use in quantitative peak intensity comparisons.

In summary, these trajectory calculations verify the focal properties and magnification of the lens in both modes of operation, and indicate that for kinetic energies greater than 500 eV a sharp focus is achieved. The solid angle of acceptance is shown to be strongly dependent on kinetic energy. Furthermore, this acceptance solid angle can be rather directly related to  $F(E_0/E)$ , the energy-dependent part of the response function, although small corrections due to the change

in magnification with energy may be necessary. Also, the conical angle of acceptance listed in table III-2 is an important parameter in the investigation of microscopic effects in XPS AD studies, where this angle limits the resolution of fine structure in Kikuchi-band effects and also determines the minimum region in  $\vec{k}$  space sampled in angle-resolved valence-band experiments.

REFERENCES  
SECTION III

- 1) W. B. Hermannsfeldt, Electron Trajectory Program, SLAC Report No. 166, National Technical Information Service, U.S. Department of Commerce, Springfield, Va. 22151 (1973).
- 2) H. Weaver, private communication.
- 3) M. V. Kurepa, M. D. Tasić, and J. M. Kurepa, Journal of Physics, E7, 940 (1974).
- 4) C. S. Fadley, in Progress in Solid State Chemistry, G. Somorjai and J. O. McCaldin, Ed., Pergamon Press, New York (1976).
- 5) O. Klemperer, Electron Optics, Cambridge University Press, London, 1953 Second Edition.
- 6) J. C. Helmer and N. H. Weichert, Appl. Phys. Letters 13, 266 (1968).

Figure III-1 - Overall schematic drawing of the experimental system used for performing angular-dependent XPS experiments at ultrahigh vacuum conditions.

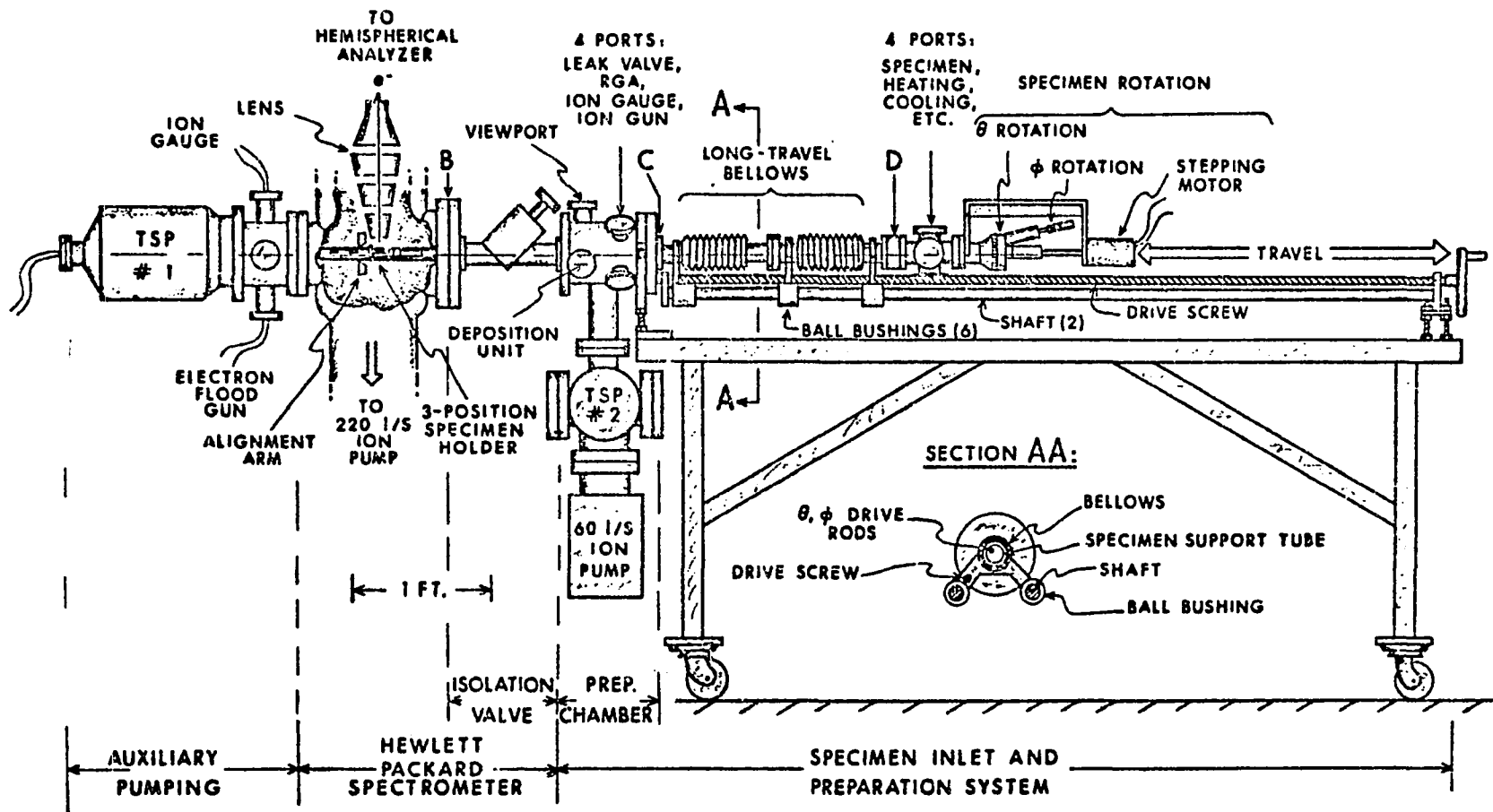


Figure III-2 - Photograph of the modified inlet system shown in the same approximate orientation as figure III-1.

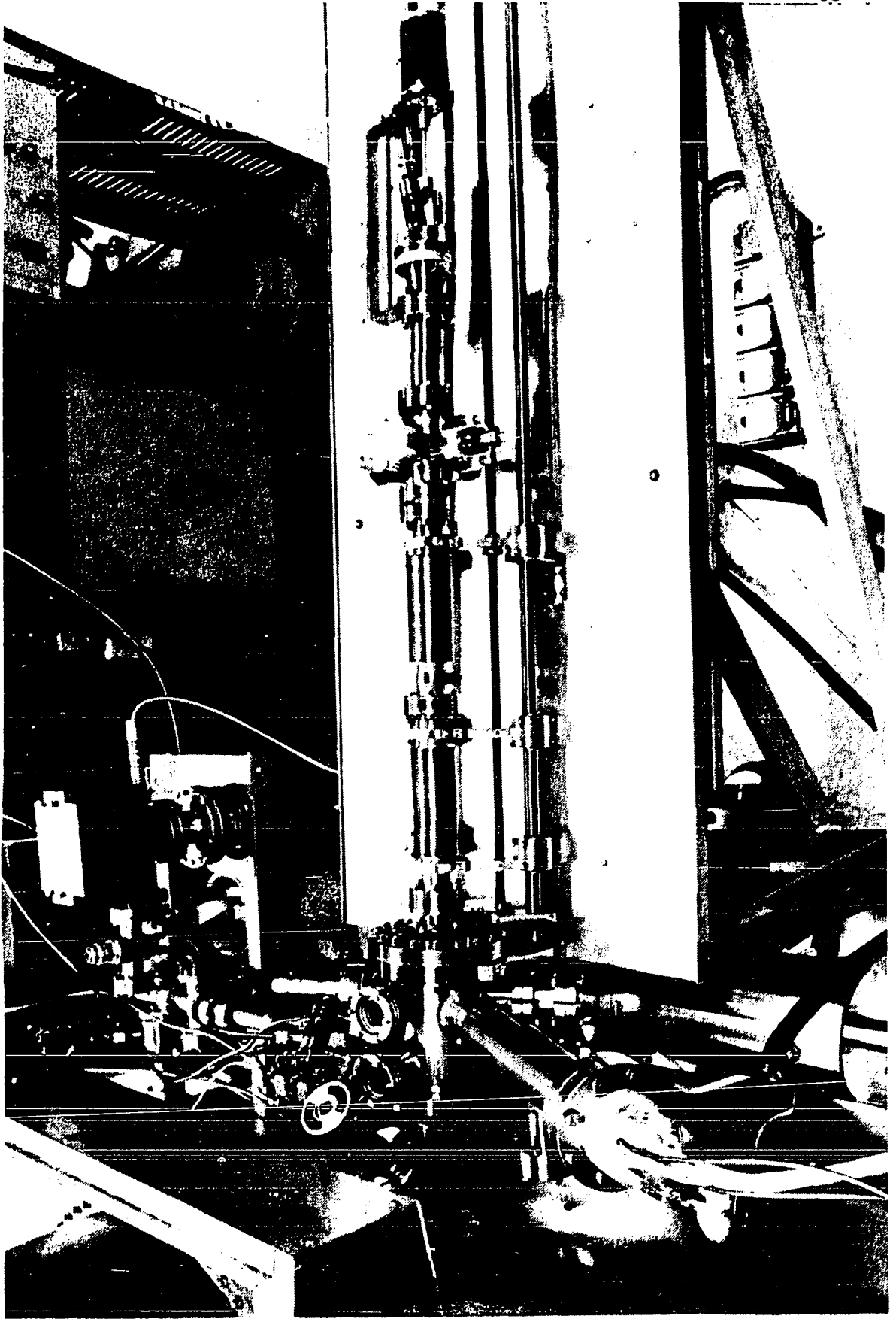


Figure III-3 - Photograph of the three-position specimen probe.

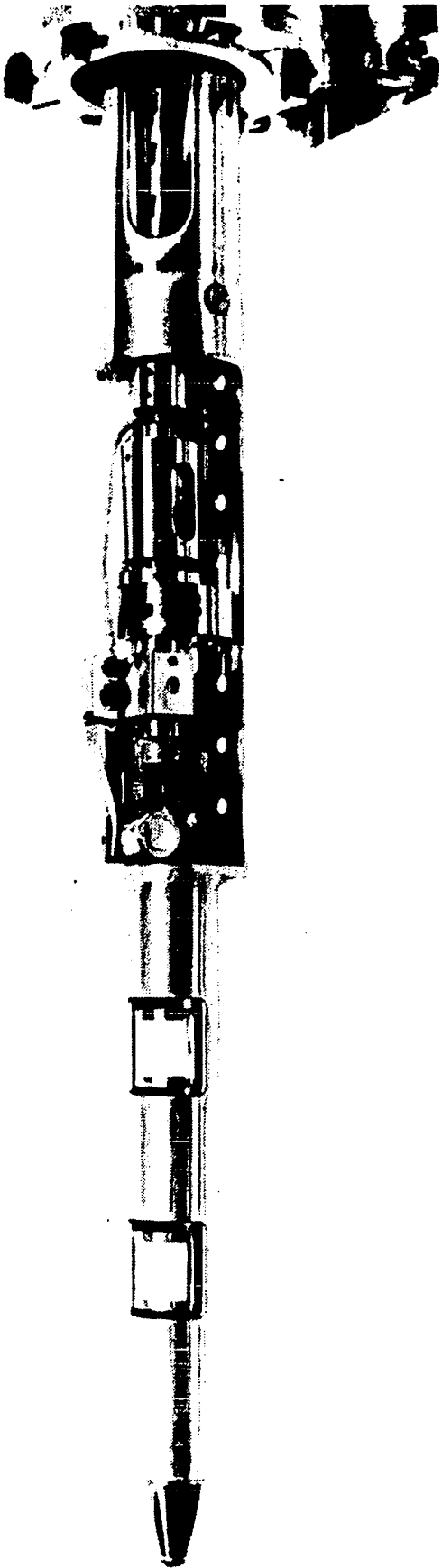


Figure III-4 - Two views of the two-axis, variable-temperature, specimen holder.

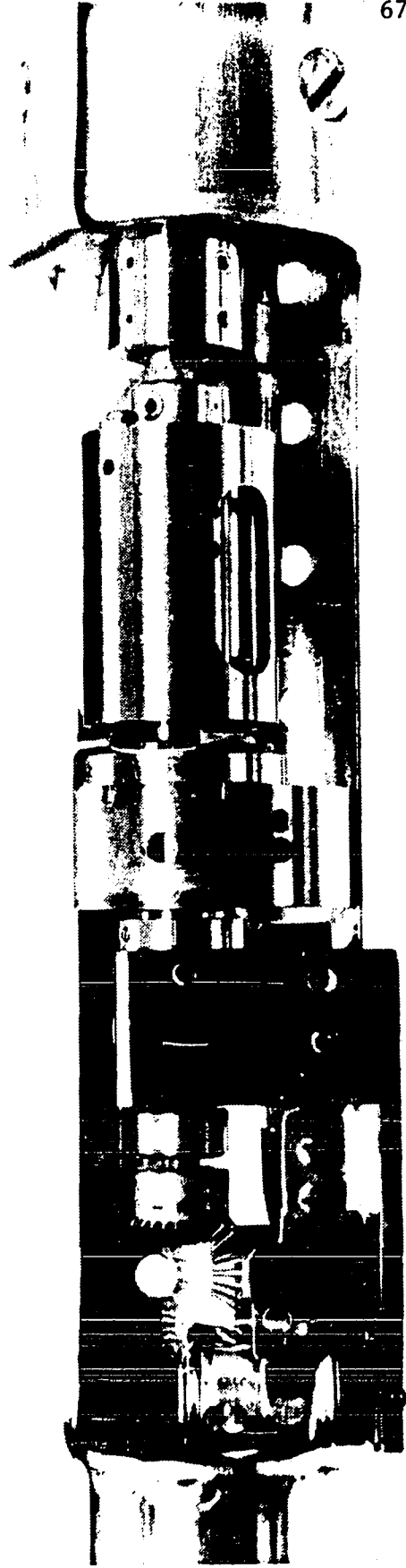
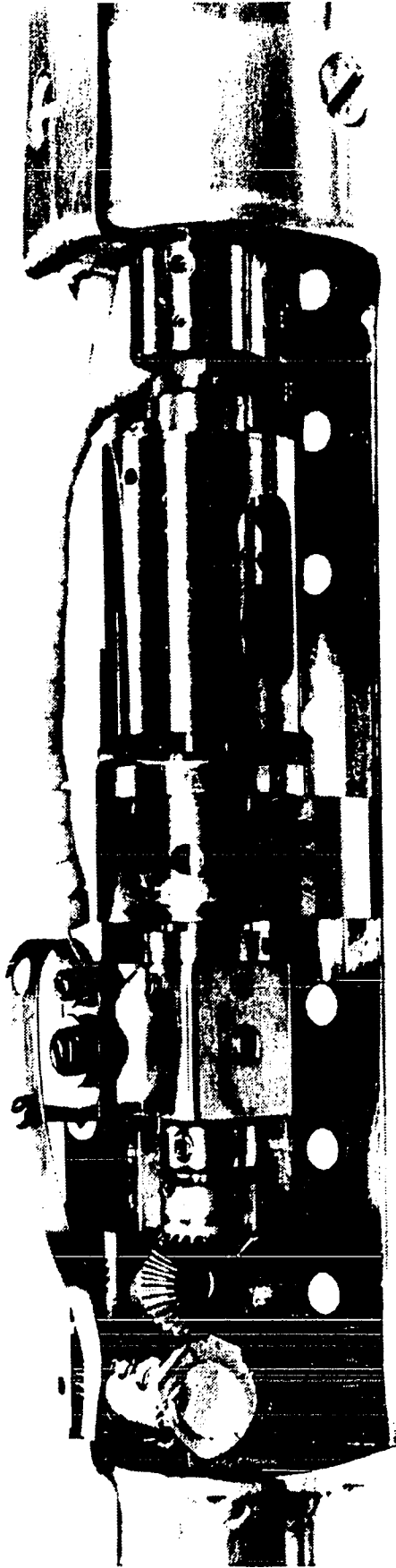


Figure II-5 - a) Representative trajectories of 1500eV electrons in the electrostatic lens at standard magnification ( $M \sim -5$ ). The trajectories start at the sample on the left and are directed toward the entrance plane of the hemispherical analyzer located at 155.0 on the horizontal axis (dotted lines). The scales are in tenths of an inch, and the y-axis has been expanded by a factor of 2.5 for clarity.

b) Trajectories of 1500 eV electrons in the lower magnification mode ( $M \sim -2$ ) of operation.

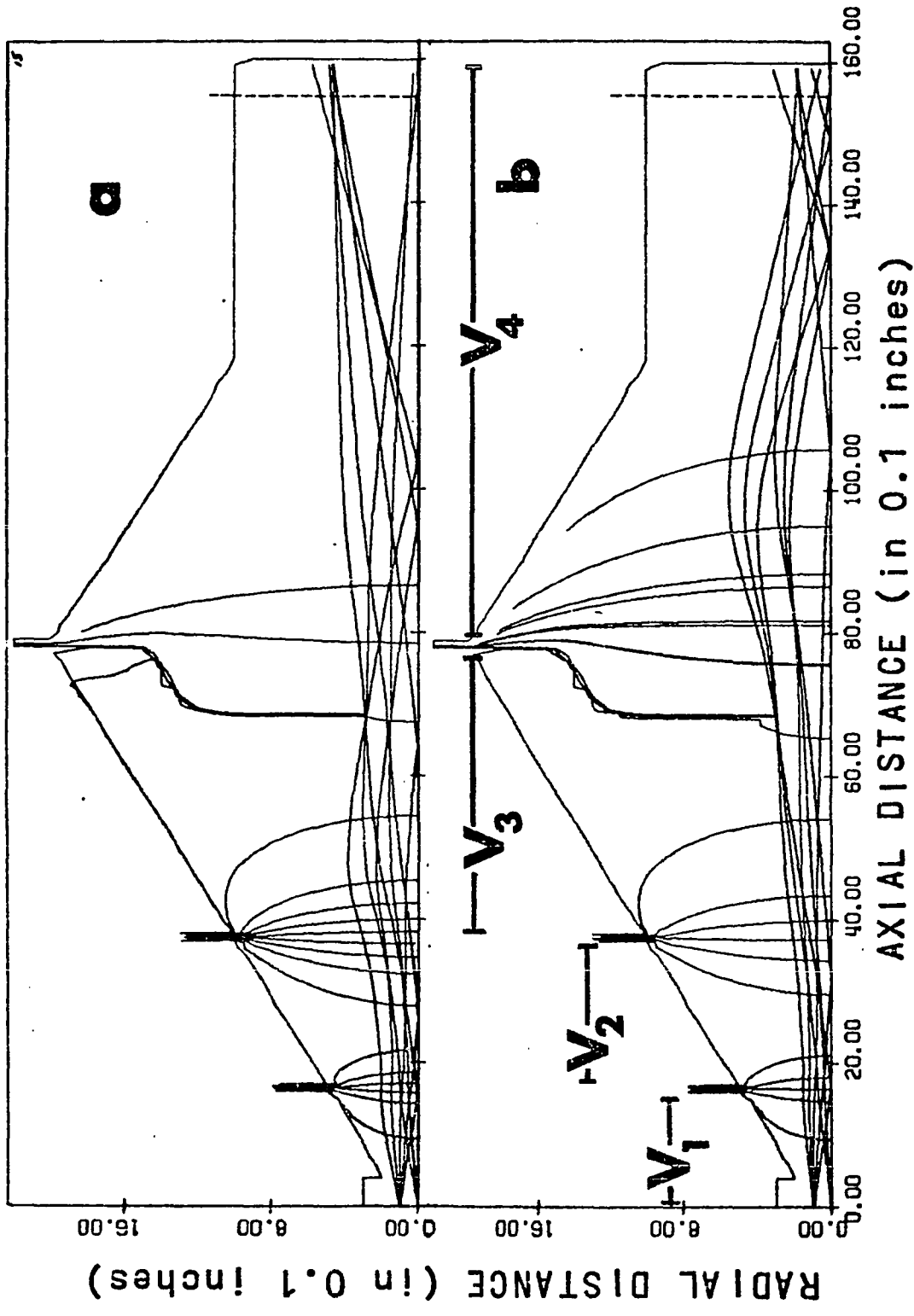


Figure III-6 - a) Representative trajectories of 1000 eV electrons at standard magnification ( $M \sim 5$ ). b) Trajectories of 500 eV electrons at low magnification ( $M \sim 2$ ).

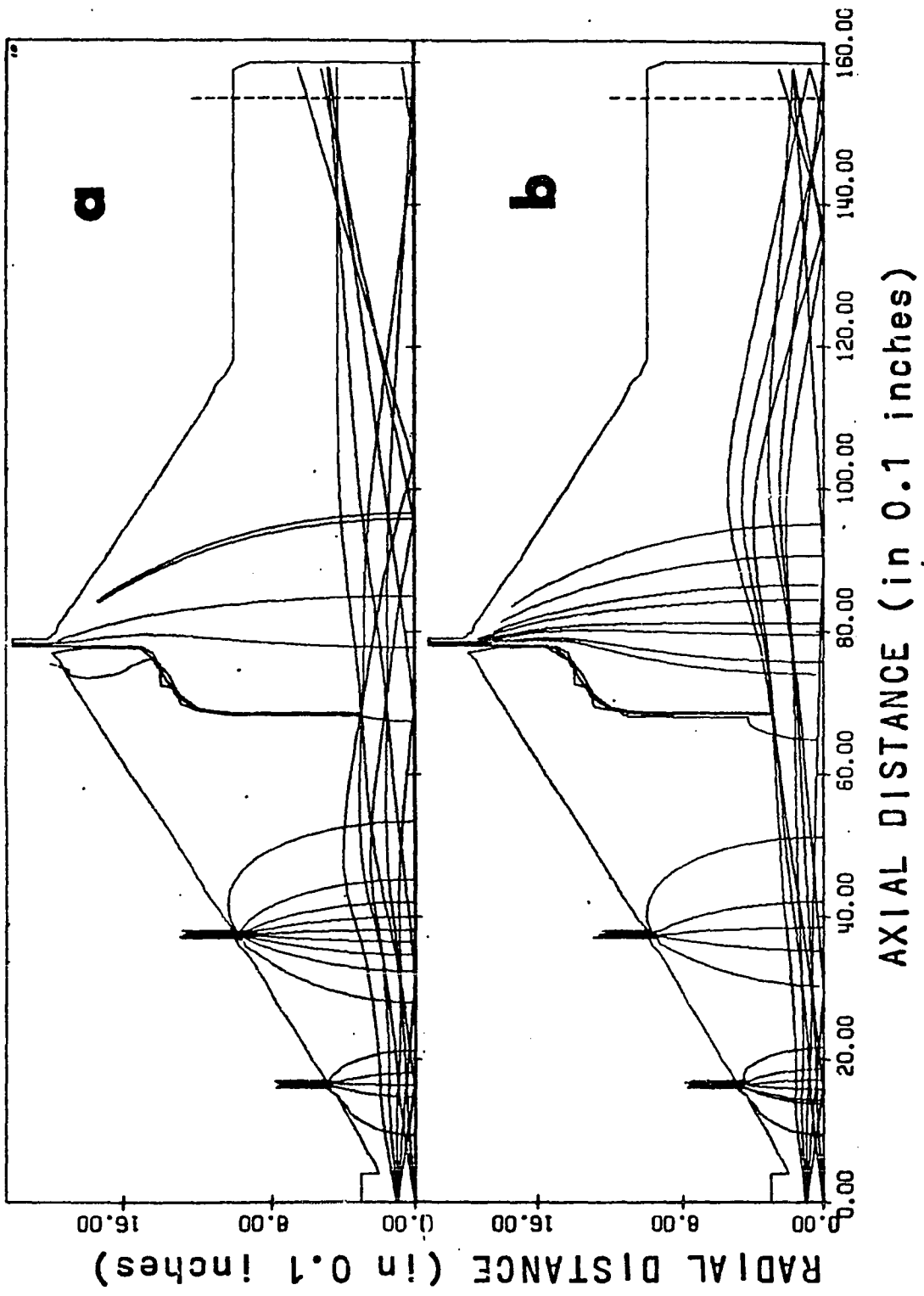


Figure II-7 - a) Representative trajectories of 500 eV electrons at standard magnification ( $M \sim -5$ ). b) Trajectories of 500 eV electrons at low magnification ( $M \sim -2$ ).

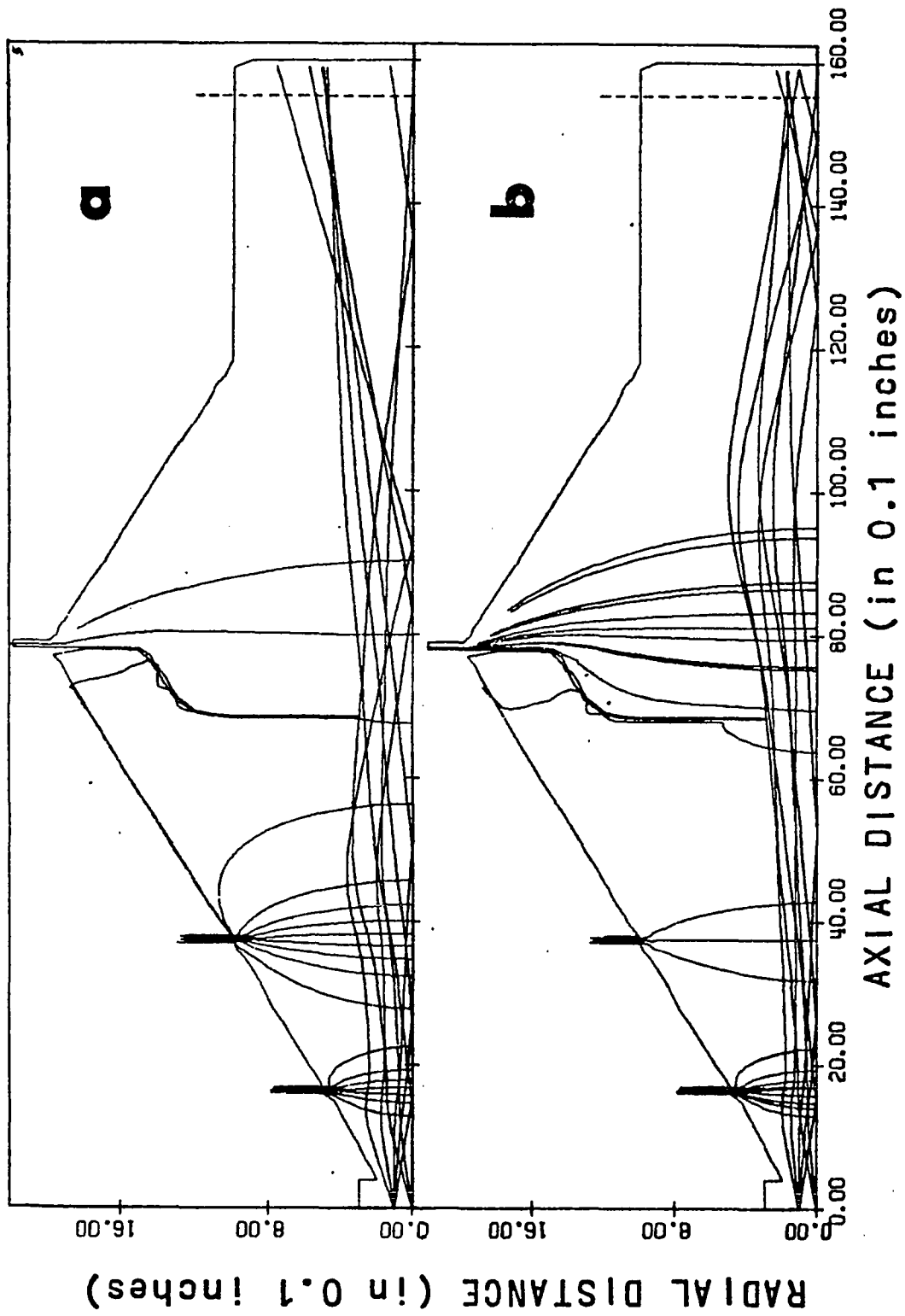


Figure III-8 - a) Representative trajectories of 200 eV electrons at standard magnification ( $M \sim -5$ ). b) Trajectories of 200 eV electrons at low magnification ( $M \sim -2$ ).

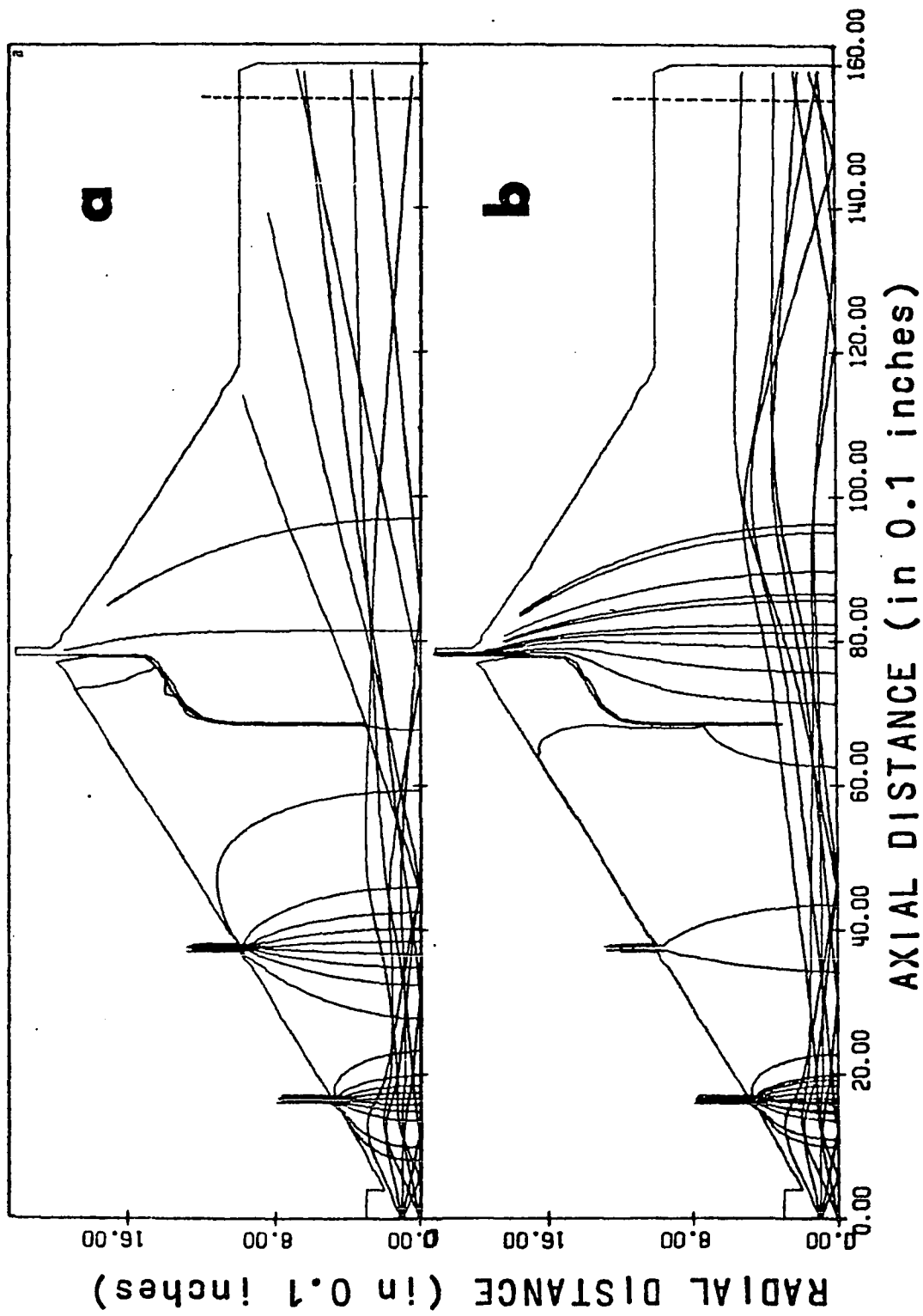
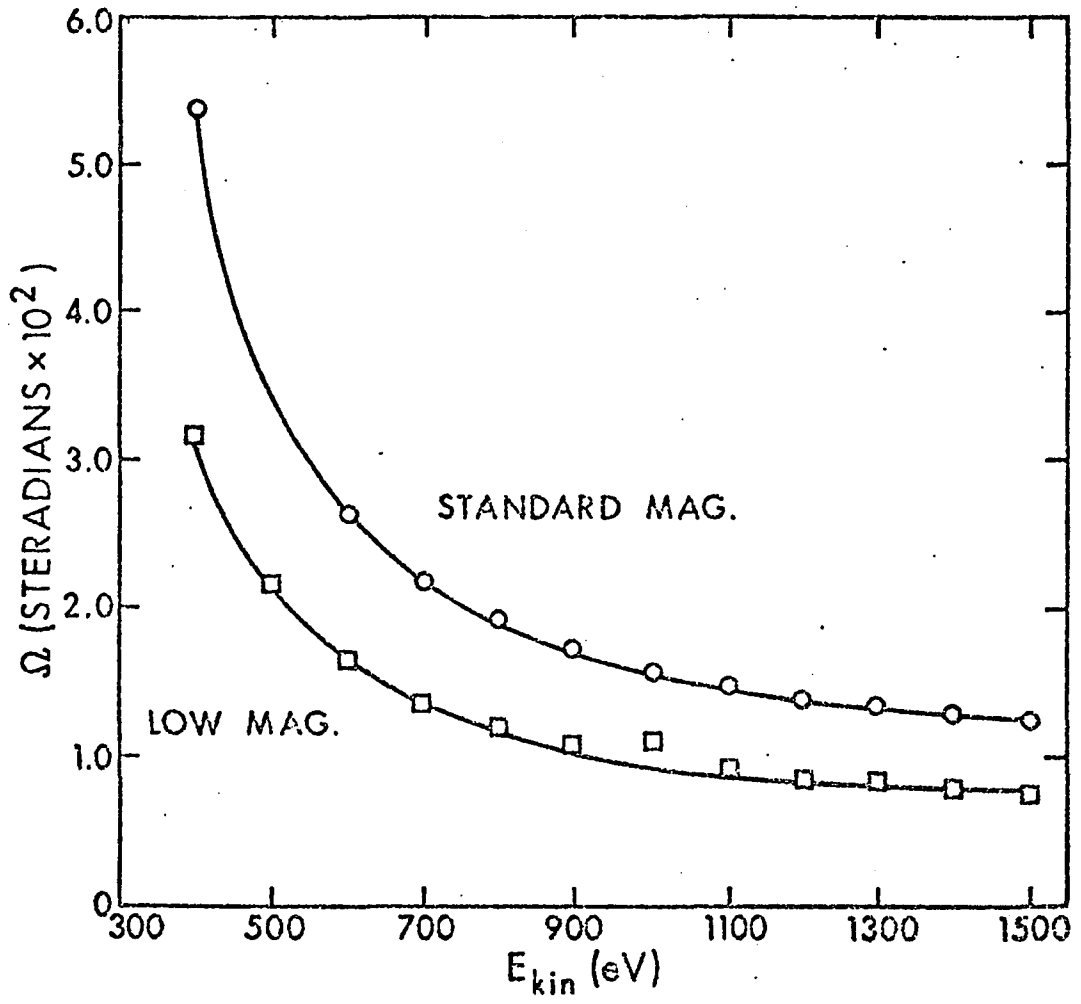


Figure III-9 - Solid angle of acceptance of the electrostatic lens as a function of kinetic energy for both standard and low magnification modes of operation.



#### IV. X-RAY-PHOTOELECTRON ANGULAR DISTRIBUTIONS WITH DISPERSION-COMPENSATING X-RAY- AND ELECTRON-OPTICS<sup>†</sup>

##### 1. Introduction

X-ray-photoelectron angular distribution (AD) measurements have been shown in a number of prior studies involving solid specimens to be capable of yielding several useful types of information beyond those derivable from energy-distribution data alone<sup>1-14</sup>. The specific phenomena noted have been: (1) the selective enhancement of surface-atom intensities for low (grazing) electron exit angles<sup>1,2,4-9,11,12</sup> or low x-ray incidence angles<sup>5,6,10,12</sup>; (2) the quantitative analysis of XPS AD data to yield parameters such as electron attenuation lengths<sup>3,4,5-7,10,12</sup>, surface-layer thicknesses<sup>4-6,12</sup>, surface concentration profiles<sup>5,6,9,11,12</sup>, and surface roughness contours<sup>5,6,8,9,11,12</sup>, and, in measurements on single-crystal specimens, (3) pronounced fine structure in angular distributions of total peak intensities<sup>1,2,7,9,12,13,14</sup>, as well as significant changes in valence-peak relative intensities with angle<sup>9,12,14</sup>, both of which effects can be related to atomic geometries and orbital symmetries. Certain basic instrumental problems associated with performing XPS AD measurements have been reviewed previously<sup>5,6,12</sup>, but no detailed investigations of the performance of a specific instrument have been carried out.

<sup>†</sup> Based on a paper "X-ray-Photoelectron Angular Distributions with Dispersion-Compensating X-ray- and Electron- Optics" by R. J. Baird and C. S. Fadley submitted to Journal of Electron Spectroscopy and Related Phenomena.

A further important instrumental consideration in XPS is that of resolution, which is primarily limited in most present systems by the natural width of the x-radiation used for excitation (for example, approximately 0.9 eV full width at half maximum intensity (FWHM) for  $\text{AlK}_{\alpha 1,2}$ <sup>15</sup>). One possibility for increasing resolution is to monochromatize the exciting x-rays by means of a crystal or grating<sup>15,16</sup>, as is now done in certain commercial XPS instruments. Such monochromatization is also an integral part of photoelectron spectroscopy utilizing synchrotron radiation<sup>17,18</sup>. A further refinement of this procedure involves matching the spatial energy dispersions of monochromator and electron energy analyzer in such a way that the two cancel one another<sup>15</sup>. The applicability of such a dispersion-compensation procedure in XPS was first demonstrated by Seigbahn et al.<sup>15</sup>, and has subsequently been implemented in a commercial system in somewhat modified form by the Hewlett-Packard Company<sup>19</sup>. Although  $\text{AlK}_{\alpha 1,2}$  radiation is used for excitation in this system, overall instrumental widths are  $\approx 0.5$  eV<sup>19</sup>. In order for dispersion compensation to be operative, however, the specimen surface has to be oriented at a unique angle with respect to the monochromator and energy analyzer<sup>15</sup>. Thus, in this particular mode of operation, some degree of resolution loss is expected to occur over much of the angle range scanned in a typical AD study.

It is thus of interest to investigate the detailed systematics of XPS angular distribution measurements as performed with instruments utilizing monochromatized radiation sources. In the present study, a

theoretical model for predicting spectrometer response as a function of electron emission angle from the specimen surface is presented. This model is developed for the case of a particular system in which dispersion compensation can occur, and numerical calculations of peak shapes, intensities, and positions as a function of angle are carried out. Corresponding experimental results are also obtained and these are directly compared with theory. Certain special equipment constructed for this study is also described.

## 2. Theory

The basic elements of the combined x-ray- and electron-optical system to be discussed are schematically shown in Figures IV-1, IV-2 and IV-3. Figure IV-1 indicates the main components, Figures IV-2(a), IV-2(b), and IV-2(c) illustrate qualitative behavior for three special specimen orientations, and Figure IV-3 defines various quantities essential for a detailed mathematical model of the system. For the special case of operation with dispersion compensation shown in Figure IV-2(b), Siegbahn, Hammond, Fellner-Feldegg, and Barnett<sup>19</sup> have discussed the design, construction, and performance of the basic components, and we therefore present only a brief review here. Various critical dimensions and parameters (including several determined as part of the present study) are presented in Table IV-1. The x-ray monochromator consists of three-spherically-bent quartz crystals aligned vertically along the y direction (as defined in Figure IV-3). In optimum alignment, the three Rowland circles associated with these crystals intersect in a point lying both in the center of the specimen

surface and also somewhere along the central axis of a regarding and imaging electron lens. The x-ray flux is thus spatially dispersed in energy along a direction perpendicular to the mean propagation direction. The quantity  $2\Delta(h\nu)$  of Figures IV-1 and IV-2 represents the energy spread of the x-ray line after passing the monochromator, and will be less than or equal to the natural width of the line. Photoelectrons emitted from the planar specimen surface pass through the four-element electrostatic lens which forms a magnified, inverted image of the specimen in the equatorial plane of a hemispherical analyzer; this lens furthermore retards the electrons from some initial kinetic energy  $E$  to a constant mean energy of analysis  $E_0$ . The lens magnification is held constant for all input kinetic energies  $E$  and is denoted by  $-M$ . The entrance aperture in the equatorial plane of the hemispherical analyzer is effectively rectangular and has fixed dimensions of  $\Delta r_0$  and  $y_0$ . After passing through the analyzer, electrons are counted in a multichannel detector system.

We shall be concerned only with angular distribution measurements performed by rotating the specimen on an axis that lies in its surface and is also perpendicular to the planes of Figures IV-1 - IV-3 (that is, parallel to the  $y$  axis). For simplicity, Figures IV-1 and IV-2 are drawn with the specimen rotation axis intersecting the central lens axis (which also defines a central reference trajectory indicated by dotted lines in Figures IV-2 and IV-3). Figure IV-3 allows for a more general alignment of the specimen rotation axis, as does our final theoretical model. The angle  $\theta$  lies between the electron emission direction and the

specimen surface. The x-ray incidence angle is similarly defined and is denoted by  $\phi_x$ . The relative spatial orientation of the x-ray- and electron<sup>a</sup> optical elements is held fixed, and the constant angle between the mean x-ray propagation direction and the lens axis or central reference trajectory is denoted by  $\alpha$ . Thus, specimen rotation simultaneously varies both  $\theta$  and  $\phi_x$ , but in opposite directions. The two angles are simply related by  $\phi_x = \pi - \alpha - \theta$ , and we shall arbitrarily take  $\phi_x$  to be the dependent variable.

Dispersion compensation occurs for the specimen orientation shown schematically in Figure IV-2(b). Although different points on the specimen surface are illuminated with different photon energies spanning a range of  $2\Delta(h\nu)$ , each point is ideally imaged by the lens to a radial position within the entrance aperture of the analyzer such that its final radial image position in the detection plane is identical to that of any other point on the surface. The proper specimen orientation is critical in precisely matching the monochromator- and lens-analyzer-dispersions. The angle at which dispersion compensation occurs will be denoted by  $\theta_0$ .

If the specimen angle is varied in either direction away from  $\theta_0$ , two rather important and easily visualized limits are reached: (1) In the limit for which  $\theta$  goes to zero, the radial width of the specimen image formed by the lens in the entrance aperture also tends to zero (Figure IV-2(a)). In this limit, the hemispherical analyzer appears to have a zero-width electron source in its equatorial plane that has been generated by illumination with all energies over the range  $2\Delta(h\nu)$ .

Dispersion compensation is thus completely lost, and the overall instrumental width is determined primarily by the effective x-ray line width, much as in more standard systems without monochromatization. (For the case shown in Figure IV-2(a), however, photoelectron intensity due to x-ray satellite lines and bremsstrahlung radiation would not be present.) The low- $\theta$  limit of instrumental line width should thus be independent of changes in both the lens magnification and the aperture size, and should be given by a convolution of line width contributions from the x-ray source and non-idealities in the lens, the analyzer, and the multi-channel detector. (2) In the limit for which  $\theta$  is increased such that the x-ray incidence angle  $\alpha_x$  goes to zero (Figure IV-2(c)), the spread of photon energies over that portion of the specimen surface from which electrons can finally be accepted into the analyzer ( $\Delta h$ ) goes to zero, and furthermore, the entrance aperture is completely and very uniformly illuminated by electrons. Thus, the hemispherical analyzer appears to have a uniform, monoenergetically-excited source of electrons over its entire entrance aperture, and the radial width of the aperture  $r_0$  is directly translated into the final peak width observed in the detection plane. The resolution in this high- $\theta$ /low  $\alpha_x$  limit thus depends primarily on the aperture width  $r_0$  (converted into an energy spread via the dispersion equation for the analyzer) as taken in convolution with the lens-, analyzer-, and detector-linewidth contributions. Changes in the

lens magnification should have little effect on this limit.

The two limits discussed above have the further significance that they occur very near angles for which the photoelectron intensity becomes zero. That is, if  $\theta$  is decreased beyond zero, the specimen surface shades itself from the lens/analyzer/detector system, and if  $\phi_x$  is decreased beyond zero, the surface shades itself from the monochromator.

A quantitative and more general description of the range of phenomena represented by Figure IV-2 can be achieved in terms of a mathematical model that predicts the shapes, widths, positions, and intensities of photoelectron peaks as a function of  $\theta$ . No detailed discussion of the equations describing the system shown in Figures IV-1 - IV-3 has been presented previously. Several quantities essential to this model are defined in Figure IV-3. (Wherever applicable, we have used notation in agreement with that in recent discussions of XPS angular distribution studies<sup>5,6,9,12</sup>.)

The basic aim of this model is to calculate for an arbitrary value of  $\theta$  a purely instrumental response function giving the photoelectron intensity at a certain value of energy as measured in the detection plane. We shall measure energy and various other quantities relative to the central reference trajectory shown in Figure IV-3, indicating the apparent energy difference of an arbitrary trajectory from that of the reference by  $\Delta E$ . The response function can thus be denoted by  $R'(\theta, \Delta E)$  and a schematic plot of it against  $\Delta E$  is shown in Figure IV-3.  $R'(\theta, \Delta E)$  should thus contain all purely instrumental contributions to peak shapes, widths, positions, and intensities. For example, a shift

in the value of  $\Delta E$  corresponding to the maximum in  $R'(\theta, \Delta E)$  from one  $\theta$  value to another will yield a purely instrumental peak shift with angle.

Integrating  $R'(\theta, \Delta E)$  over  $\Delta E$  yields a total intensity response function  $R(\theta)$  that is necessary for absolute intensity analyses in connection with angular distribution measurements:

$$R(\theta) = \int R'(\theta, \Delta E) d(\Delta E) \quad (\text{IV-1})$$

This response function has been discussed previously<sup>5,6,8,9,12</sup> and it is easily calculated provided that, for any point on the specimen surface, both the incident x-ray flux  $I_x$  and the true solid angle of acceptance into the electron spectrometer  $\Omega$  are known. For the present case, if a Cartesian coordinate system is centered at the intersection of the central reference trajectory with the specimen surface and oriented such that the x direction lies along the surface and in the plane of Figure IV-3, the y direction is perpendicular to this plane, and the z direction is perpendicular to the specimen surface, then the position of any point on the surface with respect to the x-ray- and electron-optical system can be uniquely specified by the coordinates  $\theta$ ,  $x$ , and  $y$ . Thus, the x-ray flux and solid angle can be expressed as  $I_x(\theta, x, y)$  and  $\Omega(\theta, x, y)$ , and the total-intensity response function  $R(\theta)$  can be shown to be<sup>5,6,12</sup>:

$$R(\theta) \equiv \sin\theta \iint_A I_x(\theta, x, y) \Omega(\theta, x, y) dx dy, \quad (\text{IV-2})$$

in which  $A$  is the total planar surface area of the specimen. For an infinitely thick, homogeneous specimen with a perfectly flat and

uncontaminated surface, the total photoelectron intensity in a peak originating from the kth level will vary with  $\theta$  according to<sup>5,6,12</sup>:

$$N_{\infty}(\theta) = D_0 \cdot F(E_0/E) \cdot \rho \cdot \left[ d\sigma_k/d\Omega \right] \cdot \Lambda_e(E) \cdot R(\theta). \quad (\text{IV-3})$$

$N_{\infty}(\theta)$  is the k intensity for an infinitely thick specimen,  $D_0$  is the efficiency of the detector,  $F(E_0/E)$  is a function allowing for possible intensity loss due to retardation,  $\rho$  is the density of the atom on which the kth level is located,  $d\sigma_k/d\Omega$  is the differential photoelectric cross section, and  $\Lambda_e(E)$  is the energy-dependent electron attenuation length. The  $\sin\theta$  factor in equation IV-2 arises in integrating for total intensity over  $z$ , and allows for the fact that the average depth perpendicular to the surface that is effective in producing no-loss photoelectrons is  $\Lambda_e \sin\theta$ <sup>5,12</sup>.

In incorporating the energy parameter  $\Delta E$  into the response function  $R'(\theta, \Delta E)$ , it is necessary to determine only the apparent energy of detection associated with photoelectron emission from each point on the specimen surface. This can be done by adding the energy shifts associated with the x-ray- and electron-optical systems, and multiplying by the differential instrumental intensity generated at a given point (which will be proportional to  $I_x(\theta, x, y) \Omega(\theta, x, y)$ ). For ideal operation of the x-ray monochromator and lens/analyzer/detector system, each point  $\theta, x, y$  on the surface will result in a unique apparent energy shift relative to the reference trajectory that can be denoted by  $\Delta E'(\theta, x, y)$ . Non-idealities in the various elements can be allowed for by introducing a normalized broadening function  $B(\Delta E, \theta, x, y)$  which gives the true distribution of intensity emitted from a point  $\theta, x, y$  and detected at

various apparent energies  $\Delta E$  that need not be equal to the ideal apparent energy  $\Delta E'(\theta, x, y)$ . For an ideal system,  $B(\Delta E, \theta, x, y)$  is given by the delta function  $\delta(\Delta E - \Delta E'(\theta, x, y))$ . The most important types of non-ideality convoluted together in  $B$  are thus: monochromator resolution limitations due to the finite number of diffracting planes, as well as crystalline and geometric aberrations<sup>19</sup>; imperfect alignment of the three separate Rowland circles involved; lack of either perfect point-to-point focusing in the lens or line-to-line focusing in the analyzer; and image blurring in the multichannel detector. The desired energy-dependent response function can thus be written as:

$$R'(\theta, \Delta E) = \sin\theta \iint_A I_x(\theta, x, y) \Omega(\theta, x, y) B(\Delta E, \theta, x, y) dx dy, \quad (\text{IV-4})$$

or, in the limit of ideal operation:

$$R'(\theta, \Delta E) = \sin\theta \iint_A I_x(\theta, x, y) \Omega(\theta, x, y) \delta(\Delta E - \Delta E'(\theta, x, y)) dx dy. \quad (\text{IV-5})$$

Equation IV-r furthermore, can be used to describe any spectrometer system, in the sense that if  $B$  includes the full x-ray linewidth, operation without monochromatization is implied, whereas if the lens broadening involves a highly distorted or defocused image, a set of conditions appropriate to more standard usage of a slitted monochromator system results. For ideal operation at  $\theta = \theta_0$  in a dispersion-compensated system,  $R'(\theta, \Delta E)$  has non-zero values only for  $\Delta E = 0$ , so that  $R'(\theta_0, \Delta E = 0) = R(\theta_0)$  as calculated from equation IV-2.

An experimental spectrum resulting from such a spectrometer will be produced by a convolution of  $R'(\theta, \Delta E)$  with the natural shape of the

kth level. This shape we shall assume to include inelastic scattering effects. If this shape is denoted by  $W_k(\Delta E - \Delta E'')$  then the spectrum from a clean, flat specimen of infinite thickness will be given by:

(IV-6)

$$N'(\theta, \Delta E) = D_0 \cdot F(E_0/E) \cdot \rho \cdot d\sigma_k/d\Omega \cdot \Lambda_e(E) \int R'(\theta, \Delta E'') W_k(\Delta E - \Delta E'') d(\Delta E'')$$

$$= D_0 \cdot F(E_0/E) \cdot \rho \cdot d\sigma_k/d\Omega \cdot \Lambda_e(E) \cdot R''(\theta, \Delta E)$$

in which

$$R''(\theta, \Delta E) = \int R'(\theta, \Delta E'') W_k(\Delta E - \Delta E'') d(\Delta E'').$$

For the special case of the  $\theta$  value giving rise to the minimum experimental linewidth,  $\theta$  should be very nearly equal to  $\theta_0$  and the only remaining contributions to linewidth should be those due to non-ideal instrumental effects as represented by  $B(\Delta E, \theta, x, y)$  and the natural shape of the level as given by  $W_k(\Delta E - \Delta E'')$ . Thus, at the minimum width condition, an experimental spectrum should be given by

$$N'(\theta_0, \Delta E) = D_0 \cdot F(E_0/E) \cdot \rho \cdot d\sigma_k/d\Omega \cdot \Lambda_e(E) \cdot R''(\theta_0, \Delta E). \quad (IV-7)$$

The spectral lineshape given by  $R''(\theta_0, \Delta E)$  can thus be obtained experimentally at the minimum linewidth angle, and convoluted with ideal theoretical results based upon equation IV-5 to permit direct comparison between experimental spectra and theoretically-generated spectra for  $\theta \neq \theta_0$ . (For  $\theta = \theta_0$ , the convolution simply regenerates the experimental spectrum, as the ideal  $R'(\theta, \Delta E)$  is proportional to  $\delta(\Delta E)$ .)

Detailed calculations with this model thus require a knowledge of  $I_x(\theta, x, y)$ ,  $\Omega(\theta, x, y)$  and  $\Delta E'(\theta, x, y)$  for all points on the specimen

surface for substitution into equation IV-5.

The dispersed x-ray flux will be most accurately described by a distribution function giving the intensity in an energy interval  $h\nu$  to  $h\nu + d(h\nu)$  for any point in space that can be occupied by the specimen surface for various choices of  $\theta$ . The basic action of the monochromator is to disperse the flux along a coordinate  $\gamma$  that is perpendicular to the mean x-ray propagation direction and also lies in the x,z plane. If the coordinate  $\delta$  points along the x-ray propagation direction, the dispersed flux can be denoted generally by the function  $I_x'(h\nu ; \gamma, \delta, y)$ . The  $\gamma, \delta$  coordinate system is thus rotated by an angle  $\theta + \alpha - \pi/2$  with respect to x,z.

The function  $I_x'(h\nu ; \gamma, \delta, y)$  thus can include all non-idealities in the monochromator, but it is reasonable to simplify it in several respects: (1) We assume that, over the region in space that can be occupied by those portions of the specimen surface active in producing detectable photoelectrons, the flux distribution does not depend on distance  $\delta$  along the x-ray propagation direction. This is reasonable if the overall angle of convergence of the x-rays on the Rowland circle is not too large (it is only approximately  $7^\circ$  for the system considered here), and if the photoelectron-active region has a small width along the x coordinate in comparison with the Rowland circle diameter (approximately 0.1-0.2 cm in comparison to 28.0 cm for the present case). With this approximation,  $I_x'(h\nu ; \gamma, \delta, y)$  becomes  $I_x'(h\nu ; \gamma, y)$ . A further assumption that will be made in performing all integrations is that  $I_x'$  is independent of y over the photoelectron-active length of the

specimen; this may be only approximately true for the specific system considered here, with one possible cause of deviations being that the three intersecting Rowland circles are tilted with respect to one another. (2) For ideal operation of the monochromator,  $h\nu$  and  $\gamma$  are furthermore related by a constant factor  $d(h\nu)/d\gamma$  that is easily shown to be:

$$\begin{aligned} \frac{d(h\nu)}{d\gamma} &= \frac{1}{C} \cdot \frac{d(h\nu)}{d\theta_B} & (IV-8) \\ &= \frac{h}{C \tan \theta_B} \end{aligned}$$

in which  $\theta_B$  is the Bragg angle and  $C$  the Rowland circle chord length (see Figure IV-1).  $\gamma$  and  $h\nu$  are thus linearly related, so that  $I_x'(h; \gamma, y)$  can be replaced simply with  $I_x'(\gamma, y)$  or  $I_x'(\Delta(h\nu), y)$  (see Figure IV-3). Because a given value of  $\gamma$  projects along the  $\delta$  direction into a value of  $x$  given by  $\gamma / \cos(\theta + \alpha - \pi/2)$ , this intensity distribution can also be easily converted to one of the form  $I_x(\theta, x, y)$ , as required for use in equation IV-5.

The detailed form of  $I_x'(\gamma, y)$  will ideally be the natural lineshape of the exciting x-ray(s), as converted from an energy to a coordinate scale by equation IV-8. However,  $I_x'(\gamma, y)$  will only be precisely equal to the natural lineshape if a completely uniform x-ray flux is emitted from a large enough surface area of the x-ray tube anode to span the full range of Bragg angles associated with the natural lineshape. For the specific system under study, the oblique angle of x-ray emission from the anode (approximately  $5^\circ$ , cf. Figure IV-1), translates this requirement into a rather broad area of uniform emission ( $\sim 2-3$  cm along the

direction of x-ray propagation). Any tapering off of x-ray flux over this area in moving away from the anode center will tend to narrow  $I_x'(\gamma, y)$  relative to the natural lineshape. Such effects have been allowed for in final numerical calculations based upon this model by directly measuring  $I_x'(\gamma, y)$  as described in Section IV-3.

The solid angle  $\Omega(\theta, x, y)$  will also in general be a complicated function derivable only by detailed trajectory calculations through the lens and analyzer for emission from all allowed surface points. However, to a good approximation, it can be simplified as a box function with constant value  $\Omega_0$  over all specimen surface points from which electrons can be imaged by the lens onto points inside the entrance aperture area  $A_0$ , and with zero value for all other surface points. If the lens is further assumed to be perfectly focusing with magnification  $-M$ , then the actual aperture dimensions  $\Delta r_0$  and  $y_0$  can be projected onto the surface along the direction of the reference trajectory to yield limits for the non-zero regions of  $\Omega(\theta, x, y)$  on the surface. Thus  $\Omega(\theta, x, y)$  in this approximation is defined to be:

$$\Omega(\theta, x, y) = \begin{cases} \Omega_0 & \text{for } -\Delta r_0/2M\sin\theta \leq x \leq \Delta r_0/2M\sin\theta \\ & -y_0/2M \leq y \leq y_0/2M \\ 0 & \text{for other values} \end{cases} \quad (\text{IV-9})$$

For the case under consideration, the lens is cylindrically symmetric, so that  $\Omega_0$  is a cone of solid angle with half-angle  $\Delta\theta/2$  (see Figure IV-3).

In order to compute the ideal apparent energy shift  $\Delta E'(\theta, x, y)$  it is also necessary to know the x-ray-associated energy shift relative to the reference trajectory for each point on the surface. Within our

approximations, this will be given by

$$\begin{aligned} E_{h\nu} &= \frac{d(h\nu)}{d\gamma} \cdot \gamma \\ &= \frac{d(h\nu)}{d\gamma} \cdot x \cos(\theta + \alpha - \pi/2) \end{aligned} \quad (\text{IV-10})$$

The electron-optical contribution to  $\Delta E'(\theta, x, y)$  can be calculated by assuming that only the radial position of the specimen image formed in the entrance aperture is significant in determining the apparent energy in the detection plane. This assumption thus neglects any effects due to differences in lens image positions along the direction of the reference trajectory, even though for an ideal lens, the specimen image will be oriented at some angle determined by  $\theta$ . This is reasonable, since the axial magnification of the lens will probably be of order unity, so that the maximum axial differences in image position will be small in comparison to the total trajectory length in the analyzer (approximately 0.1 cm in comparison to 49.0 cm). The radial image position is denoted by  $\Delta r$ , and if it is measured relative to the reference trajectory, it will be given by  $\Delta r = -Mx \sin\theta$ . This shift of  $\Delta r$  can be converted into an apparent energy shift by utilizing the known energy dispersion of the hemispherical analyzer, which implies that  $dE/dr = E_0/2r_0$ <sup>15,20</sup>. The dispersion is assumed constant for all trajectories, which will be the case as long as the total spread of photon energies is small in comparison to  $E_0$  ( $\sim 1\%$  for the specific system under study). The energy shift associated with the electron analyzer will then be given by

$$\begin{aligned}
 E_{e^-} &= (dE/dr) \cdot \Delta r \\
 &= -\frac{ME_0 \sin \theta}{2r} \cdot x
 \end{aligned}
 \tag{IV-11}$$

The total apparent energy shift associated with a given point on the specimen surface can now be calculated simply by adding the x-ray- and electron-optical contributions in equations IV-10 and IV-11 to give:

$$\Delta E'(\theta, x, y) = \Delta E_{h\nu} + \Delta E_{e^-}
 \tag{IV-12}$$

$$\Delta E'(\theta, x, y) = \left[ \frac{d(h\nu)}{d\gamma} \cos(\theta + \alpha - \pi/2) - \frac{ME_0 \sin \theta}{2r_0} x \right].$$

In order for dispersion compensation to occur,  $\Delta E'(\theta, x, y)$  must be zero for all points on the surface, implying that

$$\frac{\cos(\theta_0 + \alpha - \pi/2)}{\sin \theta_0} = \frac{ME_0}{2r_0 \cdot d(h\nu)/d\gamma}
 \tag{IV-13}$$

Equation IV-13 can be used to obtain  $\theta_0$  from a knowledge of the pertinent optical parameters. One of these parameters that is subject to relatively simple experimental alteration is the lens magnification  $M$ , and equation IV-13 indicates that a change in  $M$  will shift the location of  $\theta_0$ .

A further important point in connection with comparisons of experimental and theoretically-generated spectra at different angles  $\theta$  is that, if the specimen rotation axis does not intersect the reference trajectory (cf. Figure IV-3), then the point of intersection of this trajectory with the surface will shift along the  $x$  direction as  $\theta$  is varied. This shift will also cause a change in the photon energy incident at that point. If the rotation axis is offset from the

reference trajectory by a distance  $x_0$  along the surface with the specimen oriented at an angle  $\theta_0$ , then the associated energy scale shift for all points on the surface for arbitrary  $\theta$  is easily shown to be

$$\Delta E'_{h\nu} = \frac{d(h\nu)}{d\gamma} \cdot \frac{x_0 \sin\theta_0 \cos(\theta + \alpha - \pi/2)}{\sin\theta} \quad (\text{IV-14})$$

Theoretical spectra thus must be shifted by this amount in making comparisons with experiment. Significant instrumental peak shifts with  $\theta$  could, for example, be produced in this way by a misaligned specimen rotation axis.

A second type of spectrometer misalignment that can also produce energy shifts is associated with a vertical displacement  $\delta z$  of the specimen surface either above or below the specimen rotation axis, with the surface defined to contain the origin and the x and y axes as before. For  $\theta = \theta_0$ , such a displacement does not affect the attainment of dispersion compensation, but it does produce an energy shift given by

$$\Delta E''_{h\nu} = \frac{d(h\nu)}{d\gamma} \cdot \frac{\delta z \cos(\theta_0 + \alpha - \pi/2)}{\sin\theta_0} \quad (\text{IV-15})$$

Suitable sums of equations IV-14 and IV-15 can thus be used to determine the energy shifts appropriate for misalignments of both types at arbitrary angles.

Numerical calculations based upon this overall model were performed by first determining the ideal  $R'(\theta, \Delta E)$  from equation IV-5 and the stated approximations for  $I_x(\theta, x, y)$ ,  $\Omega(\theta, x, y)$  and  $\Delta E'(\theta, x, y)$ . This  $R'(\theta, \Delta E)$  was then convoluted with an experimental lineshape of minimum width corresponding to  $R''(\theta_0, \Delta E)$ . Energy scale shifts associated with

equation IV-14 were also included. The computer program written to carry out these calculations was further set up so as to permit inputs directly in terms of the two mechanical adjustments possible on the particular system under consideration. These were: (1) rotation of the monochromator crystals on an axis through their centers (cf. Figures IV-1 and IV-3), a procedure which has the net effect of translating the flux distribution  $I_x$  along  $\gamma$  (as denoted by "A" in Figure IV-3), and (2) rotation of the specimen-carrying rod about its axis (not equivalent to the specimen rotation axis), an action which moves the specimen rotation axis along a circular path of radius R, thereby changing its orientation with respect to the reference trajectory and the monochromator (denoted by "B" in Figure IV-3). The effects of spectrometer misalignment in either respect, and also the basic question of what constitutes optimum alignment could thus be directly investigated. Various numerical values utilized in these calculations are given in the next section, and the results of these calculations are compared with experiment in Section IV-4.

### 3. Experimental

All experimental spectra were obtained with a Hewlett-Packard 5950A photoelectron spectrometer that was specially modified to permit angular-dependent studies. The basic operation of this dispersion-compensating system has been discussed in prior sections.  $AlK_{\alpha_{1,2}}$  radiation is used for excitation. The acceptance solid angle  $\Omega_0$  of the cylindrically-symmetric electrons lens in this system was determined from detailed electron trajectory calculations to be a cone with  $3.5^\circ$  half angle in

the standard mode of electron lens operation (see equation IV-9 and Table IV-1).

A modified sample probe was constructed which allowed rotation of the specimen about two axes, one lying in the plane of the specimen surface and one normal to the surface. This probe was designed so as to be compatible with the standard differentially-pumped sliding-seal inlet system, and was constructed of non-magnetic ultrahigh vacuum materials. The probe as shown in figure IV-4 consists of a polished, notched, stainless-steel tube which contains the sample positioning device. This tube is closed at its internal end, and is fitted at its external end with a precision rotary- and linear-motion feedthru. The probe can thus translate a specimen from outside the vacuum chamber, through the sliding-seal inlet system, and into both an isolable sample preparation chamber and the x-ray photoelectron spectrometer.

The rotary motion of the manipulator is directly used to rotate the specimen about an axis lying in the plane of its surface, thereby effecting variation of  $\theta$ . The linear motion provided by the feedthru is used to rotate the specimen about an axis normal to its surface via a rack-and-pinion gear set, as shown in Figure IV-5; this rotation varies the azimuthal angle of electron emission. The  $\theta$  motion is controlled by a precision stepping motor ( $0.9^\circ$  per step) which is interfaced to a Hewlett-Packard 2100A computer; this computer is also used to control the spectrometer system. The linear motion for azimuthal angle adjustment is produced by a micrometer.

The sample rotation mechanism consists of a fixed frame, a rotating

yoke and a sample holder as shown in Figure IV-5. The frame, which is rigidly mounted to the probe tube, defines the  $\theta$  axis of rotation and also contains a notched rod and return spring that transmit linear motion to the azimuthal-drive rack-and-pinion set. The yoke carries the sample holder and the azimuthal-drive mechanism and is turned in the frame by the rotary motion of the feedthru. The sample holder is mounted in the yoke in such a way that the plane of the sample surface is accurately positioned to contain the  $\theta$  axis of rotation defined by the frame. The pin on the azimuthal-drive rack gear engages the notch of the linear drive rod for a particular setting of  $\theta$ . At this setting of  $\theta$ , the azimuthal angle may be changed. After the azimuthal angle has been changed,  $\theta$  rotation is again possible. Figures IV-5(a)-(c) show closeup views of this mechanism at three different  $\theta$  settings. Although azimuthal rotation of the specimen was not critical for any of the data reported here, it has proven to be useful in studies of either single-crystal specimens<sup>12,14</sup> or specimens with anisotropic surface roughness contours<sup>8,9,11,12</sup>. Both azimuthal- and polar-angles can be set to within  $\pm 1^\circ$  with this device.

A precision rotary feedthru was also mounted on the monochromator chamber so as to permit in situ rotation of the mounting block containing the three quartz crystals, as shown in Figures IV-1 and IV-3. The resultant movement of the x-ray flux with rotation of the internal monochromator adjusting screw was experimentally measured by observing the darkened image of the flux formed on a specimen of white polyvinylchloride. The measured flux movement perpendicular to the x-ray

propagation direction was  $1.09 \times 10^{-3}$  cm per degree of adjusting screw rotation. This experimental result compares very well with a value of  $1.17 \times 10^{-3}$  cm deg<sup>-1</sup> calculated from the known geometry of the crystal mounting assembly.

The ability to adjust the position of the x-ray flux ("A" in Figure IV-3) combined with the ability to rotate the probe tube in the seals about the longitudinal axis of the tube ("B" in Figure IV-3) provides the necessary degrees of freedom for aligning the sample holder in the spectrometer. For a certain combination of these adjustments, it is possible to make the x-ray flux maximum and the specimen rotation axis both lie at some point along the axis of the electron lens (central reference trajectory). In this condition, the spectrometer is optimally aligned and rotation of the sample about the axis lying in its surface causes variations in resolution relative to the dispersion-compensated case, but results in no net shifts in the observed photoelectron peaks. However, if the alignment conditions outlined above are not met, either because the axis of rotation does not lie in the sample surface or because the axis of rotation does not coincide with the intersection of the reference trajectory and the maximum in the x-ray flux distribution, then purely instrumental peak shifts and asymmetries will be introduced into the observed spectra with rotation of the sample. Such effects were observed experimentally, and examples of the shifts caused by monochromator misalignment are shown together with the theoretically predicted shifts in Figure IV-6. Such shifts and asymmetries result primarily from the movement of the centroid of the spatially energy-

dispersed x-ray flux across the sample surface with rotation of the sample and are discussed in more detail in Section IV-4. The absence of peak shifts and asymmetries with rotation of the sample provides a very sensitive test for overall spectrometer alignment.

In addition to providing a means of alignment, the ability to rotate the probe in the seals also permitted measuring the spatial distribution of the x-ray flux perpendicular to the x-ray propagation direction,  $I(\gamma, y)$ . The sample was rotated on its axis so as to be nearly parallel to the x-ray propagation direction ( $\phi_x \approx 5^\circ$ ) but still exposed to both the x-ray flux and the electron lens. The sample surface which lay within the acceptance of the electron optics was thus excited by only a small section of the dispersed x-ray flux. The probe was then rotated on its axis together with simultaneous counter-rotation of the specimen so as to maintain a constant  $\phi_x$ . In this way the specimen was effectively translated across the x-ray flux, and the total peak intensity measured at each position was proportional to the flux strength in a narrow interval in  $\gamma$ . The results of such a probe-rotation experiment with a gold sample are shown in Figure IV-7 along with the expected  $\text{AlK}\alpha_{1,2}$  lineshape<sup>15</sup>. The energy scale of the figure is derived from the dispersion of the quartz crystal ( $d(h\nu)/d\gamma = 11.03 \text{ eV/cm}$  at the sample) and the known geometry of the monochromator and the sample probe. It is apparent that the full  $\text{AlK}\alpha$  line is not transmitted by the monochromator. As noted previously, this can be explained by the geometry of the x-ray anode, which has a relatively small excitation spot and is placed at a shallow angle of  $\sim 5^\circ$  relative to the x-ray

emission direction toward the monochromator crystals (see Figure IV-1). This anode geometry results in an effective slitting of the x-ray source, since those regions of the anode which are located so as to have Bragg angles appropriate for energies near the edge of the  $AlK_{\alpha}$  line are not as strongly excited by the electron flux from the cathode. The overall flux distribution  $I_x(\gamma, y)$  is further found to be very well approximated by a single Gaussian peak with a FWHM of 0.64 eV; it is this form that was used in theoretical calculations of spectrometer performance.

A further modification was made in the operation of the spectrometer for some experiments. Namely, the magnification of the four-element electron lens was reduced from -5.0 to -2.3. The advantage associated with this change can be understood by noting that, in the limit of  $\theta \approx 0^\circ$ , the resolution of the spectrometer is limited primarily by the width of the excitation line, and that at  $\phi_x \approx 0^\circ$ , it is limited primarily by the width of the entrance slit to the hemispherical analyzer and the dispersion of the analyzer (cf. Section IV-1 and Figure IV-2). For this system, the excitation width is  $\sim 0.6$  eV, the entrance aperture to the hemispheres has a width  $r_0 \approx 0.6$  cm, and the dispersion of the hemispherical analyzer is  $dE/dr = 3.71$  eV/cm. Thus, in the limit of low  $\theta$ , the instrumental contribution to linewidth is  $\approx 0.6$  eV, and in the limit of low  $\phi_x$  (high  $\theta$ ), it is 2.2 eV. Although the instrumental widths at these two limits are thus fixed properties of the instrument, it was desirable to attempt to improve the resolution for high  $\theta$  values near the low- $\phi_x$  limit, which occurs for  $\theta \approx 108^\circ$  as  $\alpha = 72^\circ$  for this system. Reference to equation IV-13 shows that, if the magnification of the lens is decreased, then the dispersion-compensation condition is met for a

higher value of  $\theta_0$ . By modifying only the voltage on the third lens element, it was found to be possible to decrease the lens magnification from -5.0 to -2.3, and thus to change  $\theta_0$  from  $30^\circ$  to  $60^\circ$ . A preliminary discussion of the use of this mode has been presented previously<sup>21</sup>.

(Lens magnifications were determined directly from experimental image size along the y coordinate in the multichannel detector, from equation IV-13 and experimental minimum line width angles, and also from theoretical electron trajectory calculations. All three methods gave the same result to within  $\pm 10\%$ .)

In normal operation of the lens, the potentials of the first and second lens elements ( $V_1$  and  $V_2$ ) are fixed at ground and + 1250 V, respectively. The potential of the fourth lens element ( $V_4$ ) which provides the final retarding potential is given by

$$\begin{aligned} V_4 &= -(h\nu - E_b) + E_0 \\ &= -(1486.6 - E_b) + 115.0 \text{ (volts),} \end{aligned} \quad (\text{IV-16})$$

in which  $h\nu$  is the mean  $\text{AlK}\alpha$  photon energy,  $E_b$  is the electron binding energy referenced to the spectrometer vacuum level and  $E_0$  is the mean energy of analysis. The potential of the third lens element ( $V_3$ ) is linearly dependent on  $V_4$  and is given by

$$V_3 = (V_4 + 90.0) \times .897 \text{ (volts).} \quad (\text{IV-17})$$

It was found empirically that the magnification of the electrostatic lens could be reduced with no significant loss in resolution by holding  $V_1$ ,  $V_2$  and  $V_4$  at their normal values and modifying  $V_3$  to

$$V_3 = (V_4 + 1076) \times .987 \text{ (volts).} \quad (\text{IV-18})$$

The empirical values for the slope and intercept in this equation were obtained by observing the Cu  $2p_{3/2}$  ( $E_b = 931$  eV), Cls ( $E_b = 284$  eV), Au $4f_{7/2}$  ( $E_b = 284$  eV), and Au5d ( $E_b = 0-10$  eV) lines and varying  $V_3$  to optimize resolution at the lower magnification. The effects of this magnification change on resolution at various angles is discussed in detail in the next section. The solid angle in this mode of operation was determined from trajectory calculations to be a cone of  $2.8^\circ$  half-angle.

A summary of the various parameters characterizing this spectrometer is given in Table IV-1.

In accumulating all spectra, care was taken to avoid any effects due to signal saturation in the videcon tube forming part of the multichannel detector system. Such effects were more pronounced for the higher intensities encountered with higher  $\theta$  values and also for operation with the lower lens magnification, which led to smaller dimensions of the source image on the detector as measured along the y direction.

Two types of samples were used in this study. Gold specimens were prepared by in situ evaporation of high purity gold onto glass substrates, with provision being made for electrical contact between the sample and the spectrometer to avoid charging effects. Carbon samples were prepared by allowing an Aquadag colloidal graphite suspension to evaporate on a gold-plated copper substrate to form a smooth, contiguous, thick carbon layer. The carbon samples were heated in air to drive off any remaining volatile impurities before being inserted into the spectrometer. The pressures during measurements were  $\sim 2-5 \times 10^{-9}$  torr. Residual small-

scale surface roughness on either type of specimen has been shown theoretically not to affect its use in the determination of a flat-surface instrument response function<sup>12</sup>.

#### 4. Results and Discussion

Detailed theoretical calculations of  $R'(\theta, \Delta E)$  were carried out for ideal operation of a spectrometer of the Hewlett-Packard geometry by means of equation IV-5. These calculations were performed for lens magnifications of both -5.0 and -2.3 at a variety of possible spectrometer alignments using the parameters given in Section IV-3 and Table IV-1. The  $R'(\theta, \Delta E)$  functions were then convoluted with minimum linewidth Cls spectra obtained at each lens magnification. The results of this convolution are  $N_{\infty}'(\Delta E, \theta)$  as defined in equation IV-6 and can be compared directly to experimental spectra obtained at the angle  $\theta$ . For a magnification equal to -5.0, the minimum linewidth was observed at  $\theta = 30^{\circ}$  and  $\theta_0$  was taken to be  $30^{\circ}$ . At a lens magnification of -2.3, the minimum linewidth occurred at  $\theta = 60^{\circ}$  and this angle was taken as  $\theta_0$ . In each case the experimental  $\theta_0$ 's are within 10% of the values calculated from equation IV-13. Theoretical and experimental spectra are compared for lens magnifications of -5.0 and -2.3 in Figures IV-8 and IV-9 respectively, for the case of an optimally aligned spectrometer. The theoretical spectra are in excellent agreement with experiment and reproduce both the observed intensity variations and the increases in linewidth as  $\theta$  is varied away from  $\theta_0$ . Two minor discrepancies are easily explained: In both figures at high  $\theta$  where  $R'(\theta, \Delta E)$  becomes quite broad ( $\sim 2.2$  eV) there is a slight peak shift relative to

experiment. This apparent peak shift probably occurs because the inelastic tail in the Cls spectrum at  $\theta = \theta_0$  that was used in determining  $R'(\theta_0, \Delta E)$  was not precisely equivalent in origin to the tails at other angles. The convolution of this tail in calculating the spectra at any other angle  $\theta$  thus gives rise to a slight shift and asymmetry that would not be present if all spectra were somehow corrected for inelastic scattering. The slight deviations in peak intensity between theory and experiment could be caused by either small errors due to bulk inelastic scattering effects or by a small amount of oxygen impurity near the graphite sample surface. The presence of such an impurity layer could decrease the Cls intensity at low  $\theta$  relative to the intensity at higher  $\theta$  because of inelastic scattering. This would result in a decrease in the experimental Cls intensity relative to theory for  $\theta < \theta_0$  and an increase relative to theory for  $\theta > \theta_0$ , as is observed; this effect was much more pronounced in a similar comparison of theory and experiment carried out for the Au4f intensity from an evaporated gold film with a carbon contaminant overlayer.

The variation in peak area with  $\theta$  is equivalent to the energy integrated response function  $R(\theta)$  and is shown in Figure IV-10 for the lens magnifications of -5.0 and -2.3. Except for the slight systematic deviations between theory and experiment noted above, there is in general excellent agreement. It is apparent that for this spectrometer geometry, the intensity increases greatly as  $\theta$  increases. This variation of intensity with angle results from a combination of the wide acceptance aperture utilized in the dispersion-compensated spectrometer and the

non-uniformity of the x-ray flux distribution  $I_x'(\gamma, y)$  along  $\gamma$ . It has been shown previously<sup>3,5</sup> that, for the simple case of a uniform flux distribution and a box-type solid angle distribution such as equation IV-9, the signal intensity from a thick specimen will be constant with variation in  $\theta$  so long as the illuminated portion of the sample fills the projected entrance aperture of the analyzer. For this case, when the illuminated portion of the sample no longer fills the projected acceptance of the analyzer (below some angle designated  $\theta_{\min}$ ) the intensity will fall off as  $\sin\theta$  with decreasing angle. Due to the wide acceptance of the dispersion-compensated spectrometer, effects analogous to those associated with  $\theta_{\min}$  occur at large values of  $\theta$ . For example, for the lens magnification equal to  $-5.0$ , 95% (or  $+2\sigma$ ) of the Gaussian flux distribution on the sample fills the projected entrance aperture for  $\theta \approx 60^\circ$  while for a magnification of  $-2.3$ , the same condition is met for  $\theta \approx 89^\circ$ . The response functions  $R(\theta)$  for these magnifications are the same for  $\theta \lesssim 60^\circ$  since essentially the full flux distribution is accepted at either magnification. The intensity does not become constant with increasing  $\theta$  for  $\theta > \theta_{\min}$  because the concurrent decrease in  $\phi_x$  ( $\phi_x = \pi - \alpha - \theta = 108^\circ - \theta$ ) results in the illumination of the portion of the sample that lies within the projected acceptance of the analyzer by the more intense central region of the x-ray flux distribution. The volume elements near the surface that are responsible for producing no-loss photoelectrons are thus illuminated by a higher average x-ray flux. The  $R(\theta)$  for a magnification of  $-2.3$  is greater than that for  $-5.0$  for  $\theta > 60^\circ$  because a larger specimen surface area is included in the

projected analyzer acceptance (cf. equation IV-9). In addition to increased x-ray flux at the surface, placement of the sample so as to receive the monochromatized radiation at low  $\phi_x$  also results in a further effective slitting of the monochromator output and a resultant flux that is more monoenergetic on those regions of the sample within the acceptance of the analyzer. This increase in photon intensity and monochromaticity at low  $\phi_x$  could perhaps be exploited in the design of a spectrometer utilizing a monochromatized x-ray source, for example, in conjunction with an analyzer such as a cylindrical mirror in which dispersion compensation is not possible.

In Figure IV-11 the variation of the FWHM of the Cls peak with  $\theta$  is shown. Again excellent agreement between theory and experiment is obtained for both lens magnifications. As was noted in Section IV-2, the resolution is independent of lens magnification for the extremes of  $\theta \approx 0^\circ$  and  $\phi_x \approx 0^\circ$  ( $\theta \approx 108^\circ$ ). This point is verified by the convergence of the two experimental and theoretical FWHM curves at  $\theta = 0^\circ$  and  $\theta = 108^\circ$ . The observed and calculated width of 1.1 eV at  $\theta = 0^\circ$  is consistent with an excitation width of  $\sim .64$  eV and the observed and calculated width of  $\sim 2.6$  eV at  $\theta \approx 108^\circ$  is consistent with an analyzer entrance aperture of .6 cm. In the range of  $\theta$ 's between the extremes, it can be seen that dispersion compensation quickly breaks down as  $\theta$  becomes greater than  $\theta_0$  for a lens magnification of -5.0. However, for the lens magnification of -2.3 the resolution is less strongly dependent on  $\theta$  over the full range and very good resolution with FWHM  $\approx 1.1$  eV can be maintained from  $\theta = 0^\circ$  to  $\theta \approx 85^\circ$ . In comparison with Figure IV-10

it can also be noted that, when the spectrometer is operated at the lower lens magnification (with resulting change in  $\theta_0$  from  $30^\circ$  to  $60^\circ$ ), it is possible to gain approximately a factor of two in sensitivity with very little loss in resolution. It is also evident that the considerable loss of resolution occurring for  $\theta > 95^\circ$  could be avoided if the radial width of the entrance aperture to the hemispherical analyzer were externally adjustable, rather than fixed in magnitude. This variation in resolution with sample angle is specific to the dispersion-compensating spectrometer geometry discussed here. A more conventional hemispherical analyzer with or without a monochromatized source would to first order show no variation in resolution with changing sample angle.

The effects of various possible types of spectrometer misalignment were also studied (cf. Section IV-3). These calculations were again in good agreement with experimental results obtained for intentional misalignment of the spectrometer. For example, Figure IV-6 presents results for which the axis of sample rotation was kept in the sample surface and intersecting the centerline of the electron optics. However, the centroid of the x-ray flux distribution was allowed to move so as to lie either above or below the axis of  $\theta$  rotation. Both theory and experiment show that considerable peak shifts can be introduced with  $\theta$  rotation when the center of the x-ray flux is not coincident with the axis of rotation. The shapes of the peak shift curves can be qualitatively understood in the following manner. The cause of the apparent peak shift is the movement of the intense center of the x-ray flux distribution across the sample with variation in  $\theta$  which in turn results in a radial movement

of the sample image in the entrance plane of the analyzer. At  $\theta = 0^\circ$ , the displacement of the flux along the sample surface has no effect since the surface then lies on the centerline of the electron optics and movement of the x-ray flux does not cause any radial movement of the sample image in the entrance plane of the hemispherical analyzer. Hence, all curves converge for  $\theta = 0^\circ$ . As  $\theta$  is increased from  $0^\circ$  the center of the x-ray flux will tend to move across the sample and away from the central reference trajectory. Thus, if the center of the flux is above the sample axis of rotation, the most intense part of the projected image of the sample in the entrance plane of the analyzer will tend to move radially outward with increasing  $\theta$  due to the inversion of the sample image by the lens. This will move the image in the detection plane radially inward giving an apparent shift to higher binding energy (lower kinetic energy). Similarly, if the center of the flux is below the axis of rotation the projected image will shift inward to lower radius and there will be an apparent shift to lower binding energy. In either case, the effect will tend to saturate at high  $\theta$  as the center of the flux moves out of the acceptance of the analyzer. Such peak shifts with angle could also occur for similar reasons in a monochromator-based system without dispersion compensation; the principle requirement is for a collimated radiation source to exist.

In addition to causing peak shifts and asymmetries, misalignment of the spectrometer can also affect the integrated response function  $R(\theta)$ . In the previous example of misalignment it was noted that the x-ray flux tended to move outside of the acceptance of the analyzer for large values

of  $\theta$ . This movement results in a decrease in intensity at higher  $\theta$ 's relative to the optimally aligned case. Figure IV-12 shows the theoretical and experimental variations in intensity for the cases of x-ray flux misalignment described previously in connection with Figure IV-6. It can be seen that the fall off in intensity with increasing  $\theta$  increases dramatically with the degree of monochromator misalignment. Similar instrumentally-produced intensity changes with angle would also occur in any system with a collimated radiation source that is misaligned so as not to be directed at a rotation axis lying in the specimen surface.

While the preceding discussion makes it clear that an understanding of the system response function is necessary for absolute intensity studies and for analysis of peak shapes and peak shifts, it is also important to note that the integrated response function  $R(\theta)$  is a function only of  $\theta$  for a particular spectrometer in a given state of alignment. Therefore, meaningful relative intensity measurements can be made in any spectrometer with no knowledge of  $R(\theta)$  so long as ratios are taken between different peak areas at a given angle. This point is well illustrated in Figure IV-13 where the ratios of Cls to Au $4f_{7/2}$  peak areas are shown as a function of  $\theta$  for a variety of spectrometer alignments for an evaporated gold sample with a thin carbon overlayer. Even though  $R(\theta)$  is significantly different for the various alignments (as indicated in Figure IV-12, the ratio data is in very good internal agreement.

## 5. Conclusions

The theoretical model presented has been shown to very well describe

the operation of a photoelectron spectrometer with a monochromatized x-ray source. In particular, the model predicts the instrumental contributions to peak shape, position, and intensity in angle-resolved photoemission experiments for a spectrometer system which allows dispersion compensation for the x-ray excitation width. While the response of the this system has been discussed previously for the particular sample placement at which dispersion compensation occurs, this is the first treatment which allows for arbitrary placement and also accounts for various effects associated with spectrometer misalignment. The numerical results presented should be applicable to any spectrometer of the same design and the alternate lower lens magnification should significantly extend the usefulness of this type fo spectrometer in performing measurements over a wide range of angles. Furthermore, the model presented is general enough that, with the use of proper excitation and acceptance functions, it should be applicable to predicting instrumental effects in AD experiments with other spectrometer systems. A further useful quantity which can be derived from this model is the total intensity response function  $R(\theta)$ ; this function is required for absolute intensity measurements as a function of angle. However, it has also been demonstrated that  $R(\theta)$  influences only absolute intensity measurements and that, if ratios of peak areas are taken at a given spectrometer setting, then the response function cancels. This result is of utility for the performance of AD studies in any spectrometer for which  $R(\theta)$  is not known.

REFERENCES  
SECTION IV.

1. C. S. Fadley and S. Å. L. Bergstrom, Phys Letters 35A 375 (1971).
2. C. S. Fadley and S. Å. L. Bergstrom, in Electron Spectroscopy, D. A. Shirley, Ed., North Holland, Amsterdam, 1972, p. 233.
3. B. L. Henke, Phys. Rev. A 6, 94 (1972).
4. W. A. Fraser, J. V. Florio, W. N. Delgass, and W. D. Robertson, Surf. Sci. 36, 661 (1972).
5. C. S. Fadley, R. J. Baird, W. Siekhaus, T. Novakov, and S. Å. L. Bergstrom, J. Electron Spectrosc. 4, 93 (1974).
6. C. S. Fadley, J. Electron Spectrosoc. 5, 725 (1974).
7. J. Brunner and H. Zogg, J. Electron Spectrosc. 5, 911 (1974) and private communication.
8. R. J. Baird, C. S. Fadley, S. Kawamoto, and M. Mehta, Chem. Phys. Letters 34, 49 (1975).
9. C. S. Fadley, paper and comments in Faraday Society Discussion No. 60 (1975).
10. M. Mehta and C. S. Fadley, Physics Letters 55A, 59 (1975).
11. R. J. Baird, C. S. Fadley, S. Kawamoto, M. Mehta, R. Alvarez, and J. Silva, Anal. Chem. 48, 843 (1976).
12. C. S. Fadley, to appear in Progress in Solid State Chemistry, G. Samorjai and J. McCaldin, Eds., Pergamon Press, 1976, Volume 11, Part 3.
13. K. Siegbahn, U. Gelius, H. Siegbahn, and E. Olson, Physics Letters, 32A, 221 (1970).

14. R. J. Baird, C. S. Fadley, and L. F. Wagner, to be published.
15. K. Siegbahn et al., Electron Spectroscopy for Chemical Analysis, Nova Acta Regiae Soc. Sci. Upsaliensis, Almqvist and Wiksells, Uppsala, Sweden, 1967, or National Technical Information Service Report No. AD844315, U. S. Department of Commerce.
16. K. Siegbahn, J. Elect. Spectrosc. 5, 3 (1974).
17. D. E. Eastman in Vacuum Ultraviolet Physics, E. E. Koch, R. Haensel, and C. Kunz, Eds., Pergamon Press, New York, 1974.
18. S. Doniach, I. Lindau, W. E. Spicer and H. Winick, J. Vac. Sci. Technol. 12, 1123 (1975).
19. K. Siegbahn, D. Hammond, H. Fellner-Feldegg, E. F. Barnett, Science, 176, No. 7032, 245 (1972).
20. K. D. Sevier, Low Energy Electron Spectroscopy, Wiley Interscience, New York, 1972.
21. R. J. Baird and C. S. Fadley, paper presented at the Northwest Regional ACS Meeting, June 1975, Honolulu, Hawaii.

Table IV-1 - Values of various physical parameters defining the spectrometer system under investigation (Hewlett-Packard 5950A).

Crystal monochromator:

Bragg angle =  $\theta_B = 78.5^\circ$   
 Rowland circle diameter = 27.94 cm (11.0 in)  
 Dispersion -  $d(h\nu)/d\gamma = 11.03$  eV/cm  
 Flux distribution -  $I_x'(\gamma, y)$  Gaussian of 0.64 eV FWHM along

Electrostatic lens:

Manification =  $M = -5.0$  or  $-2.3$  (two modes)  
 Acceptance solid angle =  $\Omega_o = \begin{cases} \text{cone of } 3.5 \text{ half-angle (M = -5.0)} \\ \text{cone of } 2.8 \text{ half-angle (M = -2.3)} \end{cases}$   
 Angle between x-ray incidence and lens axis =  $\alpha = 72^\circ$

Hemispherical analyzer:

Radius of central trajectory =  $r_o = 31.12$  cm (12.25 in)  
 Energy of analysis =  $E_o = 115$  eV  
 Dispersion =  $dE/dr = e.71$  eV/cm  
 Entrance aperture width =  $\Delta r_o = 0.30$  cm  
 Entrance aperture height =  $y_o = 2.5$  cm

Specimen probe:

Radius of rotation of specimen axis =  $R = 0.714$  cm (0.281 in)  
 Horizontal offset of specimen rod rotation axis from lens axis  
 (cf. Figure 3) =  $0.559$  cm (0.220 in)

Figure IV-1 - Schematic illustration of the combined x-ray- and electron-optical system showing the relationship between the crystal monochromator, specimen, imaging electrostatic lens and hemispherical analyzer.

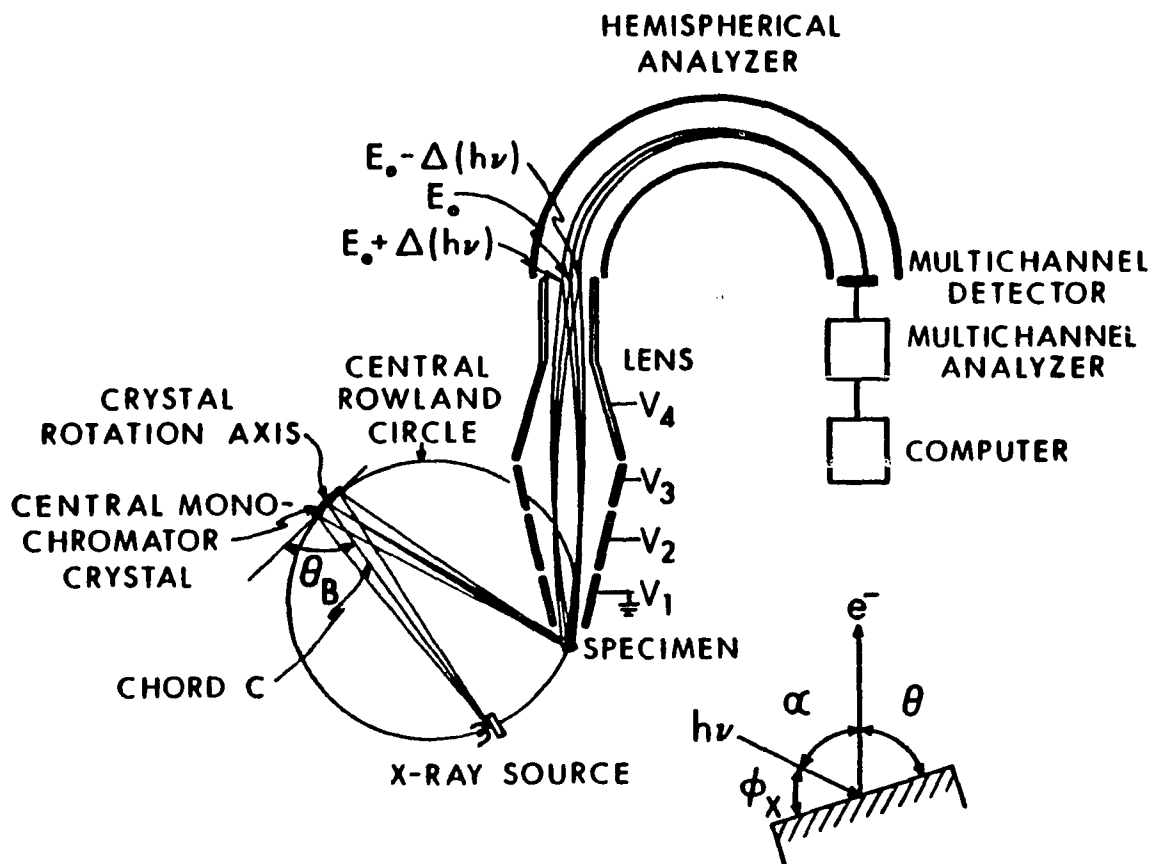
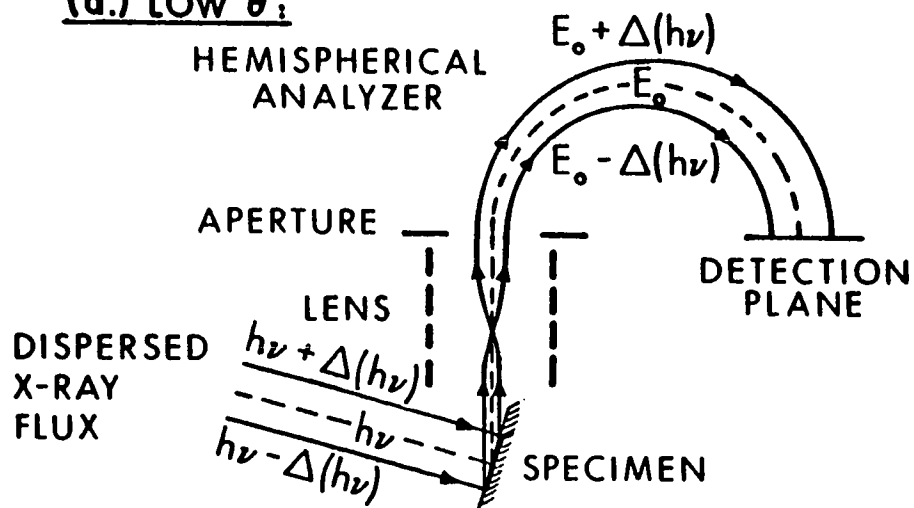


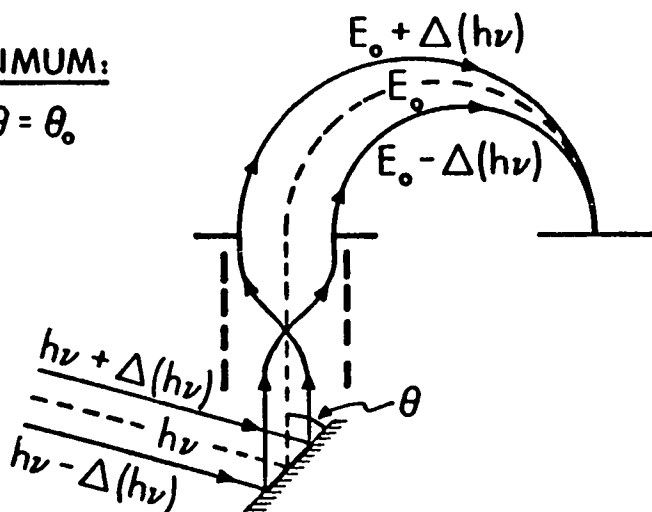
Figure IV-2 - Schematic diagram of electron trajectories for various sample positions: (a) for low  $\theta$ , the projected image of the sample appears as a narrow source in the entrance plane of the analyzer; (b) for  $\theta = \theta_0$ , dispersion compensation is achieved; (c) for low  $\phi_x$  (high  $\theta$ ), the active portion of the sample is illuminated by photons in a narrow range of energies  $\delta(h\nu)$ .

(a.) LOW  $\theta$ :



(b.) OPTIMUM:

$\theta = \theta_0$



(c.) HIGH  $\theta$  (LOW  $\phi_x$ ):

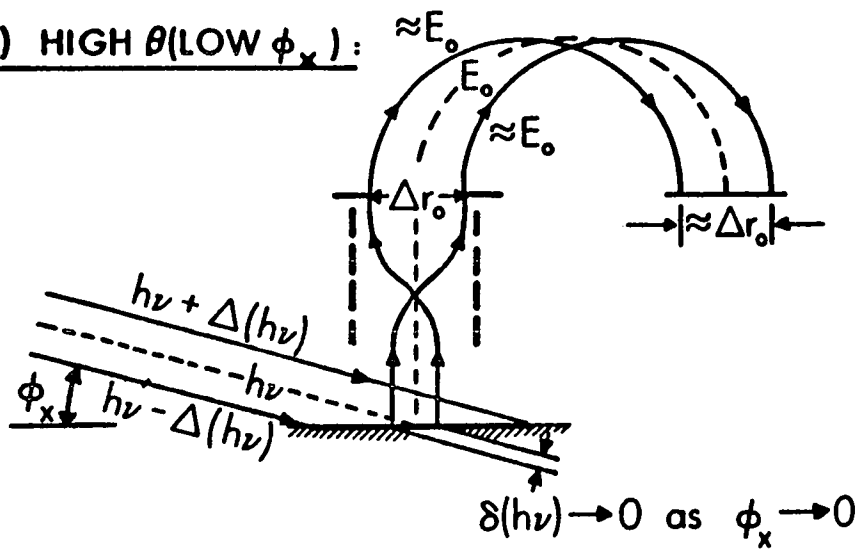


Figure IV-3 - A general spectrometer geometry indicating various quantities necessary for the mathematical modeling of spectrometer operation. The various items noted are defined more precisely in the text.

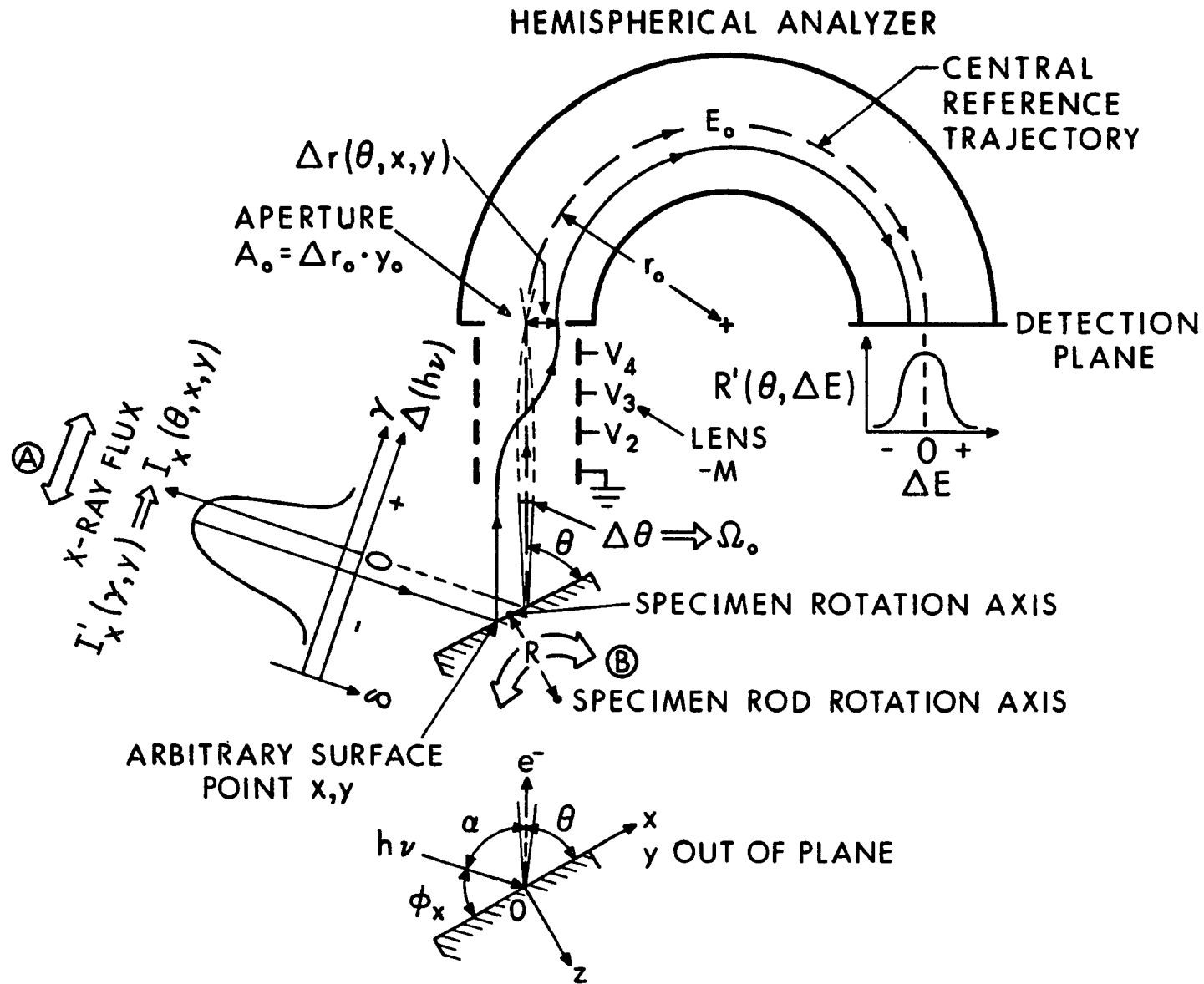


Figure IV-4 - (a) Overall view of the modified sample probe which permits automated two-axis rotation of the specimen. The long polished tube is compatible with the differentially-pumped sliding inlet seals of a Hewlett-Packard 5950A spectrometer. The specimen is shown in white. (b) External drive for the modified probe. A precision stepping motor provides  $\theta$  rotation by means of a graduated rotary feedthru. A micrometer permits precise linear motion for  $\phi$  rotation.

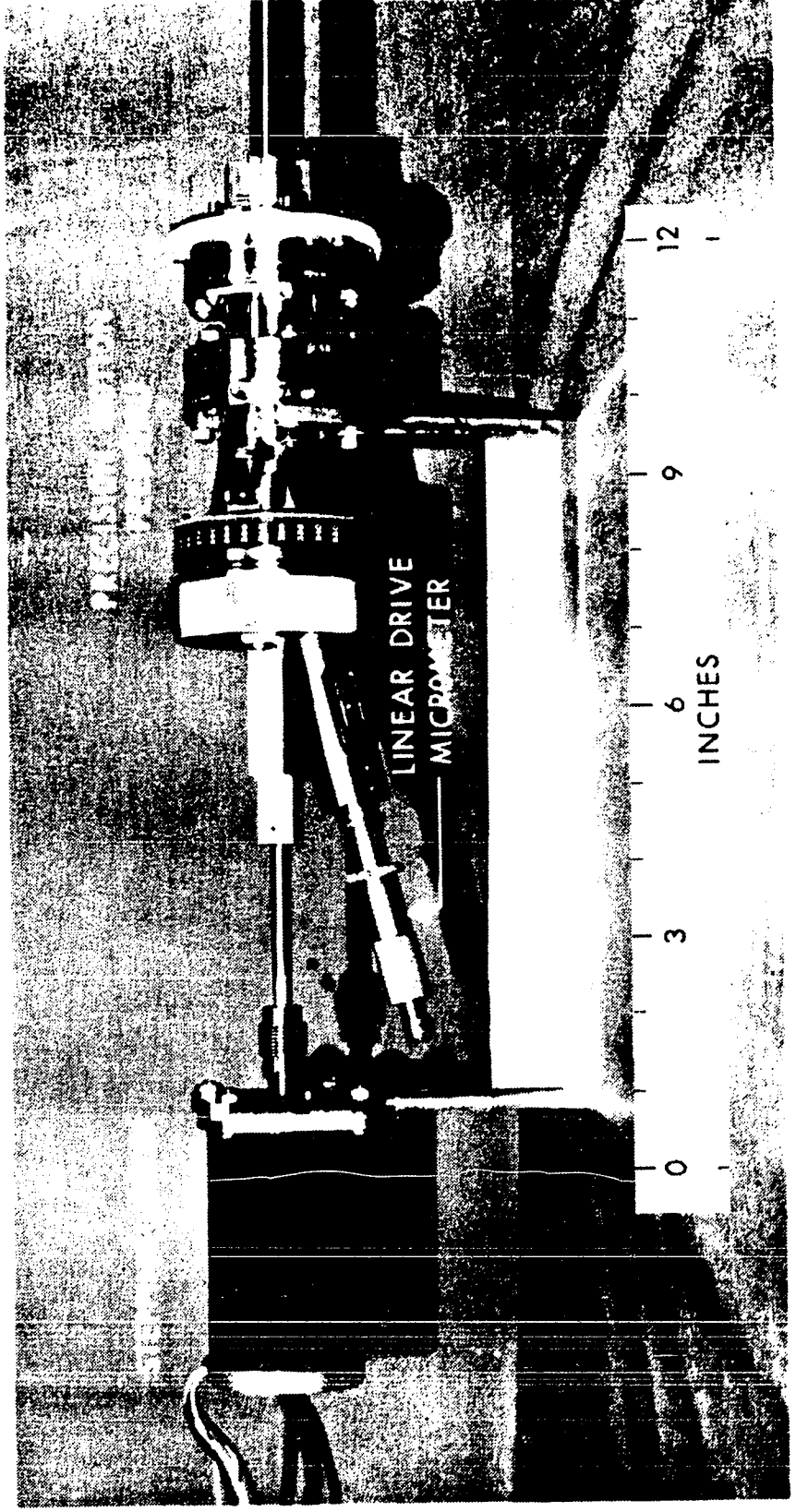
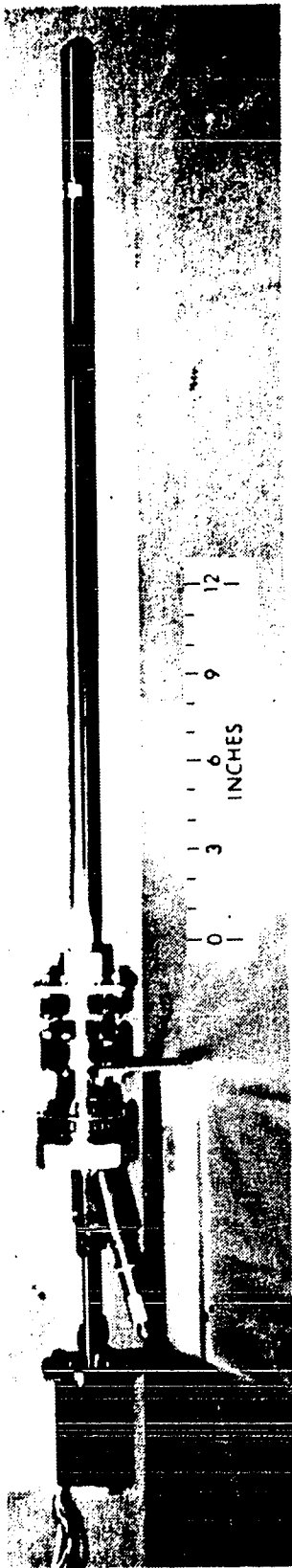
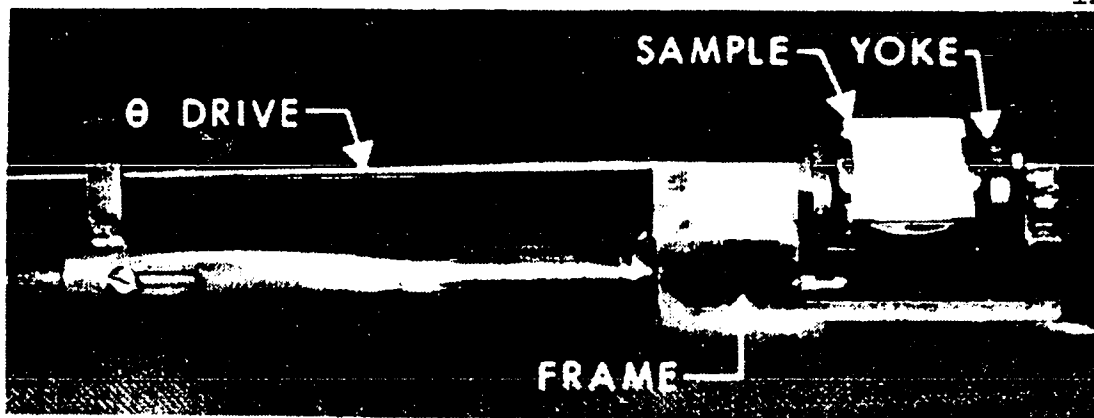
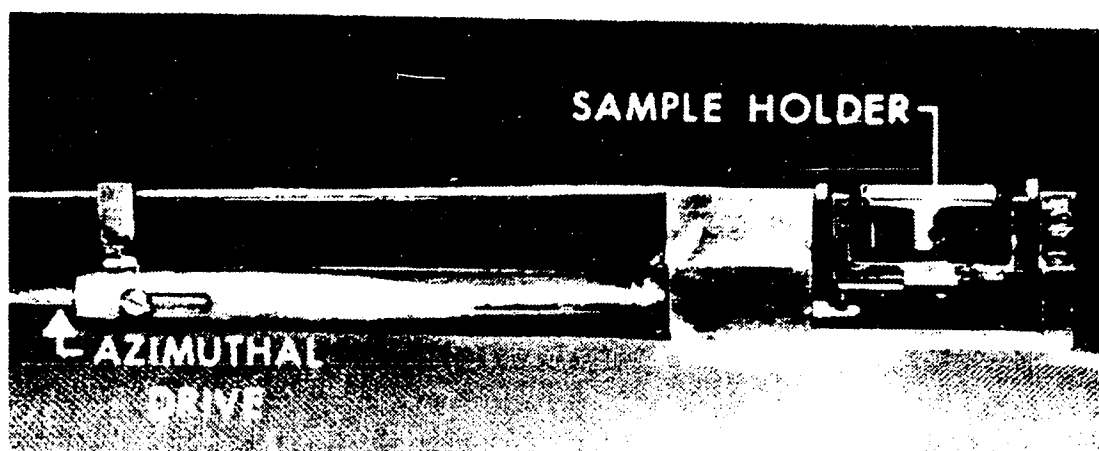


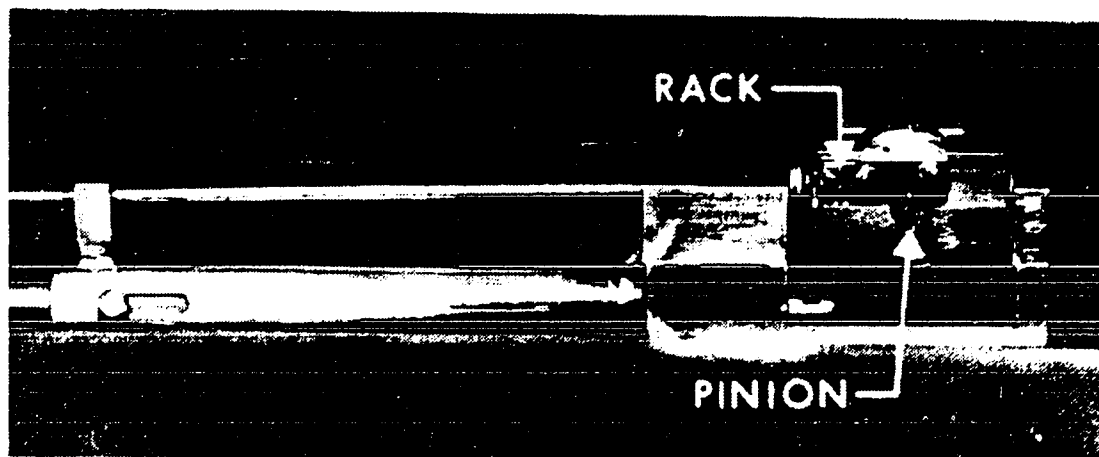
Figure IV-5 - Three views of the sample rotation mechanism which is mounted inside the polished tube of Figure 4. The specimen (in white) is shown at three different  $\theta$  orientations.  $\theta$  variation is provided by rotation of the small-diameter upper shaft. Azimuthal rotation is effected via linear motion of the lower shaft of larger diameter at left, which is in turn converted into rotational motion by means of a rack-and-pinion gear set. In (b), a notch in the  $\phi$ -rotation drive shaft is shown engaged with a pin on the rack gear so as to provide azimuthal motion.



a



b



c

Figure IV-6 - Purely instrumental peak shifts with variation of  $\theta$  introduced by monochromator misalignment. Alignments are indicated in degrees of motion of the standard adjusting screw relative to the optimum setting, with positive values corresponding to motion of the center of the x-ray flux distribution above the specimen axis of rotation.  $60^\circ$  of rotation translates the flux distribution by approximately one FWHM or 0.066 cm along  $\gamma$ .

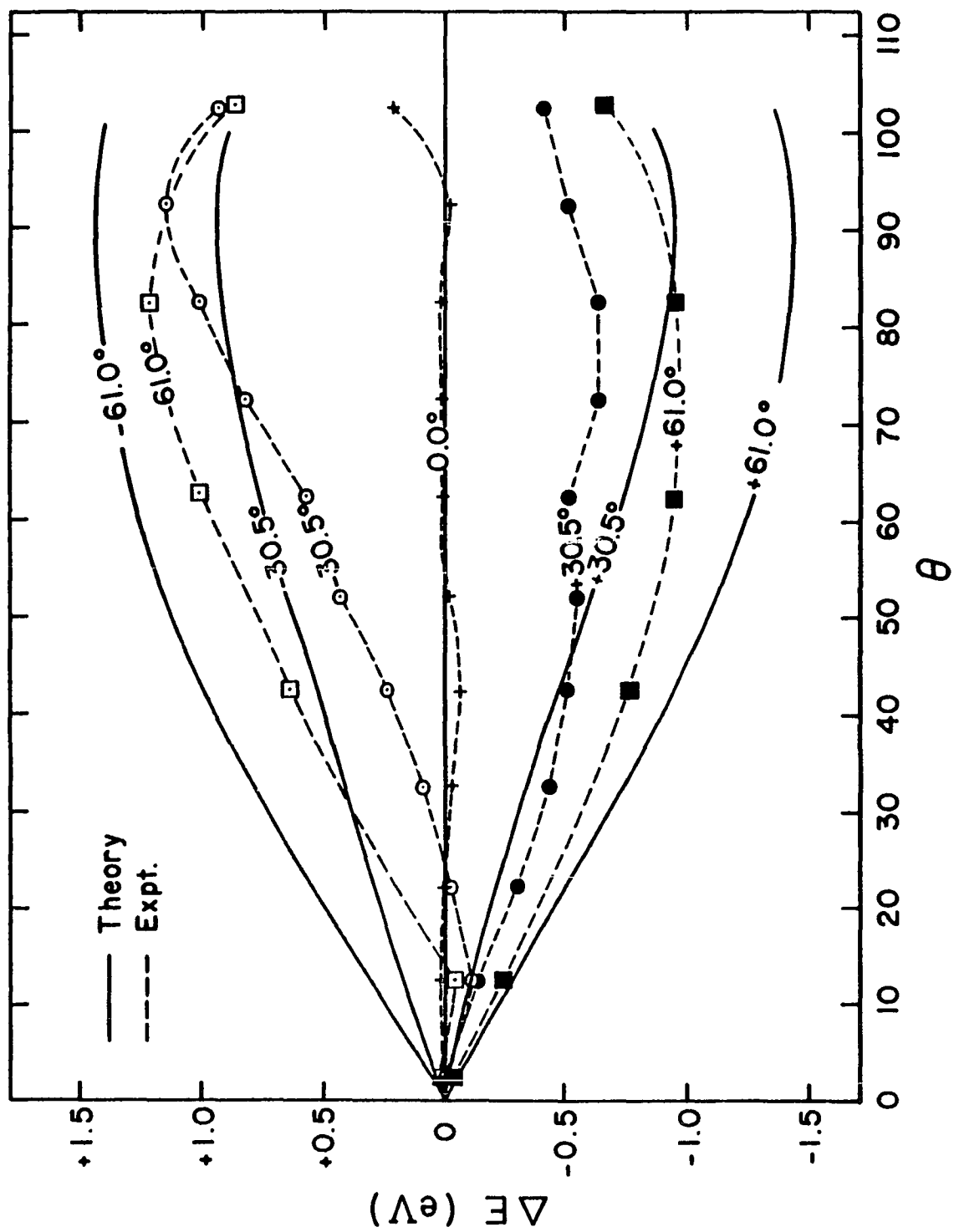


Figure IV-7 - The experimental x-ray flux distribution perpendicular to the mean x-ray propagation direction is compared to the full AlK $\alpha$  <sub>1,2</sub> distribution from reference 15. The experimental lineshape was measured by the probe-rotation experiment described in the text.

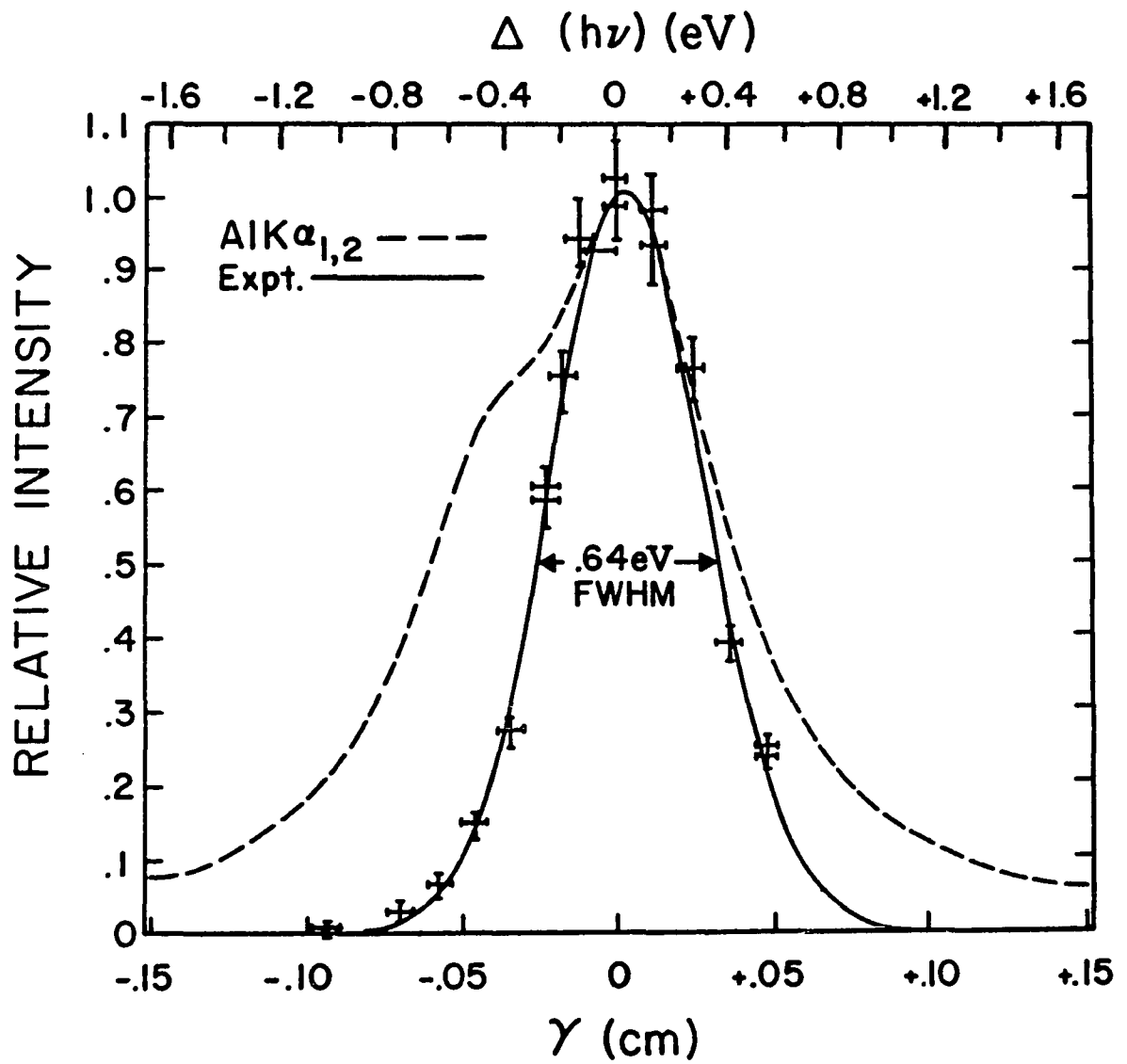


Figure IV-8 - Theoretical and experimental Cls spectra for a lens magnification of -5.0.  $\theta_0$  was taken to be  $30^\circ$ , and the modeling procedure requires experiment and theory to be identical at this angle. Spectra are shown on a fixed relative energy scale with 1 eV per division.

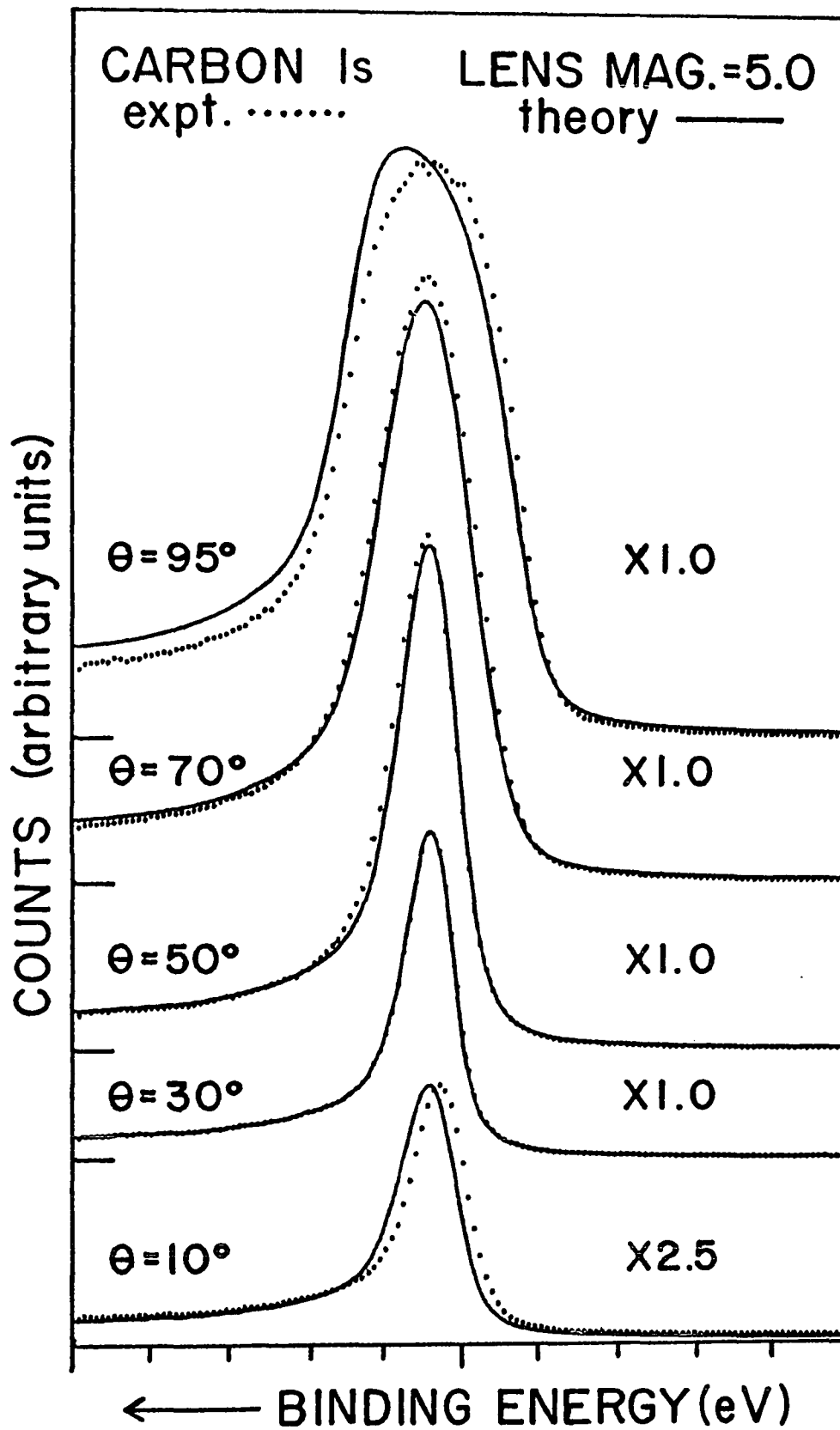


Figure IV-9 - Theoretical and experimental Cls spectra for a lens magnification of -2.3.  $\theta_0$  was taken to be  $60^\circ$ . Spectra are shown on a fixed relative energy scale with 1 eV per division.

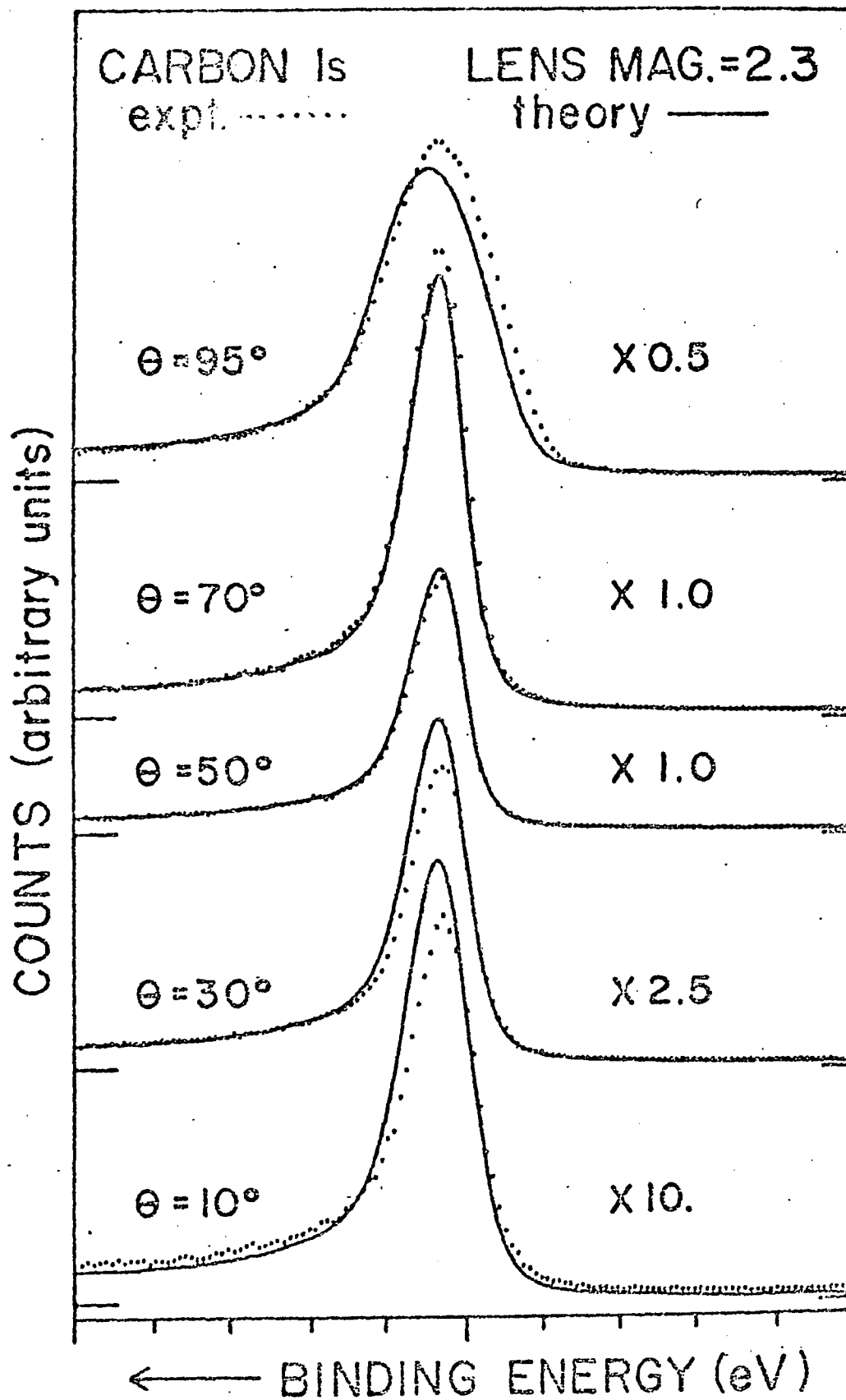


Figure IV-10 - Theoretical and experimental variation of the Cls total intensity with  $\theta$  for an optimally-aligned spectrometer with lens magnifications of -5.0 and -2.3. The dependence of intensity on angle is proportional to the response function  $R(\theta)$  as defined in equation 1.

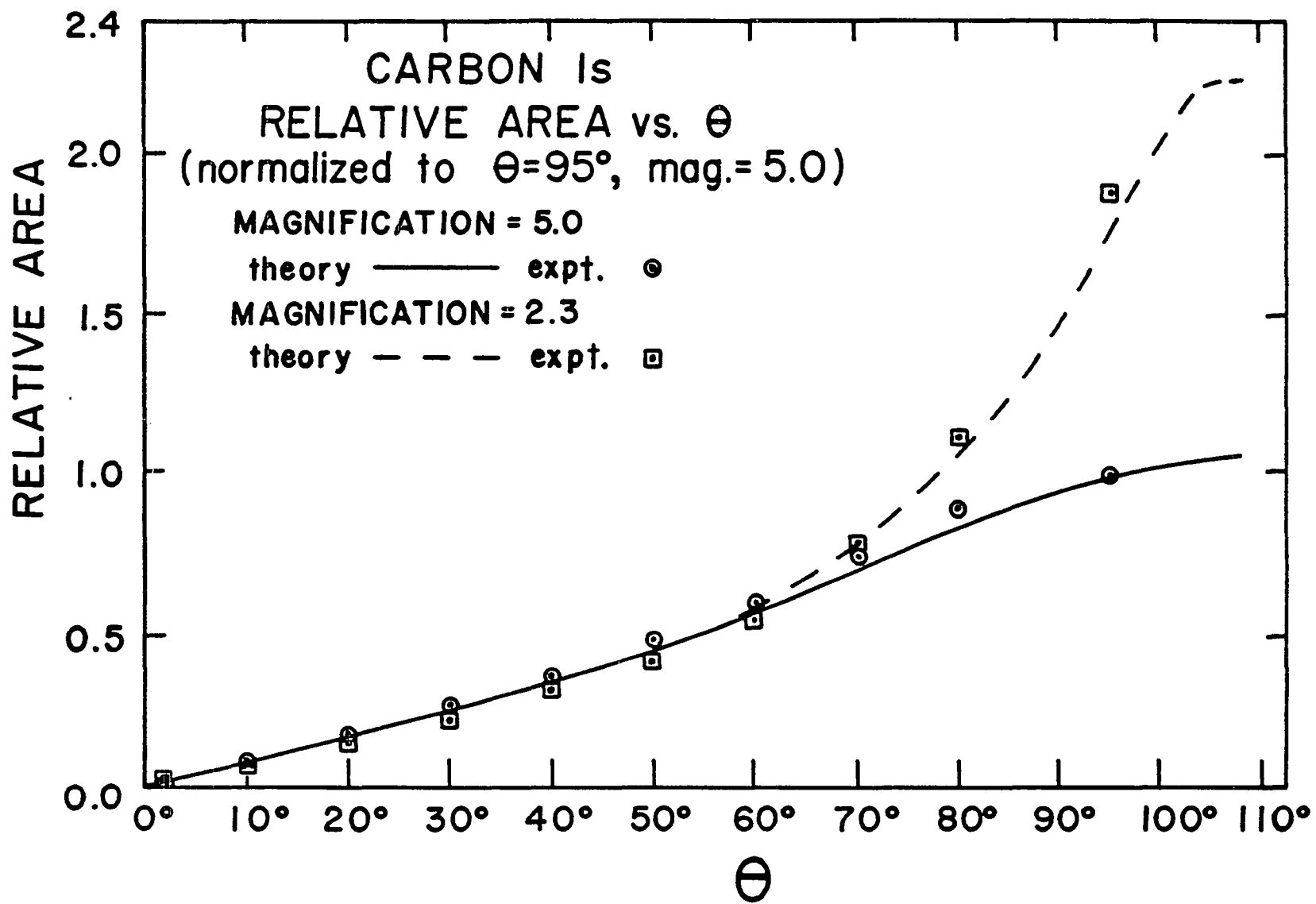


Figure IV-11 - Theoretical and experimental variation of the Cls FWHM with  $\theta$  for an optimally-aligned spectrometer at lens magnifications of -5.0 and -2.3.

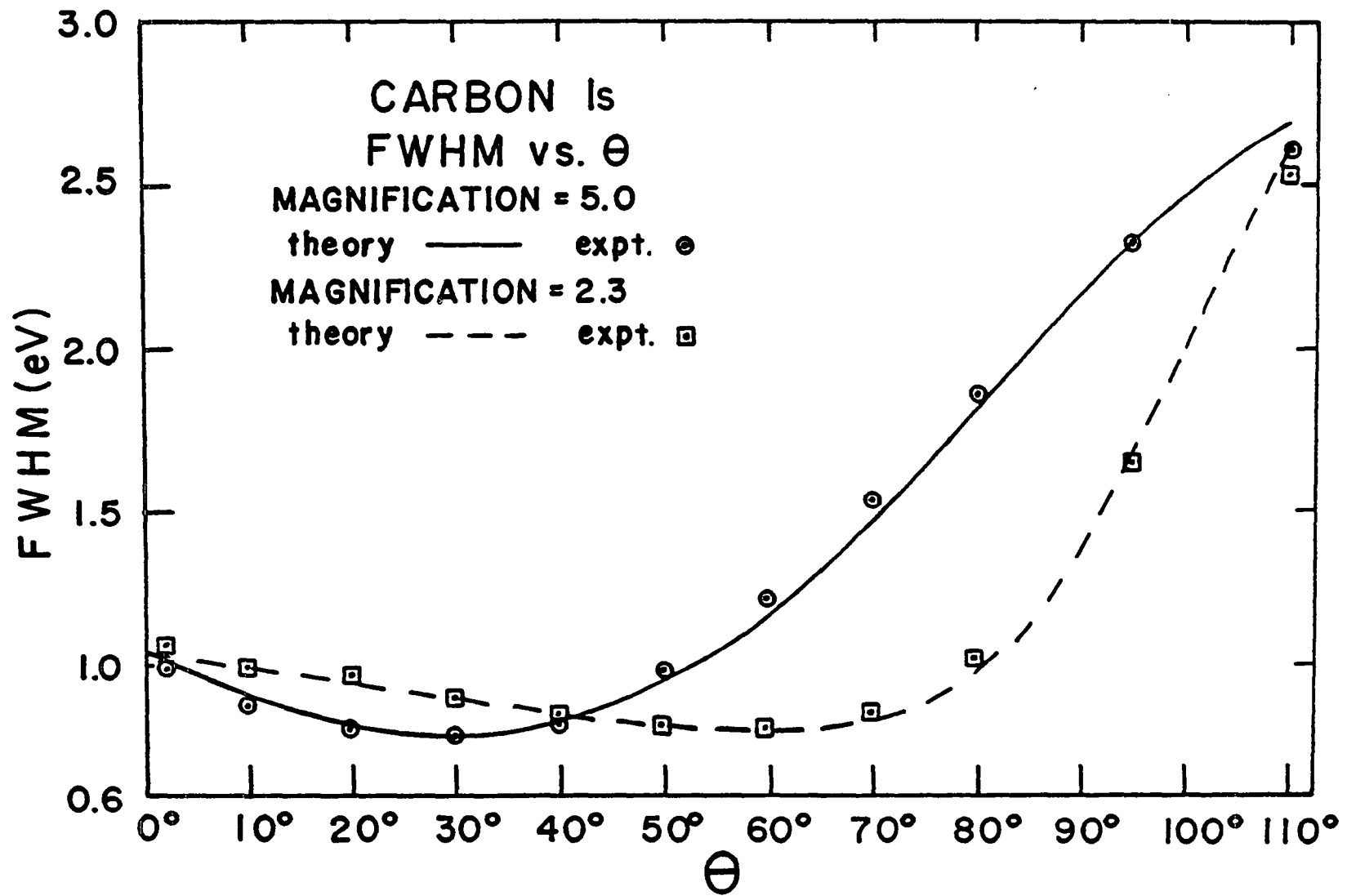


Figure IV-12 - Theoretical and experimental variation of  $Au4f_{7/2}$  total intensity with  $\theta$  for various cases of monochromator alignment. The differences between the curves reflect the dependence of  $R(\theta)$  on spectrometer alignment.

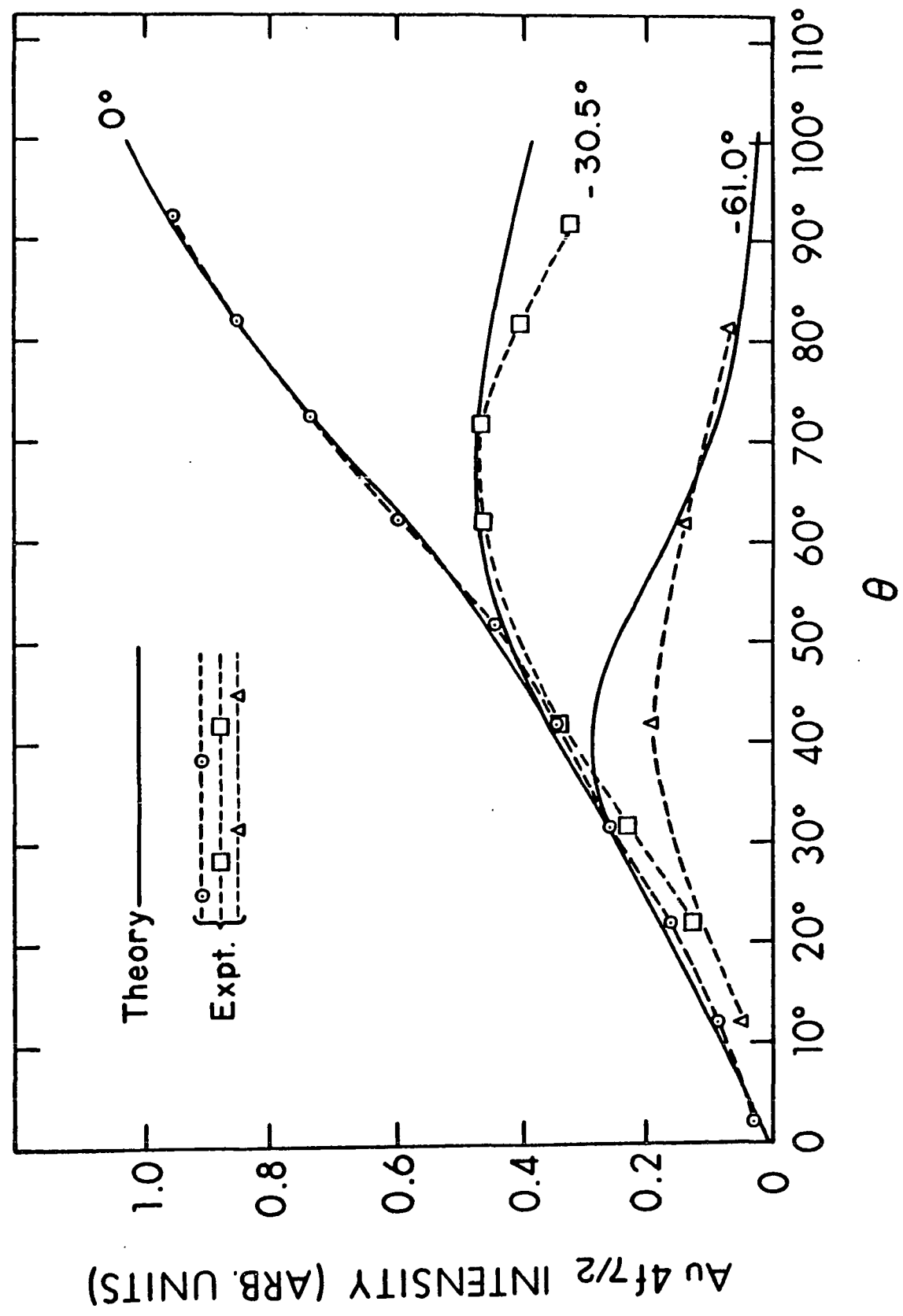
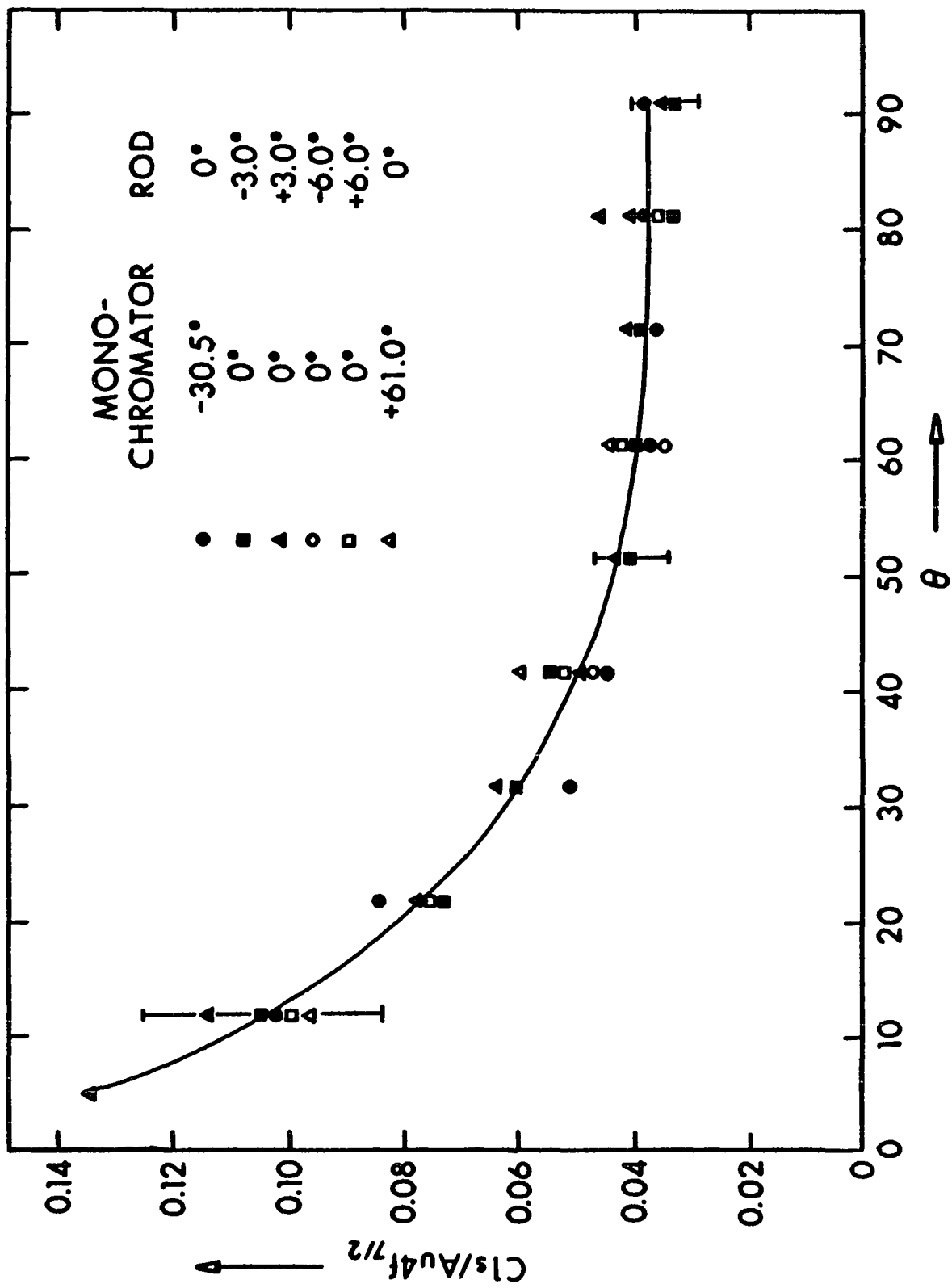


Figure IV-13 - Experimental Cls/Au4f<sub>7/2</sub> ratio angular distributions for various combinations of monochromator and specimen-rod alignment, with  $\theta_0$  corresponding to optimum. The C was present as a thin overlayer on the Au surface. All data points are described by one curve due to the cancellation of  $R(\theta)$  in the ratio measurements.



V. DIRECT OBSERVATION OF SURFACE-PROFILE EFFECTS  
ON X-RAY-PHOTOELECTRON ANGULAR DISTRIBUTIONS<sup>†</sup>

The potential utility of XPS angular distribution (AD) measurements for macroscopic surface characterizations has been pointed out in several prior studies<sup>1-6</sup>. In particular, the relative enhancement of photoelectron intensities from atoms nearer the surface that occurs for low (grazing) angles of electron escape has been experimentally demonstrated for several systems, and the forms of such enhancements are at least semi-quantitatively consistent with several versions of a straightforward theoretical model which assumes, among other things, an atomically flat substrate surface<sup>1,2,4-6</sup>. This model has also been extended by Fadley et al.,<sup>4,5</sup> so as to include the effects of surface roughness (that is, any sort of macroscopic deviation from planarity), and theoretical calculations for rough surfaces with simple periodic profiles have been carried out. Although these calculations indicate potentially significant effects of roughness on XPS angular distributions, no direct experimental observations of such phenomena have been reported prior to this work. Holloway<sup>7</sup> has also developed a statistical model for roughness effects on Auger electron intensities and this model correctly predicts certain trends in the variation of experimental intensities with angle for surfaces with relatively random roughness characteristics.

<sup>†</sup> Based on a paper "Direct Observation of Surface-Profile Effects on X-ray-Photoelectron Angular Distributions", R. J. Baird, C. S. Fadley, S. Kawamoto, and M. Mehta, Chem. Phys. Letters 34, 49 (1975).

In an attempt to assess roughness effects on XPS angular distributions, we have performed experiments on two types of polycrystalline specimens exhibiting some form of surface roughness: (1) aluminum diffraction gratings with profiles that were ideally triangular-periodic along one direction with a repeat length of approximately  $16,600 \text{ \AA}$  (corresponding to 600 lines/mm), and (2) nominally-flat aluminum specimens that were unidirectionally polished with 400 grit SiC abrasive, a procedure that should have left average scratch depths of approximately  $10,000\text{--}20,000 \text{ \AA}$ <sup>8</sup>. Core-level XPS AD's were obtained with a specially-modified Hewlett-Packard 5950A spectrometer in which monochromatized  $\text{AlK}_{\alpha}$  radiation was used for excitation. The angular acceptance of this spectrometer was  $\Delta\theta = 5^{\circ}$ ; the electron emission angle  $\theta$  is defined to be that between the electron exit direction and the planar average of the surface ( $0 \leq \theta \leq 90^{\circ}$ )<sup>4,5</sup>. This spectrometer was equipped with a custom-made rotating specimen holder that was compatible with the standard sliding-elastomeric-seal inlet system of the spectrometer<sup>5,9</sup>. This holder was in turn driven by a precision stepping motor connected to a small dedicated computer (Hewlett-Packard 2100A), thereby providing for automatic scanning of  $\theta$  and on-line analysis and storage of AD data<sup>9</sup>.

After ruling of the gratings directly in aluminum blanks by Perkin Elmer, Inc., or unidirectional polishing of the second type of specimen in our laboratory, all specimens were exposed to the atmosphere for extended periods (from one hour to several months) in order to build up a continuous, relatively thick, and very nearly uniform surface layer of aluminum oxide. The only type of surface cleaning performed after air

exposure was ultrasonication in various solvents to remove loose particulate matter and to minimize surface hydrocarbon buildup. After such cleaning, specimens were immediately inserted into the spectrometer, where AD measurements were carried out at  $\sim 5 \times 10^{-9}$  torr. Under these conditions, the relative intensities of all core peaks observed, namely those of oxygen, carbon, and aluminum, were quite stable with time at a given electron emission angle  $\theta$ . Furthermore, the chemically-shifted Al2p (oxide) and Al2p (metal) peaks were easily resolvable at any angle of escape, with a separation of approximately 2.5 eV and comparable intensities for  $\theta = 45^\circ$ . (Similar effects were also noted for Al2s (oxide) and Al2s (metal) peaks, but the Al2p doublet is somewhat easier to resolve.) Typical relative intensities for  $\theta = 45^\circ$  were Cls:Ols:Al2p (oxide):Al2p(metal) = 2:7:2:1. Of principal interest here is the angular-dependence of the intensity ratio Al2p(oxide)/Al2p(metal), which is amenable to rather simple theoretical analysis because of the cancellation of certain non-simple instrumental intensity functions in taking the ratio<sup>4,5</sup> and also because the attenuation lengths for Al2p (oxide) and Al2p (metal) photoelectrons will be essentially identical in either the oxide layers or superficial carbon-containing layers<sup>4</sup>. The latter simplification means that as a first-order approximation the effects of the carbon-containing layers can be neglected in analyzing Al2p(oxide)/Al2p(metal) ratio data, as both peaks will be attenuated by an identical factor at each point on the surface. (This neglect would be rigorously valid for a flat-surface specimen<sup>4</sup>.) Furthermore, because the attenuation length for AlK $\alpha$  x-rays in

aluminum is  $\sim 90,000 \text{ \AA}^{0.10}$ , and thus much greater than the typical dimensions of the surface irregularities on the specimens studied, it is also valid to neglect any effects due to x-ray attenuation or shading at the surface in discussing this data.

Such ratio data is presented as a function of the angle  $\theta$  in Figures V-1, V-2 and V-3 for diffraction gratings with well-defined blaze angles of  $10^\circ$ ,  $20^\circ$ , and  $43^\circ$ , respectively. The ideal surface geometries for these gratings are shown in the figures, and the definitions of the blaze angles are implicit. The AD data was accumulated in two parts, with  $\theta$  being varied stepwise from  $90^\circ$  to very low values along both of the two directions perpendicular to the grating grooves. The grating was rotated by  $180^\circ$  about an axis perpendicular to its surface between these two sets of measurements in order to provide for continuous illumination by the fixed-position x-ray source. The scales corresponding to the two different  $\theta$  variations are arbitrarily labelled  $\theta_+$  and  $\theta_-$  to distinguish them. For all three gratings, there is marked asymmetry in the experimental ratio data about the  $\theta = 90^\circ$  centerline. (All such measurements for a flat-surface specimen would be expected to be completely symmetric about this centerline.) The data for the  $10^\circ$  and  $20^\circ$  gratings are also rather similar in shape, with much more pronounced oxide enhancement toward low  $\theta_-$  and a maximum in the oxide/metal ratio for low  $\theta_+$ . The data for the  $43^\circ$  grating are distinctly different in shape, however, and exhibit greatest oxide enhancement for the relatively high angle of  $\theta_+ \approx 55^\circ$ .

In order to determine whether the observed effects are associated with surface profile, theoretical calculations of ratio angular distributions have been made. These calculations were based on the general rough-surface model presented previously by Fadley et al.<sup>4,5</sup>. The two effects of roughness allowed for in this model are (1) the shading of one point on the surface for electron escape by adjacent roughness contours (shading is assumed to be complete, as will be the case for the specimen studied here because typical roughness dimensions are much larger than electron attenuation lengths), and (2) the deviation of the true angle of electron emission  $\theta'$  associated with each differential element of surface area  $dA$  from the gross experimental emission angle  $\theta$  that is measured relative to the planar average of the surface. This model then predicts that the oxide/metal intensity ration will be given by (cf. equations (19) and (36) of reference 4):

$$\frac{Al2p(\text{oxide})}{Al2p(\text{metal})} = \frac{\rho_{Al}(\text{oxide}) \Lambda_e(\text{oxide})}{\rho_{Al}(\text{metal}) \Lambda_e(\text{metal})} \cdot \frac{\int_{A^R(\theta)} \left\{ 1 - \exp \left[ -t(\text{oxide}) / \Lambda_e(\text{oxide}) \sin \theta' \right] \right\} \sin \theta' dA}{\int_{A^R(\theta)} \exp \left[ -t(\text{oxide}) / \Lambda_e(\text{oxide}) \sin \theta' \right] \sin \theta' dA}$$

In this expression,  $\rho$  represents atomic density,  $\Lambda_e$  is an electron attenuation length,  $t(\text{oxide})$  is the oxide layer thickness (assumed constant over each surface),  $A^R(\theta)$  represents the electron-unshaded area of the rough surface for a given gross emission angle  $\theta$ , and  $dA$  is a differential element of area along the rough surface for which the true angle of emission is  $\theta'$  ( $0 \leq \theta' \leq 90^\circ$ ). For the idealized triangular-

periodic geometries shown in Figures V-1 - V-3 the integrals in this equation reduce to two-term sums, with each term representing one of the exposed faces of each triangle over which  $\theta'$  is a constant for a given  $\theta$ . Based upon previously measured values for the densities and electron attenuation lengths<sup>11,12</sup> in oxide and metal, the factor multiplying the ratio of integrals is estimated to be 0.70. Together with the assumed triangular geometry, the ratio  $t(\text{oxide})/\Lambda_e(\text{oxide})$ , an effective oxide layer thickness, thus determines the variation of the oxide/metal ratio with  $\theta$ .

As no direct measurements of effective oxide layer thickness were made, the angular distribution data was utilized to estimate this parameter in a self-consistent way. The estimation procedure involves noting that all three gratings were subjected to identical conditions of atmospheric exposure after ruling and therefore should have possessed oxide layers of nearly equal thicknesses. The latter statement is quantitatively verified by the fact that all three gratings exhibit very nearly the same minimum oxide/metal ratios; the values are 1.42, 1.32, and 1.33 for the  $10^\circ$ ,  $20^\circ$ , and  $43^\circ$  gratings respectively, corresponding to an average value of 1.35. These minima furthermore occur for  $\theta_*$  values very close to those for which the ideal geometry should yield a true emission angle of  $\theta' = 90^\circ$  for all unshaded surface, and it is at this condition that the ideal geometry should in theory yield a minimum oxide/metal ratio. The observed and theoretical minima locations in  $\theta_*$  are, respectively,  $70^\circ$  and  $80^\circ$  for the  $10^\circ$  grating,  $80^\circ$  and  $70^\circ$  for the  $20^\circ$  grating, and  $50^\circ$  and  $47^\circ$  for the  $43^\circ$  grating.

Therefore, it is a reasonable approximation to assume that the oxide/metal ratio of 1.35 corresponds to  $\theta' \approx 90^\circ$  for all unshaded surface, and that all three gratings possess an oxide layer of very nearly the same thickness. If this is the case, the equation above directly yields an estimate for  $t(\text{oxide})/\Lambda_e(\text{oxide})$  of 1.075. This value is furthermore consistent with prior studies of aluminum oxidation in air<sup>13</sup>, in that it yields an oxide layer thickness of  $\sim 18 \text{ \AA}$  (as based on the reported value for  $\Lambda_e(\text{oxide})$  of  $16.7 \text{ \AA}^{11}$ ).

Based on this empirical estimate for  $t(\text{oxide})/\Lambda_e(\text{oxide})$  of 1.075, the variation of  $\text{Al}2p(\text{oxide})/\text{Al}2p(\text{metal})$  with  $\theta$  was calculated for the three ideal grating geometries, as well as for a flat-surface reference. The theoretical curves obtained in this way are shown in Figures V-1 - V-3. The solid curves based on the ideal grating geometries correctly predict the overall shapes displayed by the data for all three gratings, with very good agreement being obtained for the specimen with  $10^\circ$  blaze angle. The sharp cutoffs in the curves occurring at  $\theta_+ \approx 10^\circ$  for the  $10^\circ$  grating and  $\theta_+ \approx 20^\circ$  for the  $20^\circ$  grating are caused by the onset of shading of the faces of the triangular grooves pointing toward the  $\theta_-$  direction. These cutoffs and their associated maxima are also reflected in the experimental data, although somewhat less dramatically, as would be expected if, for example, the true surface profile exhibited some rounding of the exposed triangular edges. For all three gratings, both experiment and theory exhibit similar regions in  $\theta$  over which the oxide-metal ratio decreases as  $\theta$  is decreased, with these being most pronounced for the  $43^\circ$  specimen. This phenomenon, which runs counter to the naive

expectation that decreasing  $\theta$  must always enhance surface-atom signals, has been predicted previously for a sinusoidally-rough surface<sup>4</sup> and is easily explained in terms of the rough-surface model utilized here. The experimental and theoretical positions of the maxima along  $\theta_+$  are also in approximate agreement, with discrepancies of approximately  $10^\circ$  for the  $10^\circ$  grating,  $14^\circ$  for the  $20^\circ$  grating, and  $30^\circ$  for the  $43^\circ$  grating.

The general shapes of the theoretical curves are furthermore not changed significantly with changes in the choice of  $t(\text{oxide})/\Lambda_e(\text{oxide})$ , although the minimum oxide/metal ratios and the amplitudes of the minimum-to- $\theta_+$  maximum excursions may change appreciably. For example, for the  $10^\circ$  grating with  $t(\text{oxide})/\Lambda_e(\text{oxide}) = 2.5$ , the minimum ratio is 7.85 and the  $\theta_+$  maximum ratio is 37.82. The overall agreement between theory and experiment is thus quite good, especially in view of the fact that the grating surfaces probably deviated somewhat from the ideal geometries assumed. Some slight deviations were verified qualitatively in scanning electron micrographs of these surfaces. One such deviation that does not appear to have altered AD forms significantly is the possible presence of small-scale roughness with typical dimensions of  $\sim 50 \text{ \AA}$  superimposed upon the much larger scale grating profile; theoretically, the presence of any such small-scale roughness should be quite effective in altering AD patterns. On the other hand, the experimental data may reflect a sensitivity of the theoretical grating curves to the choice of triangular geometry, as is illustrated by the dotted curve in Figure V-3. This curve represents a calculation for a triangular grating surface with blaze angle of  $43^\circ$  that deviates only

slightly from the ideal case, with included angles of  $43^\circ$ ,  $57^\circ$ , and  $80^\circ$ . This deviation is qualitatively consistent with scanning electron micrographs for this grating, and furthermore yields much better agreement between theory and experiment as to maximum oxide/metal ratio and overall peak width. More quantitative studies of the true grating profiles are now in progress.

In Figure V-4, Al2p(oxide)/Al2p(metal) data from a unidirectionally-polished aluminum specimen are presented. For this specimen, one complete set of AD data (including both  $\theta_+$  and  $\theta_-$  scans  $180^\circ$  opposed to one another) was accumulated for  $\theta$  variation both perpendicular to and parallel to the polishing grooves. The two pairs of  $\theta_+$ ,  $\theta_-$  data have been plotted over one another in this figure, and it is clear that there is no significant asymmetry about  $\theta = 90^\circ$  for this specimen; this finding is consistent with its mode of preparation. There is, however, a considerable difference between the relative enhancements of the oxide peak that occur for the perpendicular and parallel orientations. The oxide/metal ratio is approximately 2.5 times higher for the parallel orientation at low  $\theta$  values, although both orientations of necessity have the same ratio for  $\theta = 90^\circ$ . This behavior can be qualitatively explained by noting that in the perpendicular orientation, the unshaded surfaces remaining at low  $\theta$  will lie near the tops of the often steeply sloping sides of the polishing grooves, such that the true emission angle  $\theta'$  can still have a reasonably large average value. (This orientation would correspond very roughly to the situation occurring for the  $43^\circ$  grating of of Figure V-3.) In the parallel orientation, on the other hand, the

electron emission will be from surfaces that have relatively low slopes perpendicular to the emission direction, and therefore a lower average  $\theta'$  value will result. Because  $\theta'$  is generally lower for the parallel orientation, a greater surface enhancement is possible. On the other hand, the fact that the oxide/metal ratio in the perpendicular orientation changes by a factor of 1.8 between  $\theta = 90^\circ$  and  $\theta = 10^\circ$  also demonstrates experimentally that, even for extremely rough surfaces, some surface enhancement should be achievable at very low angles of electron escape, as has been suggested previously<sup>4</sup>.

In conclusion, these preliminary experimental peak-ratio angular distributions clearly show several pronounced effects due to the presence of surface roughness. Several of these effects have been qualitatively predicted in prior work on the basis of theoretical arguments<sup>4,5</sup>. For the relatively well characterized surface profiles represented by the diffraction gratings, there is good agreement between experiment and theory, particularly in view of certain simplifying assumptions that have been made. For the much more random roughness represented by the unidirectionally polished specimens, significant differences are also found between AD's obtained perpendicular to and parallel to the polishing direction. For all specimens, significant enhancement of surface-atom relative intensities can be achieved by a proper variation of  $\theta$ , but simply decreasing  $\theta$  does not always lead to that result for all specimens, again in agreement with theory.

Such roughness effects can occur whenever surface profile features with characteristic dimensions greater than or equal to photoelectron

attenuation lengths are present. Therefore, roughness effects may represent important considerations in the analysis of AD data from all but the most carefully prepared surfaces. With further refinements, it also should be possible to utilize such AD measurements to obtain certain types of surface profile information, as for example, concerning average surface slopes. One advantage of such a procedure would be its potential resolution, in that features with dimensions of the order of tens of Ångstroms should in principle be significant in producing alterations in observed angular distributions. Among the possible refinements would be more quantitative tests of theory against experiment for very well characterized regular profiles and more precise ultrahigh vacuum surface preparation and cleaning techniques. A further increase in the amount of information obtained might be achieved by shading the surface to be studied by vapor deposition of a different element onto it at a well-defined angle, and subsequently measuring AD's of all accessible core peaks for surface regions exposed to different deposition angles.

REFERENCES  
SECTION V.

1. C. S. Fadley and S. Å. L. Bergstrom, Phys. Lett. 35A (1971) 375; in D. A. Shirley (editor) Electron Spectroscopy, North Holland Publishing Co., Amsterdam, 1972, p. 233.
2. W. A. Fraser, J. V. Florio, W. N. Delgass, and W. D. Robertson, Surf. Sci. 36 (1973) 661.
3. B. L. Henke, Phys. Rev. A 6 (1972) 94.
4. C. S. Fadley, R. J. Baird, W. Siekhaus, T. Novakov, and S. Å. L. Bergström, J. Electron Spectrosc. 4 (1974) 93.
5. C. S. Fadley, J. Electron Spectrosc. 5 (1974) 725.
6. J. Brunner and H. Zogg, J. Electron Spectrosc. 5 (1974) 811.
7. P. H. Holloway, Abstract for 34th Physical Electronics Conference, Murray Hill, New Jersey, February 1974, and Sandia Laboratory Report SAND74-0434.
8. See for example, the AB Metal Digest, Vol. 11, no. 2/3 (1973), Buehler Ltd., Evanston, Illinois.
9. R. J. Baird and C. S. Fadley, manuscript in preparation.
10. B. L. Henke and M. Tester in Advances in X-ray Analysis, Vol. 18, Plenum Press, New York, 1975.
11. F. L. Battye, J. Liesegang, R. C. G. Leckey, and J. G. Jenkin, Phys. Lett. 49A (1974) 155.
12. H. Kanter, Phys. Rev. B 1 (1970) 2357.
13. J. E. Boggio and R. C. Plumb, J. Chem. Phys. 44 (1966) 1081.

Figure V-1 - The core-level peak area ratio for Al2p(oxide) and Al2p(metal) is plotted against  $\theta$  for an aluminum diffraction grating with  $10^\circ$  blaze angle. The experimental data consists of two separate scans of  $\theta$ , labelled by  $\theta_+$  and  $\theta_-$ . Both scans were made perpendicular to the groove direction in the manner indicated. Statistical error limits are shown on all data points for which the limits exceed the symbol size. For each point, the plus and minus limits are equal in magnitude. The ideal grating geometry is shown in the inset. The solid curve represents a theoretical calculation for the ideal geometry; the dotted curve is a theoretical result for a flat surface. All theoretical curves are based on an empirical value for  $t(\text{oxide})/\Lambda_e(\text{oxide})$  of 1.075.  $\Delta\theta = 5^\circ$  represents the angular spread accepted by the spectrometer.

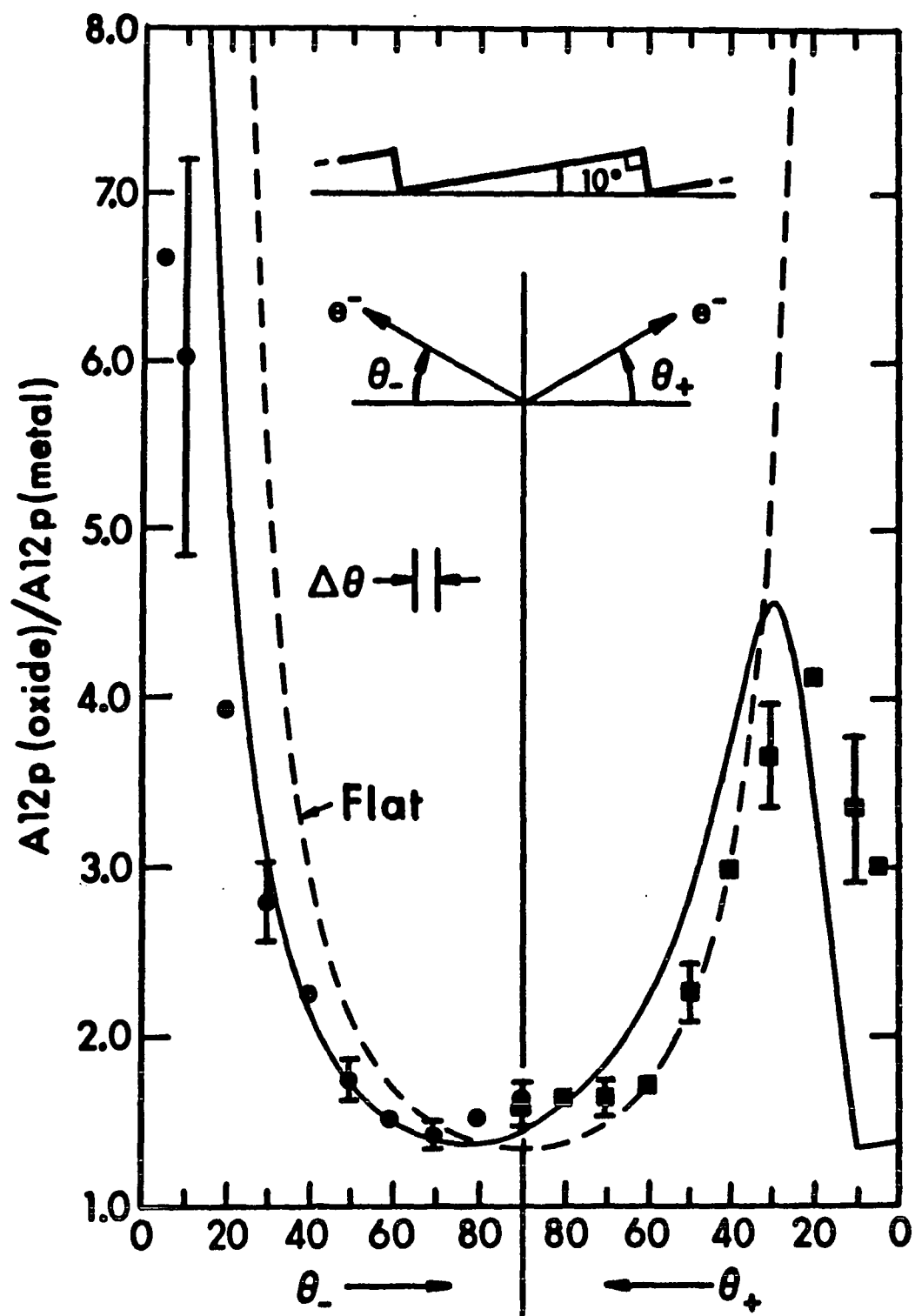


Figure V-2 - Analogous to Figure 1, but for an aluminum diffraction grating with  $20^\circ$  blaze angle.

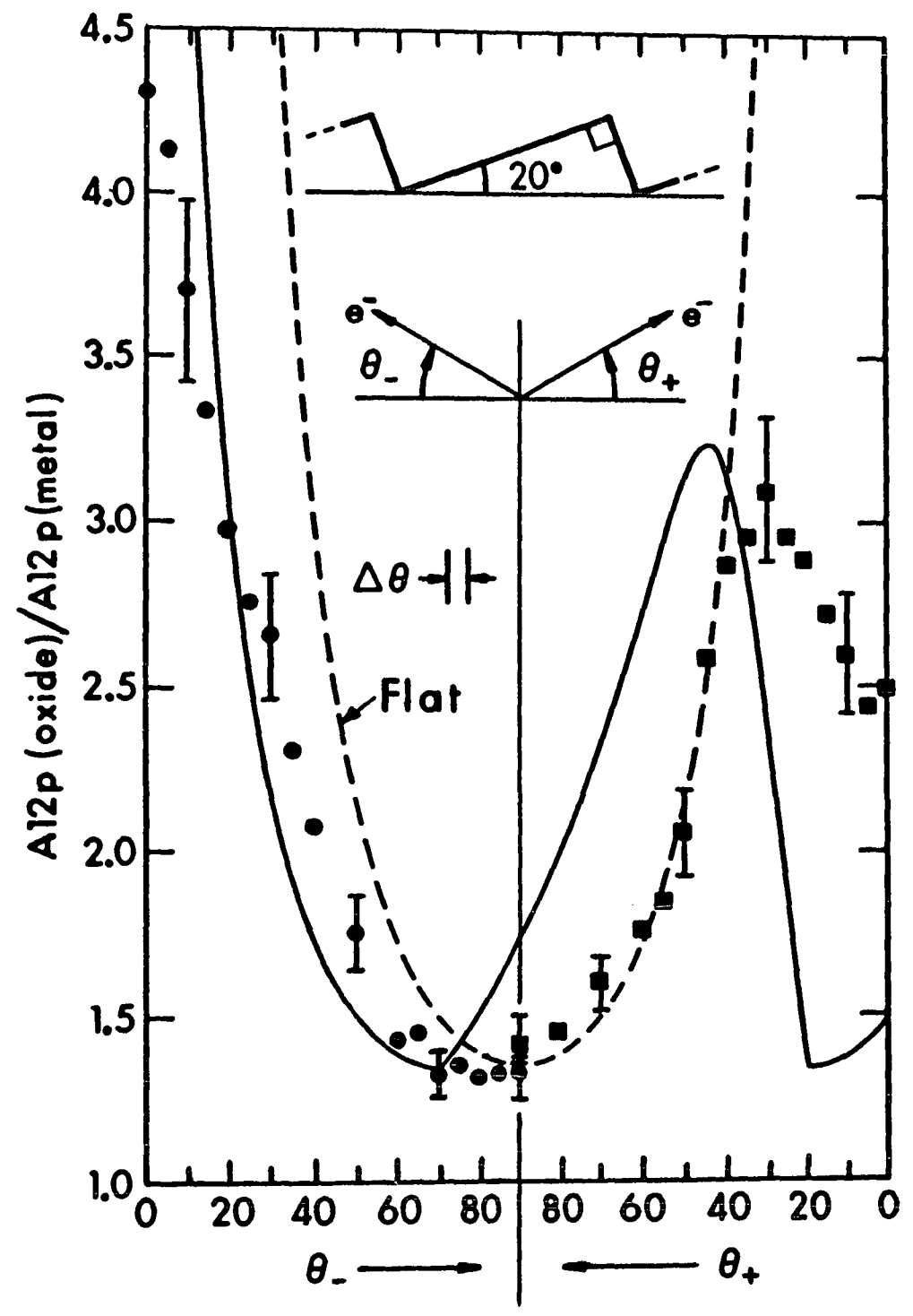


Figure V-3 - Analogous to Figure 1, but for an aluminum diffraction grating with  $43^\circ$  blaze angle. No flat-surface theoretical curve is shown. The dotted curve corresponds to a non-ideal triangular geometry based on the same blaze angle of  $43^\circ$ , but other included angles of  $57^\circ$  and  $80^\circ$ .

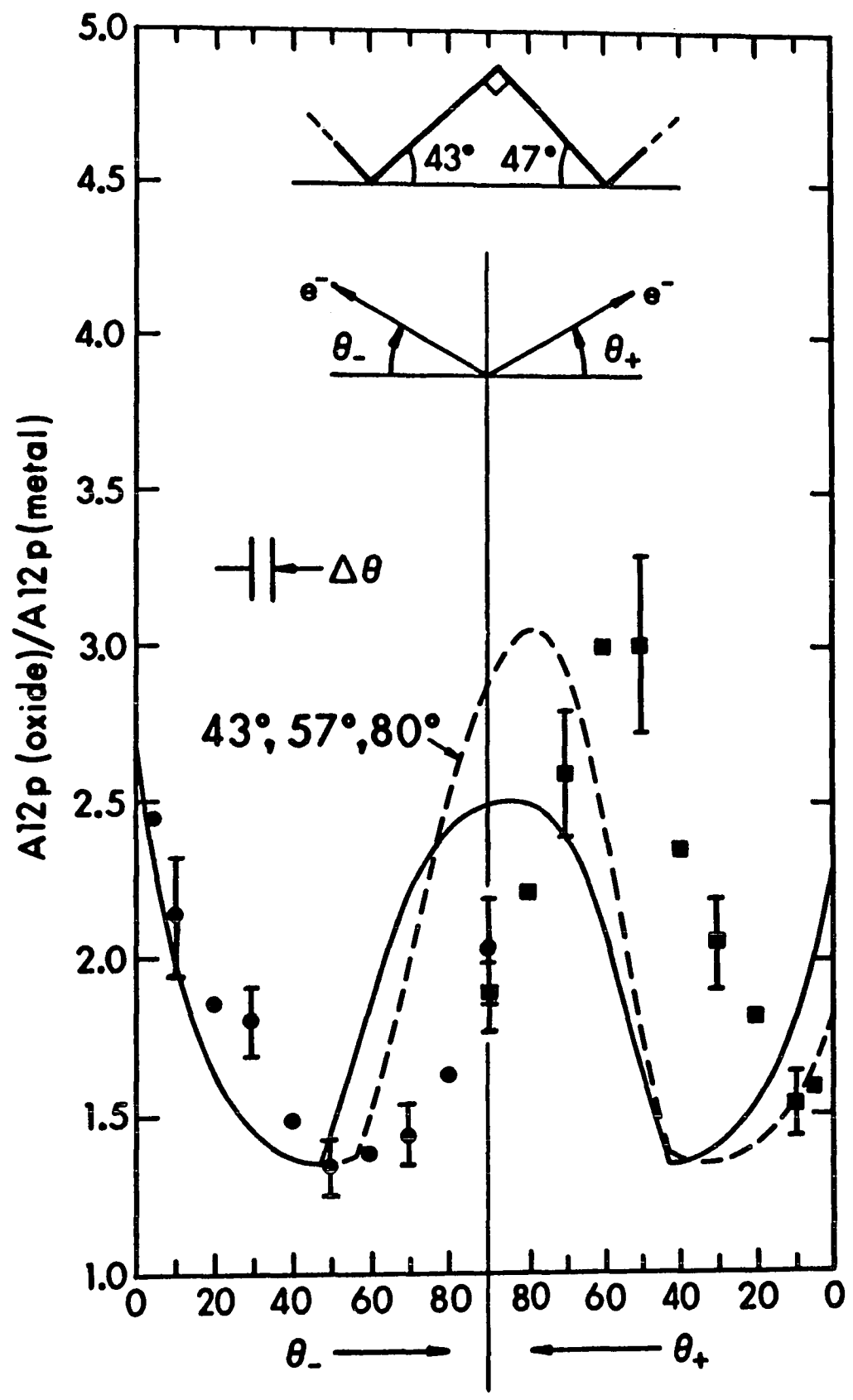
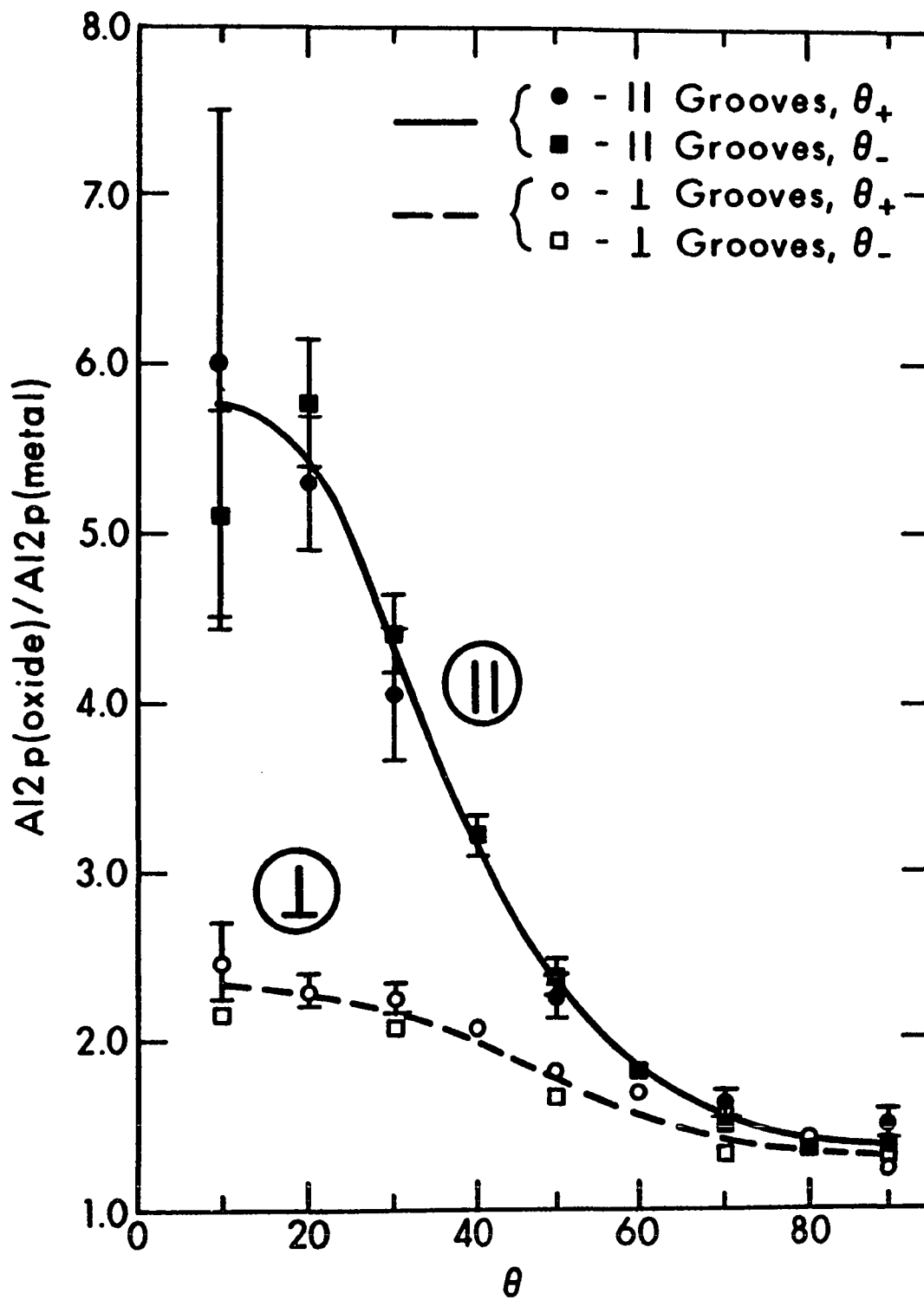


Figure V-4 - Core-level peak area ratio  $\text{Al2p(oxide)/Al2p(metal)}$  plotted against  $\theta$  for an aluminum specimen subjected to unidirectional polishing.  $\theta_+$  and  $\theta_-$  scans were performed for  $\theta$  variation perpendicular to and parallel to the polishing direction. The four sets of data are labelled in the figure. The curves are representations of the experimental data, and have no theoretical significance.



## VI. PLASMON LOSS EFFECTS

1. Introduction

Plasmon loss features are well known in electron spectroscopy, and have been observed as lower-kinetic-energy satellites of the no-loss peaks in ultraviolet photoelectron<sup>1</sup>, x-ray photoelectron<sup>2</sup>, and Auger electron-spectra<sup>3</sup>. Pollak et al.<sup>4</sup> have in particular studied the systematics of plasmon loss intensities in the XPS spectra of nine different metals for an experimental geometry with fixed angular orientation. However, the angular dependence of such loss intensities in XPS has not previously been investigated beyond the qualitative observation that surface plasmons become more significant for low or grazing angles of electron escape<sup>5</sup>.

The interpretation of XPS plasmon loss structure in terms of the often used three-step model<sup>6</sup> of bulk optical excitation, electron transport to the surface, and electron escape through the surface is complicated by several effects. First, the inelastic mean-free-path used to describe electron attenuation due to plasmon excitation in the transport step of such a model becomes a function of position and direction of propagation, in addition to being a function of energy. The position dependence of the mean-free-path arises from the presence of the surface and the orthogonality of the surface- and bulk-plasmon modes of oscillation, as has been discussed by Feibelman<sup>7,8</sup> for the case of a jellium solid. In particular, it has been shown<sup>7,8</sup> that the probability for exciting surface plasmons increases for electrons moving near the

surface, with a concomitant decrease occurring in the probability of exciting bulk plasmons. It has also been shown that the probability for exciting a surface plasmon should be proportional to the component of the electron momentum parallel to the sample surface. As a result of these early theoretical studies of plasmon inelastic scattering, Feibelman<sup>7,8</sup> proposed using the plasmon loss structure of Auger electrons for determining the depth of an Auger emitter below a surface.

A second complication of the three-step model arises from the possibility of a breakdown of the one-electron description of the optical excitation step. Langreth<sup>9</sup> has pointed out that a localized core hole created in the photoemission process could itself couple to the plasma field and give rise to what is termed "intrinsic" plasmon emission. This process is distinct from the "extrinsic" plasmons which arise from the coupling of the electric field of a moving electron to fluctuations in the electron density of the material. Interference effects between the localized hole and the exciting electron in which virtual plasmons created by one are absorbed by the other can also occur<sup>9</sup>.

In order to allow for a more general treatment of such plasmon creation processes, several theoretical descriptions of photoemission have been developed which include inelastic losses as a many-body effect in the photoemission process. Chang and Langreth<sup>10,11</sup> have presented a full many-body treatment of photoemission in which the effects of the solid surface and the core-hole are included. Šunjić, Sokčević, and Lucas<sup>12</sup> have discussed a similar but somewhat simplified theory which is capable of providing quantitative results for comparison to experimental

data. Feibelman also has extended his earlier extrinsic-only model to include the effects of the core hole<sup>13</sup>. Also, Bradshaw and co-workers<sup>14</sup> have specialized the many-body treatment to the case of an adsorbate atom on a solid surface. All numerical results obtained from these theories to date have been for the case of a uniform-density, semi-infinite, jellium solid with a step-function gradient of electron density at the surface. Very recently, Penn<sup>15</sup> has also discussed a three-step theoretical model for such processes that includes effects due to electron-electron scattering and plasmon dispersion.

As a result of these theoretical predictions of intrinsic plasmon creation, several prior fixed-angle XPS studies have been carried out in an attempt to assess the importance of these effects. Pardee et al.<sup>16</sup> have presented a statistical analysis of the intensities of the plasmon losses occurring below the 2s x-ray photoelectron peaks of Na, Mg, and Al, and have concluded that intrinsic effects were not observed in Mg and Al, but that they might be present in Na. Fuggle et al.<sup>17</sup> sought to differentiate between intrinsic and extrinsic effects by studying thin Al films evaporated onto a Mn substrate; they concluded that there was some intrinsic component in the plasmon satellites of the Al2s level. More recently, Bradshaw et al.<sup>14</sup> have investigated the angular dependence of the loss structure associated with the O1s level of oxygen chemisorbed on an aluminum surface: only one surface plasmon satellite was observed and it was concluded from comparison with theory that there is a very weak intrinsic component in this peak.

Except for the work by Bradshaw et al. on chemisorbed oxygen, all of the previous experiments on plasmon intensities have been carried out at fixed angles of electron escape with respect to the surface. Therefore, it is of considerable interest to study the angular dependence of plasmon loss structure from a well defined nearly-free-electron metal. Such angle-resolved experiments have been found in exploratory studies to exhibit varying bulk- and surface-contributions to plasmon emission<sup>5</sup>, since electrons which escape at near grazing angles tend to originate nearer to the surface. In this investigation, the detailed angular dependence of core-peak plasmon loss features has been measured for both clean aluminum surfaces and similar surfaces with adsorbed oxygen at low coverages of  $\sim 0.16$  monolayer. A preliminary account of the data obtained has been presented previously<sup>18</sup>. A more extensive set of loss intensities are given here and compared with the results of theoretical calculations based upon the work of both Šunjić and co-workers<sup>12,19-20</sup> and Feibelman<sup>7,8,13</sup>, thus permitting a more exact test of these models than has been possible previously.

## 2. Theory

A full discussion of the basic theoretical model that will be used in interpreting such angle-resolved XPS loss spectra can be found in the original papers by Šunjić et al.<sup>12,19,20</sup>. Thus, only certain salient points necessary for the present application will be presented here. The inelastic scattering processes are divided into two classes: short-range scattering associated primarily with electron-hole pair production, and long-range scattering associated with plasmon production. If it is

assumed that these two classes of scattering are independent and do not interface with each other, then the probability of inelastic scattering from a state of energy  $E_0$  into another state with an overall energy transfer of  $\Delta E$  for the combination of both processes is just the product of the individual probabilities for the two types of scattering. If the probabilities of a given type of plasmon excitation and given short-range excitation are denoted  $P_{p\ell}$  and  $P_{sr}$ , the overall probability  $P$  can thus be written:

$$P(E_0; \Delta E, E, \ell, \theta) = P_{p\ell}(E_0; \Delta E - E, \ell, \theta) P_{sr}(E_0; E, \ell, \theta), \quad (\text{VI-1})$$

in which  $E$  is the energy loss associated with short-range processes,  $\Delta E - E$  is the loss due to plasmon creation,  $\ell$  is the perpendicular distance below the surface at which the emitted electron was excited, and  $\theta$  is the angle of emission with respect to the surface (defined here such that  $\theta = 90^\circ$  corresponds to normal emission). The plasmon energy loss  $\Delta E - E$  will in general correspond to the creation of  $m$  surface plasmons and  $n$  bulk plasmons and so will be equal to  $E_{mn} = m\hbar\omega_s + n\hbar\omega_p$ , with  $\omega_s$  and  $\omega_p$  the surface and bulk plasmon frequencies, respectively. The probability for plasmon creation is also found to be a function of the lifetime of the core hole ( $\tau$ ), the plasmon frequencies  $\omega_s$  and  $\omega_p$ , and a non-uniquely-defined cutoff wave vector  $k_c$  above which plasmons are assumed not to propagate<sup>8,9,12,19,20</sup>; for a given material and core level, these are thus all fixed quantities.

The energy loss spectrum at a given angle can now be calculated by integrating equation IV-1 over the short-range energy loss and depth

$$P(E_0; \Delta E, \theta) = \iint P_{p\ell}(E_0; \Delta E - E, \ell, \theta) P_{sr}(E_0; E, \ell, \theta) dE d\ell. \quad (\text{VI-2})$$

Šunjić and co-workers point out that equation VI-2 can only be easily used to describe elastic short-range processes ( $E=0$ ). However, if only the area of the loss peak associated with the emission of  $m$  surface plasmons and  $n$  bulk plasmons is desired, then it is sufficient to average equation VI-2 over an interval of width  $D$  centered at the loss  $E_{mn}$ . Carrying out this integration and noting that  $E_{mn} \ll E_0$  for a typical XPS spectrum, one obtains

$$P_{mn}(E_0, \theta) = \frac{1}{D} \int_{E_{mn} - \frac{D}{2}}^{E_{mn} + \frac{D}{2}} P(E_0; \Delta E, \theta) d(\Delta E) \simeq \int_0^{\infty} P_{p\ell}(E_0; E_{mn}, \ell, \theta) \left\{ \frac{1}{D} \int_0^D P_{sr}(E_0; E, \ell, \theta) dE \right\} d\ell. \quad (\text{VI-3})$$

The factor  $P_{p\ell}(E_0; E_{mn}, \ell, 0)$  is furthermore given by an expression with the form of a Poisson distribution for the probability of emitting  $m$  surface and  $n$  bulk plasmons:

$$P_{p\ell}(E_0; E_{mn}, \ell, 0) = e^{-(Q_S + Q_B)} \cdot \frac{Q_S^m Q_B^n}{m!n!}. \quad (\text{VI-4})$$

The quantities  $Q_B$  and  $Q_S$  result from the many-body treatment of the photoemission process and contain contributions from extrinsic, intrinsic, and interference effects in plasmon creation.

The short-range scattering effects characterized by  $P_{sr}$  can now be treated conveniently, because instead of  $P_{sr}(E_0; E, \ell, \theta)$  for a particular scattering  $E_0 \rightarrow E_0 - E$ , an average probability for short-range scattering

that will remain the loss peak spanning  $E_0 - E_{mn} \pm D/2$  can be calculated as:

$$\bar{P}_{sr}(E_0 - E_{mn}; \ell, \theta) = \frac{1}{D} \int_0^D P_{sr}(E_0; E, \ell, \theta) dE. \quad (VI-5)$$

This averaged quantity can then be connected with the usual description of extrinsic inelastic scattering losses in terms of a mean-free-path, so that if the short-range scattering mechanisms are assumed to be isotropic,

$$\bar{P}_{sr}(E_0 - E_{mn}; \ell, \theta) = \exp \left[ -\ell / \lambda_{sr}(E_0) \sin\theta \right], \quad (VI-6)$$

in which  $\lambda_{sr}(E_0)$  is the mean-free-path for short-range scattering associated with an electron of energy  $E_0$ . Substituting equations VI-5 and VI-6 into equation VI-2 yields

$$P_{mn}(E_0; \theta) = \int_0^\infty P_{pl}(E_0; E_{mn}, \ell, \theta) \exp \left[ -\ell / \lambda_{sr}(E_0) \sin\theta \right] d\ell. \quad (VI-7)$$

For several reasons, theory can best be compared with experimental data in terms of the ratios of the areas of the different loss peaks to the area of the no-loss peak, as calculated from:

$$R_{mn} \equiv \frac{P_{mn}}{P_{00}}. \quad (VI-8)$$

$R_{mn}$  is thus defined to be the area of the loss peak associated with exciting  $m$  surface and  $n$  bulk plasmons divided by the area of the no-loss peak. Such ratios normalize the loss peaks to the no-loss peak and cancel a common factor for the rate of production of photoelectrons which is present in both  $P_{mn}$  and  $P_{00}$  in the theory. Ratio measurements of this

type also cancel out an angle-dependent instrument response function which significantly affects absolute spectral intensities, and to a lesser degree, peak widths<sup>22,23</sup>.

### 3. Experimental

All spectra were acquired with a Hewlett-Packard 5950A photoelectron spectrometer utilizing monochromatized AlK $\alpha$  radiation. The instrument was modified so as to provide ultrahigh vacuum conditions and also to allow for automated in situ rotation of the sample about an axis lying in its surface and perpendicular to the plane defined by the x-ray incidence direction and the mean electron emission direction. This rotation thus varied the emission angle  $\theta$  over its full range, with  $\theta = 0^\circ$  corresponding to grazing exit. The angular acceptance of the spectrometer was a cone of  $3.7^\circ$  half-angle (a solid angle of  $\sim 1.3 \times 10^{-2}$  steradians)<sup>22</sup>.

Ultrahigh vacuum conditions were obtained by replacing the standard differentially-pumped, sliding-seal inlet system with a bakeable, all-metal bellows assembly. This bellows system allowed the sample to be translated a distance of  $\sim 0.8$  m from an isolatable sample preparation chamber into the XPS spectrometer. The pressures in the sample preparation chamber and in the XPS system were monitored with nude Bayard-Alpert ionization gauges and were in the range  $1 - 3 \times 10^{-10}$  torr during all measurements. As determined from peak heights in mass spectra obtained with a quadrupole spectrometer (Uthe 100C) mounted on the sample preparation chamber, the composition of the residual gas was approximately 36% H<sub>2</sub>, 8% CH<sub>4</sub>, 17% H<sub>2</sub>O, 22% CO/N<sub>2</sub>, and 5% CO<sub>2</sub>. Motion for

varying the sample orientation with respect to the analyzer was provided by a precision rotary-motion feedthrough driven by a  $0.9^\circ$ /step stepping motor which was interfaced to a Hewlett-Packard 2100A minicomputer used for data acquisition. A detailed analysis of the systematics of performing angle-resolved measurements with a dispersion-compensating spectrometer such as the Hewlett-Packard 5950A is presented elsewhere<sup>22</sup>; it is found that intensity, and, to a lesser degree, resolution, are both functions of sample orientation. However, it has also been shown that these instrument response function effects cancel as long as only relative area measurements are made at a given angle<sup>22,23</sup>.

Both bulk polycrystalline samples and films vapor-deposited in situ were investigated in order to assess the effects of sample surface roughness and preparation procedure on the angular distributions. The bulk samples were prepared by mechanically polishing 99.999% pure polycrystalline aluminum (Materials Research Corp., Marz Grade) to a mirror finish with SiC paper, diamond paste, and finally CeO (Buehler, Miromet<sup>®</sup>) abrasives. Attempts at electropolishing the polycrystalline samples gave a hazy orange-peel surface which was not deemed suitable for angular-distribution measurements due to excess surface roughness effects. After inserting the mechanically-polished specimens into the vacuum system and baking for 48 hours at  $250^\circ\text{C}$ , the XPS spectra obtained showed a heavy oxide layer with some remnants of the CeO abrasive. Argon ion bombardment for 2 hours with  $\sim 10\ \mu\text{A}$  of beam current at 1 kV accelerating potential removed all of the Ce and reduced the O1s intensity to a minimum observed level of  $\sim 7\%$  of the Al2s intensity at a

detection angle of  $\theta = 45^\circ$ . This corresponds to an oxygen coverage of  $\sim 0.06$  monolayers, as estimated either by assuming a non-attenuating overlayer and using theoretical photoelectric cross sections, or by comparing observed O1s/Al2s relative intensities with that for the approximately saturated monolayer occurring at  $\sim 100$  Langmuirs exposure<sup>24</sup>. The only other contaminant present on the bulk samples was some residual argon from the ion bombardment (Ar2p/Al2s  $\approx 0.08$ ).

The second type of sample was prepared by vapor-depositing 99.999% pure Al from an aluminum-coated tungsten filament onto an ultrasmooth glass substrate (electronic grade Corning 7059) with an RMS surface roughness of  $\sim 30 \text{ \AA}$  and a maximum surface slope of  $\leq 1^\circ$ <sup>25</sup>. The films were deposited in less than 30 sec; the pressure during the deposition rose into the  $10^{-8}$  torr range and fell back into the  $10^{-10}$  torr range within 2 min after deposition. These deposited samples showed no impurity except oxygen, and the O1s to Al2s ratio at  $\theta = 45^\circ$  was .08, corresponding to a 0.07 monolayer coverage.

The O1s spectra obtained from adsorbed oxygen are from a bulk sample that was allowed to remain in the XPS chamber for 3 days at  $2 \times 10^{-10}$  torr. The principle source of oxygen was thus water in the residual gas. The oxygen coverage, as estimated from a comparison of the O1s relative intensity to those obtained in a series of controlled oxygen exposures<sup>24</sup>, is 0.15 monolayer. (It thus corresponds very closely to the oxygen coverage quoted by Bradshaw et al.<sup>14</sup>).

The experimental area ratios were derived by least-squares fitting symmetric gaussian peak shapes to the loss peaks and asymmetric gaussian

peak shapes to the no-loss peaks, with provision for the inclusion of an asymptotically constant "inelastic tail" at kinetic energies below each peak. The details of this fitting routine have been described previously<sup>26</sup>.

#### 4. Results and Discussion

Representative Al2p spectra spanning the angle range studied are shown in Figure IV-1. The Al2p region was chosen for detailed analysis rather than the Al2s region because Al2s spectra are complicated by the low-energy end of the Al2p loss structure. The no-loss peak was found to be best fit by a bi-gaussian peak shape made up of two gaussian halves with different full widths at half-maximum intensity. This peak shape permitted allowing for several possible sources of asymmetry in the no-loss Al2p peak: the presence of the unresolved spin-orbit doublet, the occurrence of a low-energy tail due to electron-hole pair creation during the formation of the core-hole<sup>27</sup>, and certain instrumental sources of low-energy asymmetry<sup>22</sup>. The much broader loss peaks were adequately fit by simple gaussian peak shapes. A constant background corresponding to the mean high-energy spectral intensity was also subtracted from each spectrum before analysis. The least-squares program was able to converge to reasonable fits with the inclusion of the following peaks: no-loss, one- and two-bulk losses, one-surface loss and one-surface-plus-one-bulk loss. (Although a very weak loss peak corresponding to the creation of two surface plasmons is observed in the  $\theta = 2^\circ$  spectrum at an energy of 21.0 eV below the no-loss peak, negligible error was incurred by neglecting it in the least-squares analysis.) The positions, widths, and

areas of all peaks were treated as variable parameters, with the single exception of the position of the one-surface-plus-one-bulk peak, which was fixed so as to be consistent with the positions determined for the other peaks. Representative fits are shown together with all component peaks in Figure VI-1. The average bulk- and surface-plasmon energies were found from this analysis to be  $\hbar\omega_p = 15.7 \pm .1\text{eV}$  and  $\hbar\omega_s = 11.0 \pm .2\text{eV}$ , respectively. To within the accuracies quoted, these values were observed to be independent of sample preparation and angle. The bulk plasmon energy is in good agreement with values reported in other studies<sup>3,4</sup>, but the surface plasmon energy is somewhat higher ( $\sim 0.5\text{ eV}$ ) than in prior work<sup>3,4</sup>. The present experimental values are also in good agreement with the theoretical plasmon energies for jellium with the electron density of aluminum, which are  $\hbar\omega_p = 15.8\text{ eV}$  and  $\hbar\omega_s = 11.2\text{ eV}$ .

As can be seen in Figure VI-1, the loss features associated with surface plasmon excitation are accentuated in relative intensity at low angles of electron emission, while the bulk plasmon loss features are significantly attenuated at low angle. Figure VI-2 compares the experimentally-observed relative intensities of the features involving only bulk losses ( $R_{\text{on}}$ ) to various theoretical calculations over the full range of electron emission angles. One set of values for  $R_{\text{mn}}$  as a function of angle and  $\lambda_{\text{sr}}$  has been obtained from Šunjić<sup>21</sup>; these are denoted  $R_{\text{mn}}(\text{S})$  and include both extrinsic and intrinsic effects. In these calculations, the values of the input parameters were taken to be  $\hbar\omega_p = 15.2\text{ eV}$ ,  $\hbar\omega_s = 10.8\text{ eV}$ ;  $k_c = 1.0\text{ \AA}^{-1}$ , and  $\gamma = 1/\tau = 3 \times 10^{13}\text{ sec}^{-1}$ . Appropriate values of  $Q_S$  and  $Q_B$  were also obtained from

Feibelman<sup>13</sup>, and equations IV-4 and IV-7 were then used to determine a second set of  $R_{mn}$  values, which are denoted by  $R_{mn}(F)$  or  $R_{mn}(F,ex)$ , with the latter including only extrinsic effects. The only significant difference in the basic parameters of the Feibelman calculations were the use of a slightly larger cutoff wave vector of  $k_c = 1.3 \text{ \AA}^{-1}$ . The short-range mean-free-path,  $\lambda_{sr}$ , was estimated from prior experimental data to be  $24 \text{ \AA}$ . This value is based on Kanter's measurements<sup>28</sup> of the transmission of 1.5 keV and 2.0 keV electrons through thin Al films, which permitted a separation of plasmon and short-range scattering processes and also indicate that short-range losses are much more probable than plasmon excitation.

The relative intensities  $R_{01}$  and  $R_{02}$  considered in Figure IV-2 are the ratios of the areas of the one-bulk and two-bulk loss peaks to the area of the no-loss peak, respectively. For both loss peaks, the area ratios are in approximate agreement with theory both in magnitude and functional form. However, the experimental values are consistently below theoretical predictions including both extrinsic and intrinsic effects by from 25-35%, and the numbers calculated using the methods of Šunjić and Feibelman differ by 20-30%. The discrepancies between theory and experiment could arise from several sources: (1) Theory may overestimate the contribution from intrinsic effects. To assess the potential magnitude of this source, the dotted curves in Figure VI-2 show the theoretically predicted angular dependence of the area ratios when only extrinsic effects are included, as based on the model of Feibelman<sup>13</sup>. In both cases, these curves lie below the experimentally

observed ratios by from 30-50%. It is thus suggested that, although some component of intrinsic creation is present in the data, the calculations include it too strongly. (2) The value chosen for  $\lambda_{sr}$  may be incorrect. For example, if  $\lambda_{sr}$  is taken to be equal to  $15 \text{ \AA}$  instead of  $24 \text{ \AA}$ , then theory including both extrinsic and intrinsic effects is in better agreement with experiment. For example, values based upon Šunjić's calculations with  $\lambda_{sr} = 15 \text{ \AA}$  are  $R_{01}(\theta = 90^\circ) = .55$  and  $R_{02}(\theta = 90^\circ) = .18$ , in very good agreement with the experimental results. However, a  $\lambda_{sr}$  as short at  $15 \text{ \AA}$  is not consistent with the available data on overall inelastic scattering lengths  $\lambda$  in aluminum (which by definition include both short-range and extrinsic plasmon effects). Two separate determinations by Kanter<sup>28</sup> and Tracy<sup>29</sup> of  $\lambda$  at the  $\sim 1.5 \text{ keV}$  energy of interest here yield values in very good agreement at  $19 \pm 1 \text{ \AA}$ . If the mean-free-path for extrinsic plasmons production is denoted  $\lambda_{p1}$ , then  $\lambda^{-1} = \lambda_{sr}^{-1} + \lambda_{p1}^{-1}$ , and  $\lambda_{sr}$  cannot be shorter than  $\lambda$ .  $\lambda_{p1}$  is found to be  $\sim 70 \text{ \AA}$ <sup>28</sup>. Our estimate of  $\lambda_{sr}$  is based on an extrapolation of Kanter's values for  $\lambda$  and  $\lambda_{p1}$  to the Al2p kinetic energy of 1410 eV.

(3) A further possibility is that the constant inelastic tails derived for the various peaks in each spectrum were somehow too high, thereby causing an underestimate of the areas of the loss peaks (which do not include the tails). The tail on the no-loss peak was chosen to give a best fit in the region between the no-loss peak and the one-surface-plasmon loss peak. The tails on the loss peaks in each spectrum were assumed to have the same peak-height-to-tail ratio. Although these choices are reasonable, it is certainly possible for errors of at least 10% to have arisen in the tail estimates. This method of tail allowance

should represent something near the maximum expected from any self-consistent analysis, so that the plasmon intensities derived after subtraction of these tails would probably tend to be systematically low if errors are present. (4) The marked discrepancies between the shapes of the experimental and theoretical curves in figure (2) for  $\theta \leq 10^\circ$  may be caused by electron refraction in crossing the surface. At XPS energies, such refraction effects become significant for electron detection angles of less than about 5-10%<sup>23</sup>. Refraction at the surface causes electrons with a given angle of propagation inside the crystal to be collected at lower angles of detection outside of the crystal. For example, an electron of 1410 eV incident on a surface barrier of 16.7 eV (the inner potential of Al<sup>30</sup>) at  $8.0^\circ$  would be detected at an angle of  $5.0^\circ$ . No allowance for refraction has been made in the calculations, but it would tend to qualitatively change the theoretical curves of Figure IV-2 so as to improve agreement with experiment. (5) The presence of sample surface roughness will also in general cause the angle of detection to be less than the average true angle of emission<sup>23,31</sup>, and would also contribute to the discrepancies noted at low angles. However, since all three sets of experimental data are in good agreement despite the differences in preparation between bulk and deposited samples, it is not obvious that surface roughness is responsible to a great degree for the differences between theory and experiment.

Figure IV-3 compares theoretical and experimental area ratios for the loss peak corresponding to the creation of one surface plasmon,  $R_{10}$ . Here, theory including both extrinsic and intrinsic effects ( $R_{10}(S)$  and

$R_{10}(F)$ ) again generally overestimates the area of the loss peak. For the higher angle range between  $30^\circ$  and  $90^\circ$  however, there is good agreement as to magnitude and general shape, particularly for the calculations of Feibelman. At lower angles of electron escape, the discrepancy between theory and experiment is much more severe, however, probably due to refraction and/or roughness effects. If only extrinsic contributions to surface plasmon excitation are considered ( $R_{10}(F,ex)$ ), the theoretical overestimate of loss intensities is even larger, presumably due to the elimination of significant interference effects. The difference noted between the  $R_{10}(F)$  and  $R_{10}(F,ex)$  curves is also qualitatively similar to analogous results for a fixed emitter depth reported recently by Bradshaw et al.<sup>14</sup>. The reason for the general overestimate of plasmon loss intensities by theory may lie in the assumption that the surface of the metal is described by a simple step-function change in electron density. The presence of this sharp potential step should lead to a very strong coupling of electrons at the surface to the surface plasmon modes. A more realistic model of the surface region may tend to reduce this strong coupling, as suggested by Penn<sup>15</sup>.

In addition to the loss peaks observed in the Al2p spectral region, it was also possible to detect loss structures associated with the O1s peak at very low oxygen coverages of  $\sim 0.15$  monolayer. Figure IV-4 shows O1s spectra at  $\theta = 90^\circ$  and  $\theta = 5^\circ$ . In the high-angle spectrum, no loss peaks are detectable on the low kinetic energy side of the peak, and the relatively flat loss spectrum is also very low in intensity. However, in the low-angle spectrum, two distinct peaks are detectable 10.1 eV and

20.8 eV from the no-loss peak. The positions of these peaks correspond very closely to the excitation of one- and two-surface plasmons by the exiting photoelectron. Based upon the Ols data, the average value of the surface plasmon energy is 10.4 eV, which is in fair agreement with the value for much cleaner surfaces of 11.0 eV. At  $\theta = 5^\circ$ , the ratios of these two loss peaks to the no-loss peak as determined by a least-squares fit are  $R_{10} = .12$  and  $R_{20} = .09$ . At higher oxygen exposures, the surface plasmon has been reported to move to lower energies, finally approaching a value of 7.9 eV characteristic of the Al/Al<sub>2</sub>O<sub>3</sub> interface<sup>32</sup>. The very small downward shift in surface plasmon energy thus indicates that it should still be approximately correct to compare the predictions of a theory based upon an unperturbed jellium-vacuum interface to the Ols experimental results. It should also be noted that a portion of the intensity of the two-surface-plasmon peak could be due to an oxide loss, which has been found at much higher oxygen exposures of  $\sim 1000$  L to be centered at 24-26 eV below the no-loss peak<sup>14</sup>. However, the oxide loss is much broader than the surface plasmon loss peak<sup>14</sup>, by contrast with the data of Figure VI-4; thus, as the position of the second peak observed in this data is also very close to  $2\hbar\omega_s$  from the no-loss peak, its assignment as predominantly a surface plasmon loss structure seems reasonable.

In Figure VI-5, theoretical intensity ratios of the one-bulk-loss peak to the no-loss peak  $R_{01}$  based on extrinsic and intrinsic calculations by Feibelman<sup>13</sup> are plotted as a function of the depth of the emitter for electrons with the Ols kinetic energy (967 eV) at normal

exit ( $\theta = 90^\circ$ ) and near grazing exit ( $\theta = 5^\circ$ ). The nearest-neighbor distance in aluminum is  $2.86 \text{ \AA}$ . Theory predicts significant bulk plasmon excitation for depths as shallow as  $1 \text{ \AA}$ , but there is no detectable bulk plasmon loss in the experimental spectrum. This suggests that the chemisorbed oxygen is situated either very near to or outside of the surface. As another indicator of the predicted relative intensities of bulk plasmon losses, Figure VI-6 shows values obtained for the single-surface-plasmon to single-bulk-plasmon ratio  $R_{10}/R_{10}$  at  $\theta = 5^\circ$ <sup>13</sup>. Comparing these results with Figure VI-4 further confirms that the emitting sites must be very near the aluminum surface, as no distinct bulk loss features are observed, corresponding to a very large value for  $R_{10}/R_{10}$ . Thus, although several prior models proposed for aluminum oxidation have involved an incorporative mechanism<sup>33,34</sup>, the present data do not indicate penetration by more than a small fraction of the nearest-neighbor distance for the coverage of  $\sim 0.15$  monolayers studied here. These results are not inconsistent, however, with recent correlations between ultraviolet photoemission data<sup>35</sup> and theoretical calculations based upon oxygen interaction with either a jellium substrate<sup>35</sup> or a 5-atom aluminum cluster<sup>36</sup>; theory and experiment are in these cases in approximate agreement for penetration distances corresponding very nearly to in-surface oxygen nuclear positions as measured relative to a charge-distributed jellium substrate.

Theoretical predictions of the  $01s$  surface plasmon relative intensities are also found to be too high. For example, including both extrinsic and intrinsic effects at  $\theta = 5^\circ$  and an emission depth of

1.0 Å yields<sup>13</sup>  $R_{10} = 1.12$  and  $R_{20} = 0.64$ , values which are approximately an order of magnitude above experiment. A large part of this discrepancy could originate in refraction or roughness effects, however, the two-surface-plasmon to one-surface-plasmon intensity ratio  $R_{10}/R_{20}$  is, on the other hand, approximately predicted by theory: at  $\theta = 5^\circ$  and an emission depth of 1.0 Å this ratio is 0.564, a value in reasonable agreement with the experimental ratio of 0.75. In such surface-plasmon ratios, a certain amount of cancellation of errors due to refraction, roughness, and the general overestimate of the surface-plasmon coupling strength would be expected to occur.

Our overall conclusions concerning the 01s loss structure are thus very close to those of Bradshaw et al.<sup>14</sup>, although one discrepancy noted is that  $R_{10}$  at  $5^\circ$  is found to be .12 while they report a higher value of .18 at the higher angle of  $\theta = 10^\circ$ . The source of this discrepancy is not clear although they have used a single-crystal specimen which may have had different surface roughness characteristics, and the fitting of relatively small peaks on an ill-defined background is in either analysis strongly dependent on the choice of background. A further experimental difference is that the oxygen-containing absorbate in the present study was primarily residual  $H_2O$ , rather than  $O_2$  as in the other measurements.

## 5. Conclusions

Angular-dependent studies of the XPS plasmon loss spectra of aluminum have thus provided a useful means of studying bulk- and surface-loss mechanisms. Comparisons of experimental and theoretical

results for Al<sub>2</sub>p loss spectra yield approximate agreement for angles  $\geq 30^\circ$ , and indicate that there is some intrinsic character in the plasmon loss mechanism in aluminum, although the theory utilized here may overestimate this contribution; this conclusion is thus consistent with a recent analysis of fixed-angle aluminum data by Penn<sup>15</sup>. Theory also significantly overestimates intensities due to surface plasmon creation, especially at low angles of electron escape. This may be due to electron refraction or surface roughness, or could be a result of the sharp-surface assumption used in the calculations. Angle-resolved loss spectra have also been shown to be capable of providing information concerning the depth of penetration of chemisorbed species. Analysis of the O<sub>1s</sub> loss spectrum of oxygen adsorbed onto aluminum indicates that there is no significant incorporation of the oxygen into the aluminum at very low oxygen coverages.

REFERENCES  
SECTION VI.

1. See for example: N. V. Smith and W. E. Spicer, Phys. Rev. Lett. 23, 769 (1969); and I. Lindau, H. Löfgren, and L. Walldén, Phys. Lett. 36A, 293 (1971).
2. See for example: L. H. Jenkins and M. F. Chung, Surf. Sci. 28, 409 (1971); and A. Barrie and F. J. Street, J. Electron Spectrosc. 7, 1 (1975).
3. See for example: Y. Baer and G. Busch, Phys. Rev. Letters 30, 280 (1973); S. A. Flodstrom, R. Z. Bachrach, R. S. Bauer, J. C. McMenamin and S. B. M. Hagström, to appear in J. Vac. Sci. Tech., Proc. of Chicago Meeting, 1976.
4. R. A. Pollak, L. Ley, F. R. McFeely, S. P. Kowalczyk and D. A. Shirley, J. Electron Spectrosc. 3, 381 (1974).
5. R. J. Baird and C. S. Fadley, results discussed in C. S. Fadley, Prog. in Solid State Chem. 11, 265 (1976) and D. A. Shirley et al., private communication.
6. C. N. Berglund and W. E. Spicer, Phys. Rev. 136, 1030 (1964).
7. P. J. Feibelman, Phys. Rev. B7, 2305 (1973).
8. P. J. Feibelman, Surf. Sci. 36, 558 (1973).
9. D. C. Langreth, Phys. Rev. Lett. 26, 1229 (1971).
10. J. J. Chang and D. C. Langreth, Phys. Rev. B5, 3512 (1972).
11. J. J. Chang and D. C. Langreth, Phys. Rev. B8, 4638 (1973).
12. M. Šunjić, D. Šokćević, and A. Lucas, J. Electron Spectrosc. 5, 963 (1974).

13. P. J. Feibelman, private communication.
14. A. J. Bradshaw and J. C. Fuggle in Photoemission from Surfaces, Proceedings of a conference in Noordwijk, Holland, September, 1976, B. Feuerbacher, R. F. Willis, and B. Fitton, Eds.
15. D. R. Penn, private communication.
16. W. J. Pardee, et al., Phys Rev. B 11, 3614 (1975).
17. J. C. Fuggle, D. J. Fabian and L. M. Watson, J. Electron Spectrosc. 9, 99 (1976).
18. R. J. Baird and C. S. Fadley in Photoemission from Surfaces, Proceedings of a conference in Noordwijk, Holland, September, 1976. Note that the relative intensity of the 01s single-surface-plasmon loss satellite at  $\theta = 5^\circ$  is erroneously reported in this paper as 0.40; the correct value is approximately four times lower and is 0.12.
19. M. Šunjić and D. Šokčević, Sol. St. Comm. 15, 165 (1974).
20. D. Šokčević and M. Šunjić, Sol. St. Comm. 15, 1703 (1974).
21. M. Šunjić, private communication.
22. R. J. Baird and C. S. Fadley, to appear in J. Electron Spectrosc.
23. C. S. Fadley, R. J. Baird, W. Siekhaus, T. Novakov, and S. Å. L. Bergström, J. Electron Spectrosc. 4, 93 (1974), and C. S. Fadley, Prog. in Solid State Chem. 11, 265 (1976).
24. R. J. Baird, unpublished results.
25. P. H. Holloway, J. Electron Spectroscopy 7, 215 (1975).
26. C. S. Fadley, Ph.D. Thesis, University of California at Berkeley, 1970 (Lawrence Berkeley Laboratory, Report UCRL-19535 (1970)).

27. P. H. Citrin, G. K. Wertheim, and Y. Baer, Phys. Rev. Lett. 35, 885 (1975).
28. H. Kanter, Phys. Rev. B 1, 2357 (1970).
29. J. C. Tracy, Crit. Rev. Solid State Sci. 4, 381 (1974).
30. C. B. Duke, in Electron Emission Spectroscopy, W. Dekeyser et al., Eds., Reidel, Dordrecht, Holland, 1973.
31. R. J. Baird, C. S. Fadley, S. Kawamoto, and M. Mehta, Chem. Phys. Lett. 34, 49 (1975).
32. E. A. Stern and R. A. Ferrell, Phys. Rev. 120 130 (1960).
33. W. H. Krueger and S. R. Pollack, Surf. Sci. 30, 263 (1972).
34. V. J. Agarwala and T. Fort, Surf. Sci. 45, 470 (1974).
35. K. Y. Yu et al., Phys. Rev. B 14, 1446 (1976).
36. J. Harris and G. S. Painter, Phys. Rev. Letters 36, 151 (1976).

Figure VI-1 - Al<sub>2</sub>p spectra at three angles showing the total fitted curve and all component peaks. The no-loss peak occurs at a binding energy of 73.1 eV. The loss peaks are labelled, with S = surface plasmon and B = bulk plasmon. In the expanded-scale inserts, the loss peaks are shown on the inelastic tail of the no-loss peak for clarity.

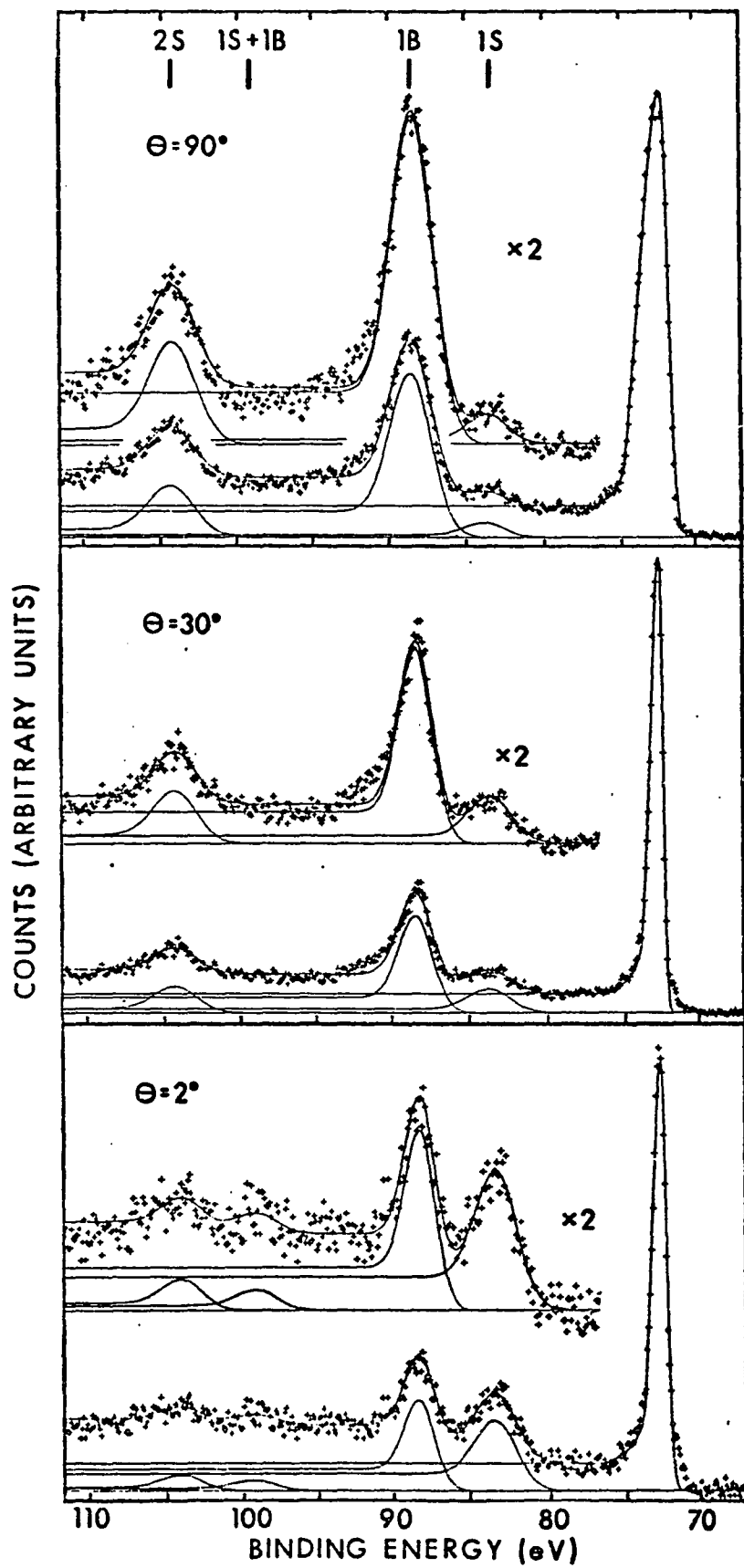


Figure VI-2 - Theoretical and experimental Al2p one-bulk-loss and two-bulk-loss relative intensities. The open data points are the experimental values of  $R_{01}$ ; the filled points are the experimental values of  $R_{02}$ . The circles and triangles are data from deposited films; the squares represent data from a bulk sample. The solid curves  $R_{on}(S)$  are the results of calculations by Šunjić<sup>21</sup> including both extrinsic and intrinsic effects. The dashed curves  $R_{on}(F)$  are analogous results due to Feibelman<sup>13</sup> and the dotted curves  $R_{on}(F,ex)$  represent calculations by Feibelman including only extrinsic effects.

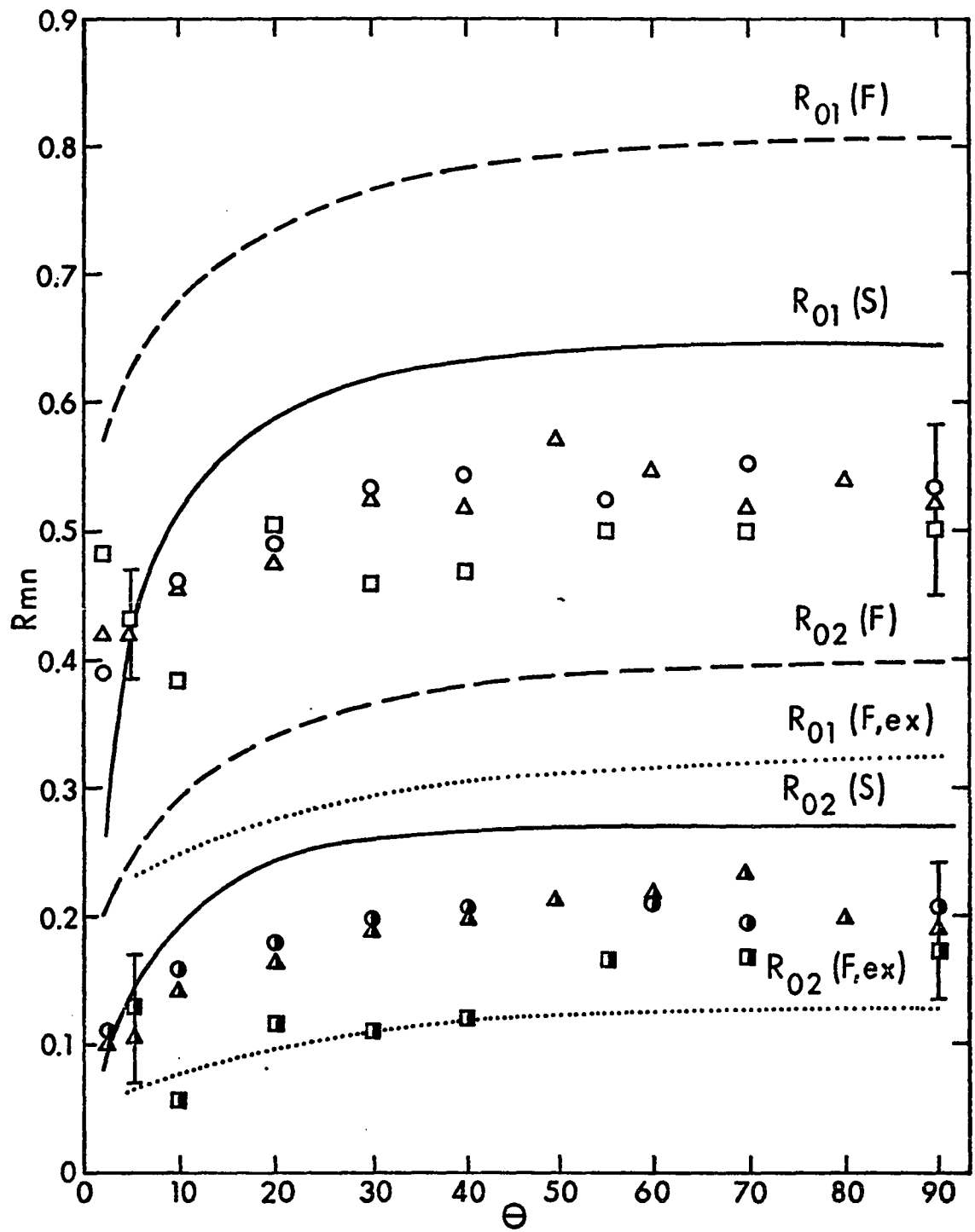


Figure VI-3 - Theoretical and experimental Al<sub>2</sub>p one-surface-plasmon relative intensities as a function of angle. The notation is the same as in Figure 2.

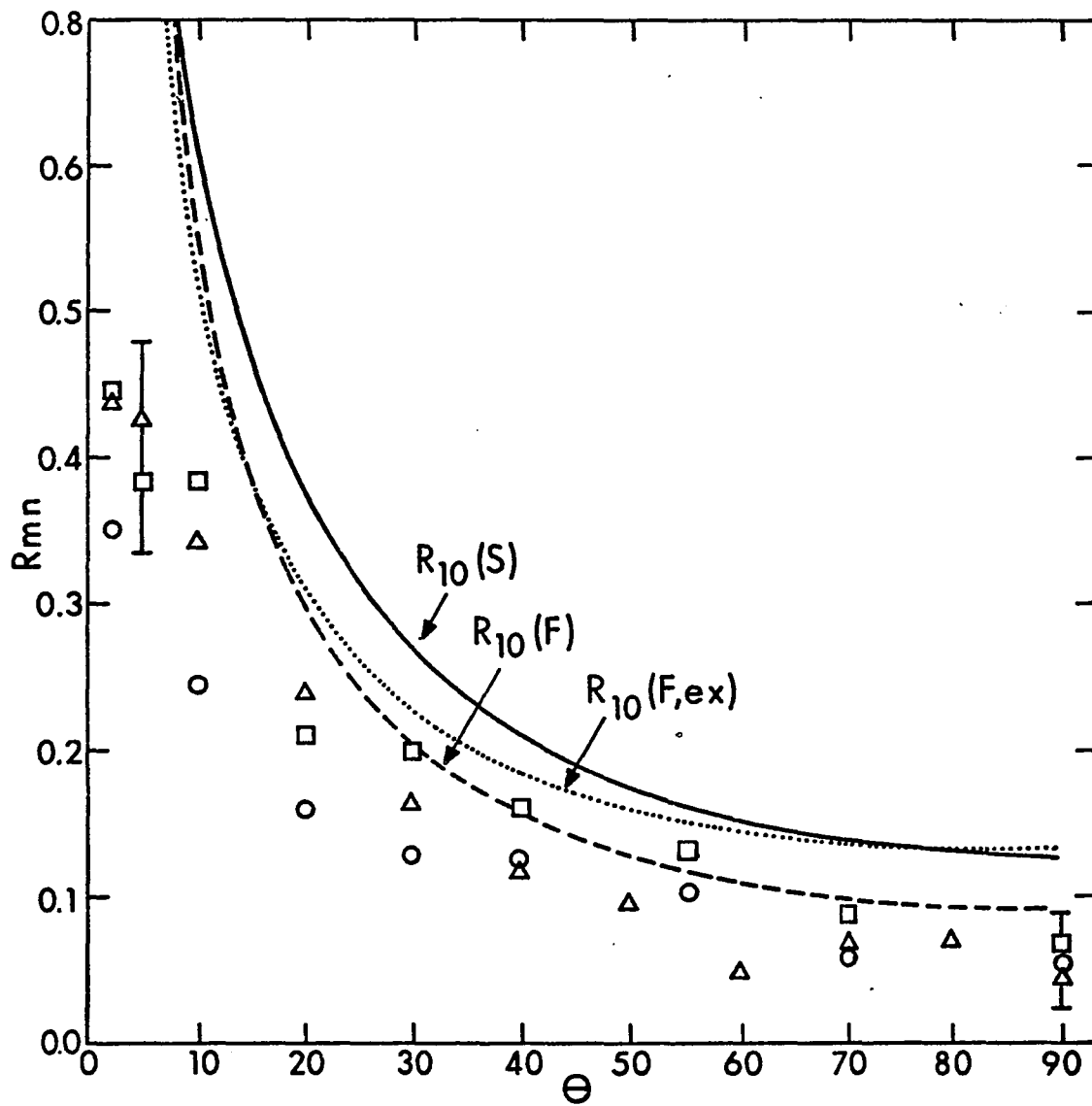


Figure IV-4 - O1s spectra at two angles obtained from oxygen adsorbed on polycrystalline aluminum at a coverage of 0.15 monolayer. The surface-plasmon loss peaks are evident in the low-angle (grazing exit) spectrum while the high angle spectrum shows a flat, featureless loss spectrum.

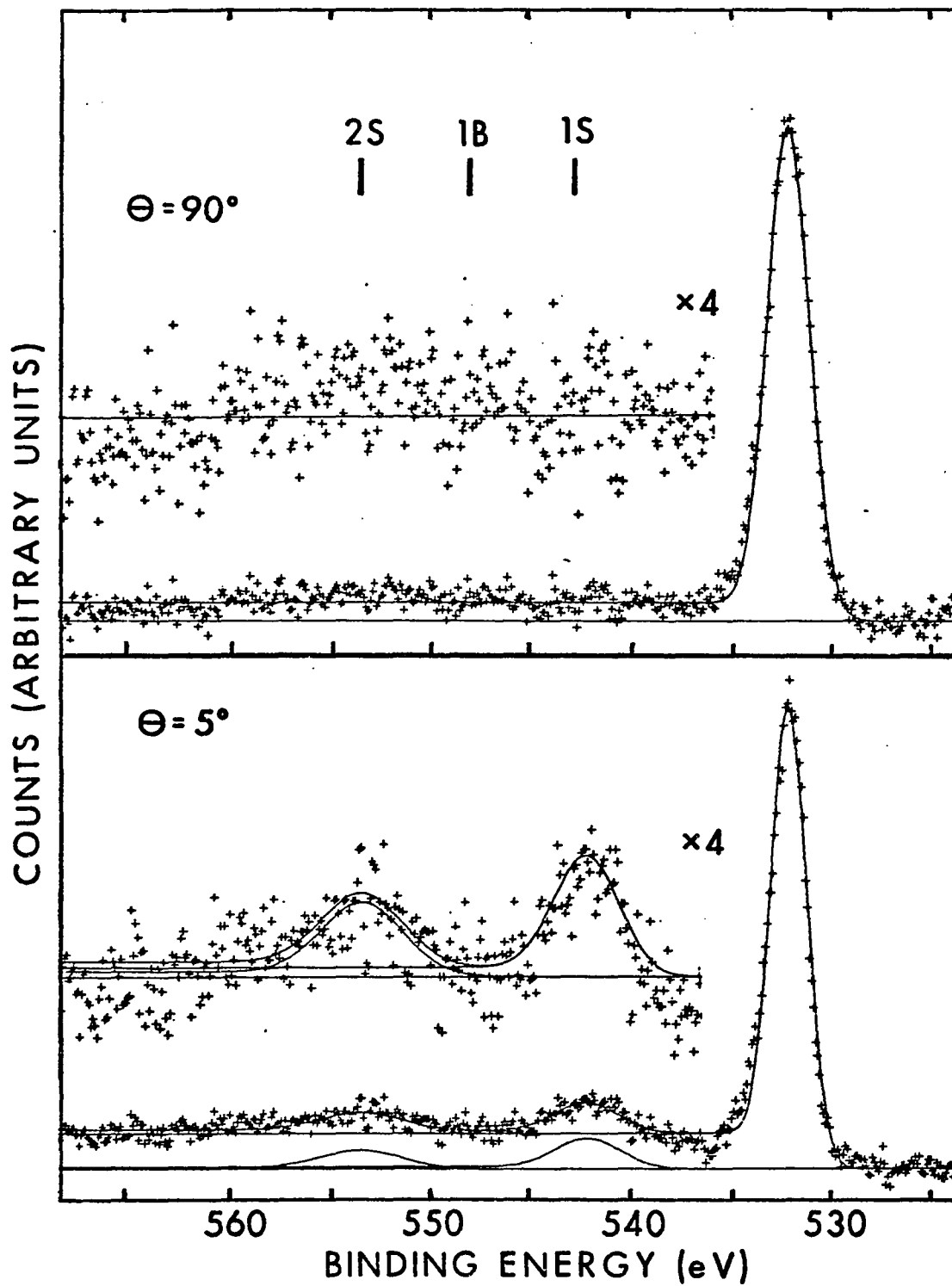


Figure VI-5 - Theoretical O1s one-bulk-plasmon relative intensities for normal emission ( $\theta = 90^\circ$ ) and near-grazing emission ( $\theta = 5^\circ$ ) as a function of oxygen depth below the surface. These values are based upon calculations by Feibelman<sup>13</sup> including both extrinsic and intrinsic effects.

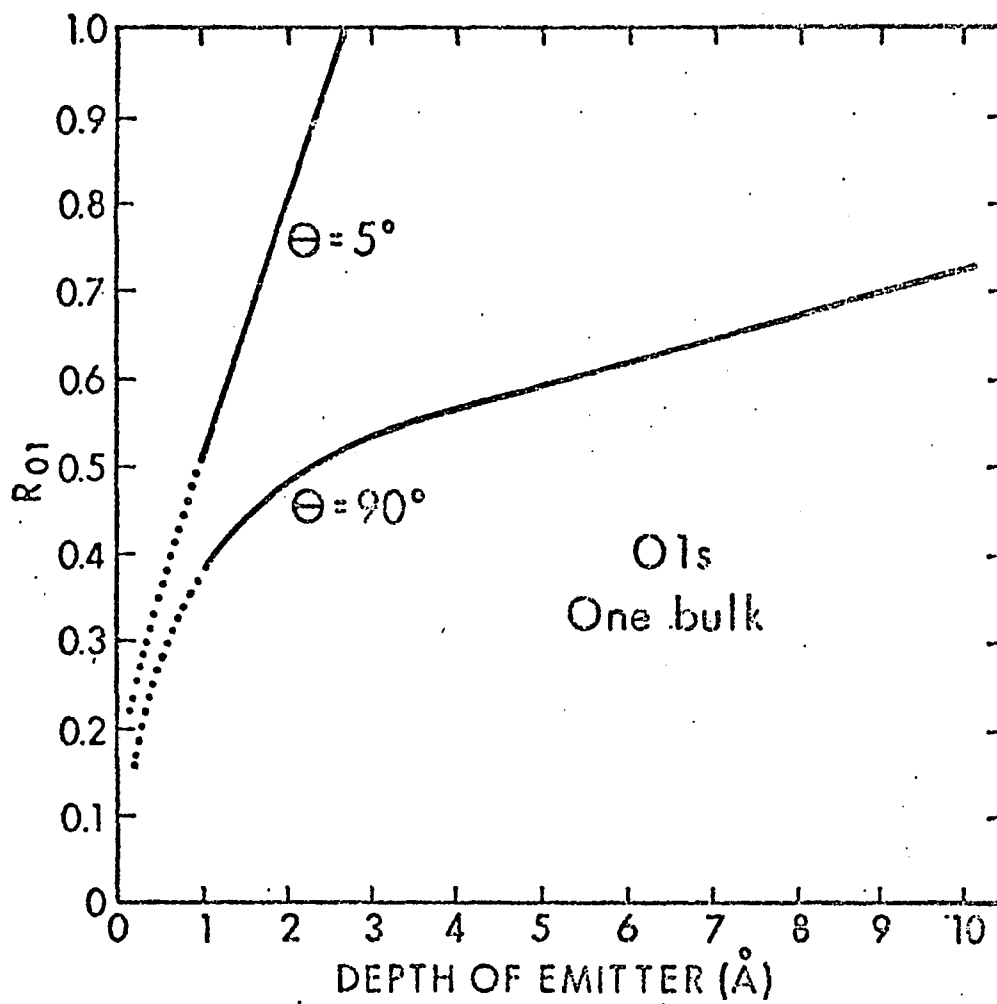
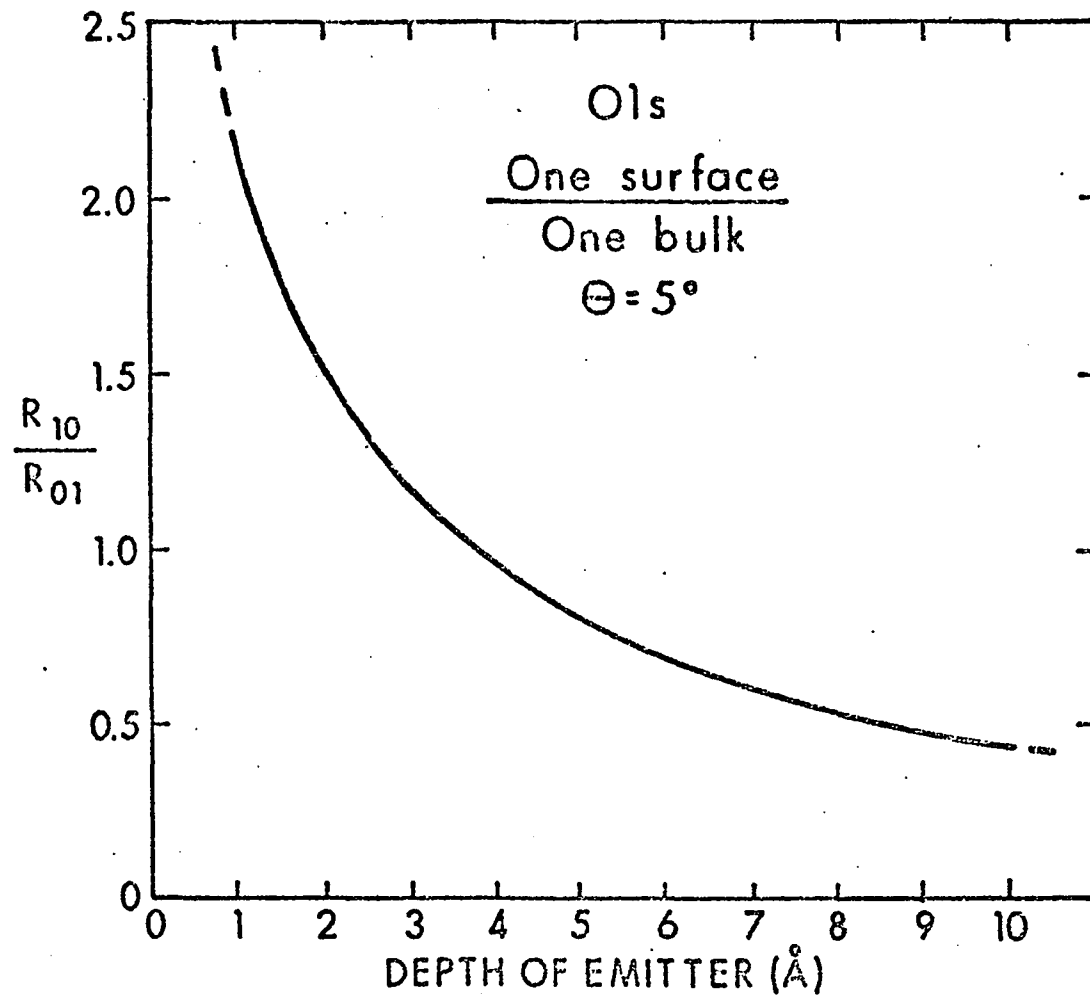


Figure IV-6 - Theoretical predictions for the O1s one-surface-plasmon to one-bulk-plasmon area ratio at  $\theta = 5^\circ$  as a function of oxygen depth below the surface. The calculations are due to Feibelman<sup>13</sup> and include both extrinsic and intrinsic plasmon creation.



VII. ANGULAR-DEPENDENT X-RAY-PHOTOELECTRON PEAK INTENSITIES  
FROM SINGLE-CRYSTAL GOLD †

1. Introduction

Pronounced fine structure has been observed previously in the angular distributions of core- and valence-x-ray-photoelectron (XPS) peak intensities from single crystals of NaCl<sup>1</sup>, Au<sup>2-4</sup>, KCl<sup>5</sup>, and Si<sup>4,6,7</sup>. These effects are associated with electron diffraction phenomena, and lead to enhanced emission along certain directions fixed with respect to the crystal axes. However, the data reported in prior studies have been limited to one<sup>1,4,5,6</sup>, or at most a few<sup>2</sup>, distinct polar-angle scans for a given crystal, and relatively large angular intervals of  $\sim 5^\circ$  have also been used in some aspects of these investigations<sup>2</sup>. In addition, although previous discussions<sup>1,2,4,5,8</sup> have implied the connection of such phenomena with the Kikuchi bands observed, for example, in low energy electron diffraction (LEED) experiments carried out at kinetic energies  $\gtrsim 300$  eV<sup>9</sup>, no detailed comparisons of experimental intensities with the well-established systematics of these bands have been made. In this paper, we report the most extensive measurement of this type performed to date, including polar plots of core- and valence-angular distributions and the first detailed intensity contour plot over essentially the full  $2\pi$  solid angle. The intensity contours are furthermore compared with the qualitative expectation of Kikuchi-band theory. The relationship of such effects to the strong angular

† Based on a paper "Angular-Dependent X-ray-Photoelectron Peak Intensities from Single-Crystal Gold", R. J. Baird, C. S. Fadley, and L. F. Wagner, to appear in Phys. Rev. B.

dependence noted previously in the relative intensities of various features in XPS valence spectra from single crystals<sup>3,4</sup>, is also discussed qualitatively.

## 2. Experimental Procedure

Measurements were performed on a Hewlett-Packard 5950A spectrometer which had been modified to permit computer-controlled in situ two-axis rotation of the specimen<sup>4,10</sup>. A schematic drawing of the experimental geometry is shown in Figure VII-1. Both the polar angle  $\theta$  and the azimuthal angle  $\phi$  associated with the electron emission direction from the surface were varied. ( $\theta$  is here defined such that  $90^\circ$  corresponds to emission perpendicular to the surface.) An accuracy of  $\pm 1^\circ$  was obtained in both angles. The solid angle accepted by the analyzer has been determined by electron trajectory calculations to be a cone of  $3.5^\circ$  half-angle<sup>10</sup>. The angle between the x-ray-incidence- and electron-exit-directions was fixed such that  $\alpha = 72^\circ$  in Figure VII-1, and polar rotations were performed about an axis perpendicular to the plane containing these directions. Azimuthal rotations were about the surface normal. Monochromatized  $AlK_\alpha$  radiation was used for excitation. Peak intensities from this spectrometer have previously been shown to vary significantly with polar angle according to a well-defined instrument response function<sup>4,10,11</sup>. If normalized to  $\theta = 90^\circ$ , this smoothly-varying function has values of: 1.00 at  $90^\circ$ , 0.74 at  $70^\circ$ , 0.47 at  $50^\circ$ , 0.27 at  $30^\circ$ , 0.09 at  $10^\circ$ , and zero at  $0^\circ$ .

A gold single crystal was mechanically polished and etched with aqua regia to remove surface disorder. The surface normal was oriented

$8 \pm 1^\circ$  away from  $[001]$  along a direction toward  $[\bar{1}\bar{1}1]$ . (This orientation permitted the determination of valence-spectrum fine structure along several  $\langle 100 \rangle$  and  $\langle 110 \rangle$  directions<sup>3,4</sup> by avoiding grazing exit angles for which the response function is zero.) All measurements in the photoelectron spectrometer were performed at 25–28°C and at pressures of  $2-4 \times 10^{-9}$  torr. Carbon was the only surface contaminant observed, with the Cls/Au4f intensity ratio being 0.03–0.04 and thus indicative of a coverage of 1–2 monolayers<sup>12</sup>. An amorphous carbon overlayer was also suggested by the structureless Cls angular distributions observed. Prior studies<sup>2,4,6</sup> indicate that such an overlayer should have a negligible smearing effect on the gold photoelectron angular distributions. The surface order of the gold crystal was verified by LEED experiments in a separate system; these gave spot patterns characteristic of the (001) surface after only light ion bombardment to remove the carbon present. Subsequent annealing did not change the LEED results.

The mean kinetic energies and de Broglie wavelengths associated with the gold peaks studies are: Au4d<sub>3/2,5/2</sub> – 1140 eV, 0.363 Å; Au4f<sub>5/2,7/2</sub> – 1397 eV, 0.328 Å; and Au valence – 1471–1481 eV, 0.319–0.318 Å. Peak intensities were determined as integrated areas above linear backgrounds, thus eliminating any effects due to angle-dependent resolution changes in the spectrometer<sup>10</sup>. The XPS valence-peak intensities for gold are well known to be associated primarily with the 5d bands.

Polar-angle scans were made for the 4d-, 4f-, and valence-spectral regions along several planes. Also, the 4f spectral region was singled out for more detailed study and intensity determinations were made over

the full solid angle on a grid with angular intervals of  $\Delta\theta = 2.7^\circ$  and  $\Delta\phi = 3.0$ . The data were accumulated in two overlapping  $\phi$  scans of  $210^\circ$  each, between which the specimen was removed from the spectrometer for manual rotation by  $180^\circ$ . The approximately 4000 data points so obtained were then used to derive contours of equal intensity via a two-dimensional Laplacian interpolation scheme. Minimal data smoothing was involved in generating these contours.

### 3. Results and Discussion

#### A. Energy-Integrated Intensities and Kikuchi Effects

Angular distributions for the 4d-, 4f-, and valence-peaks are shown in Figure VII-2 for two separate polar-angle scans. The angle interval used was  $2.7^\circ$ . Curves A correspond to scanning the emission direction approximately in a (110) plane containing the [001] and [111] directions and Curves B to a scan approximately in a (100) plane containing the [001] and [011] directions<sup>13</sup>. All curves are modulated by the instrument response function as quoted. Significant features common to the sets of curves are labelled, with peaks 5 and 10 corresponding to emission along [001]. Although the curves for the two different polar scans are markedly different in shape, it is clear from this data that the angular distributions for all three spectral regions in a given scan are essentially identical. Features 1-10 have very nearly the same positions, relative intensities, and widths for all three curves. This agreement includes very narrow structures such as 4, 7, and 9, which have total base widths of only  $\sim 5^\circ$ . Such correspondence between angular distributions is consistent with previous data of lower accuracy and resolution

obtained by Fadley and Bergstrom<sup>2</sup>. Such results thus suggest scattering effects that are dominated by the final-state character of the photoelectron, as the de Broglie wavelengths associated with the 4d-, 4f-, and valence-peaks differ by at most 13%. Initial-state properties such as the degree of localization of the orbital from which photoemission occurs thus do not appear to play a major role in determining these angular distributions of integrated peak intensity, even though we have also previously observed<sup>3,4</sup> that the relative intensities of various components within the gold valence-band spectrum change  $\sim \pm 15\%$  for different electron emission directions in the crystal. The relationship of such valence-spectrum relative intensity changes to total-intensity angular distributions is discussed in the next section.

The 4f intensity contour results are presented in stereographic projection in Figure VII-3, in which various low-index directions and planes are labelled. (The location of the [001] direction is obvious, and the surface normal is oriented  $8^\circ$  away from it towards  $[\bar{1}\bar{1}1]$ .) The dotted lines separate data obtained in the two different  $\theta$  scans. Due to slight instrumental intensity drifts and possible small changes in surface contaminant levels during external rotation between  $\phi$  scans, the two sets of data show slightly different average intensities; these differences are never greater than 25% between points with corresponding symmetry, however. No correction has been made for the instrument response function, so intensities generally decrease as the polar orientation moves away from the surface normal. An additional intensity decrease occurs toward low  $\theta$  because of attenuation in the thin contami-

nant overlayer<sup>11,12</sup>, and it is because of the difficulty of accurately allowing for this effect that no attempt was made to correct the data by dividing out the response function.

The contours of Figure VII-3 clearly exhibit the fourfold symmetry of the (001) surface, with regions of highest intensity occurring along various low-index directions (or equivalently, along the intersections of several low-index planes). In particular, intensity maxima are found along the [001],  $\langle 110 \rangle$ , and  $\langle 211 \rangle$  directions and also lie very close to the  $\langle 221 \rangle$ ,  $\langle 310 \rangle$ , and  $\langle 311 \rangle$  directions<sup>13</sup>. The outer, approximately circular, contours (such as those labelled "10") also exhibit symmetric structures that are suggestive of bands of higher intensity lying along low index planes (as, for example,  $(\bar{1}\bar{1}1)$ ,  $(2\bar{2}0)$ , and  $(111)$ ). By comparing Figures VII-2 and VII-3 it can also be seen that several peaks occur very close to certain low-index directions: peaks 1 lie along  $[111]$ , peaks 2 along  $[112]$ , and peaks 6 along  $[011]$ .

An explanation of these effects in terms of the known phenomenology of Kikuchi bands<sup>8,9</sup> requires that each set of planes  $hkl$  has associated with it a band of excess intensity oriented parallel to the planes and possessing an angular width of approximately  $2\theta_{hkl}$ , with  $\theta_{hkl}$  being the Bragg angle for electron diffraction from the planes. These bands may be bordered by deficiency regions of much smaller angular widths, and may also exhibit intensity minima at their centers<sup>8,9</sup>. For the three lowest-index planes in the fcc gold crystal from which diffraction is allowed, the Bragg angles for 4f photoelectrons are:  $111 - 4.0^\circ$ ,  $200 - 4.6^\circ$ , and  $220 - 6.5^\circ$ . As a simple test of the qualitative

applicability of this model for explaining XPS angular distributions, we show in Figure VII-4 a (001) stereographic projection on which has been placed shaded bands of uniform intensity with  $2\theta_{hkl}$  widths appropriate to the low-index planes mentioned. The positions and approximate widths of the experimental maxima along the [001],  $\langle 110 \rangle$ , and  $\langle 211 \rangle$  directions are well predicted by this model (which implicitly neglects any changes in intensity due to purely instrumental effects). The full widths at half-maximum intensity of certain peaks in the polar angular distribution curves also have magnitudes comparable to the one or more  $2\theta_{hkl}$  values that Figures VII-3 and VII-4 predict to be involved, especially if effects due to instrumental angular broadening are considered. For example, the widths of several prominent peaks have been derived from Figure VII-2 relative to a smooth-curve background and these are given together with the direction along which each peak maximum occurs as follows: peaks 1 -  $6.0^\circ$ , [111]; peaks 5 -  $6.8^\circ$  [001]; peaks 6 -  $7.6^\circ$ , [011]; and peaks 10 -  $6.0^\circ$ , [001]. The structures observed in the outer contours of Figure VII-e such as those with value 10 are also in agreement with the qualitative predictions of Figure VII-4 associated with the three lowest-index planes.

The intensity maxima observed near the  $\langle 221 \rangle$ ,  $\langle 310 \rangle$ , and  $\langle 311 \rangle$  directions are, on the other hand, not simply connected with the bands expected for the three lowest-index sets of planes. As judged by decreasing interplanar spacing (or equivalently,  $(h^2 + k^2 + l^2)^{-1/2}$ ), the next set which might be involved is  $\{311\}$ , with  $\theta_{311} = 7.7^\circ$ . As an indication of the positions of the centers of the Kikuchi bands associated

with these planes, dotted lines are shown in the lower half of Figure VII-4. (The pattern in the upper half is obtained simply by reflection of that in the lower half.) The  $\{311\}$  bands are thus predicted to intersect and thus to tend to produce intensity maxima at eight points in a star-like pattern surrounding and rather close to  $[001]$ . The four intersections along  $\{200\}$  planes should occur along  $\langle 310 \rangle$  directions, or at  $18.4^\circ$  from  $[001]$ ; this value agrees very well with the average position of the four corresponding experimental peaks in Figure VII-3, which is found to be  $19.1^\circ$  from  $[001]$ . (These peaks correspond to those numbered 8 in Figure 2.) The four intersections along  $\{220\}$  planes are predicted to occur at  $19.5^\circ$  from  $[001]$ , again in very good agreement with the mean experimental separation of  $19.7^\circ$ . (These experimental peaks are noted as 3 in Figure VII-2). Additional band intersections involving  $\{311\}$  are also expected to be found near, but not exactly along, the  $\langle 221 \rangle$  directions, thereby at least partially explaining the intensity maxima observed very close to  $\langle 211 \rangle$ . Thus, by including only planes for which  $h^2 + k^2 + l^2 \leq 11$ , it is possible to explain most of the major features noted in Figures VII-2 and VII-3.

If, in addition, the effects of bands associated with the next two higher-index planes  $\{331\}$  ( $\theta_{331} = 10.1^\circ$ ) and  $\{420\}$  ( $\theta_{420} = 10.4^\circ$ ) are considered, it is furthermore predicted that intersections and thus maxima should occur directly along  $\langle 221 \rangle$ , as well as at positions near  $\langle 211 \rangle$  along the  $\{111\}$  bands. These predictions thus further account for the maxima noted along  $\langle 221 \rangle$  in Figure VII-3, as well as for the elongation of the intensity peaks observed near  $\langle 211 \rangle$  along the direction

of the  $\{111\}$  planes. Qualitatively, there is thus very good agreement between experiment and the approximate systematics expected for Kikuchi bands.

Detailed theoretical calculations of such single-crystal effects on XPS intensities have not been carried out previously, although McRae<sup>8</sup> has discussed a phenomenological model for them. A more accurate description of these effects will no doubt involve the inclusion of multiple-scattering effects such as is done in current analyses of either LEED data<sup>14</sup> or extended x-ray absorption edge fine structure (EXAFS) experiments<sup>15</sup>. In particular, XPS emission from a localized core level is identical to the basic transition occurring in EXAFS, although the final state energy in a typical XPS experiment is somewhat higher than those of most interest in EXAFS.

#### B. Angular-Dependent Valence Fine Structure

As a final point, we comment qualitatively on the possible relationships existing between two separate effects noted in angular-dependent XPS studies of single-crystal Au: (1) the variation of energy-integrated valence-spectrum intensities with angle, as discussed in the previous section (cf. Figure 2), and (2) the angular dependence of the relative intensities and positions of various individual features in the d-band-dominated valence spectrum, as observed previously<sup>3,4,16</sup>. Figure VII-5 presents Au valence spectra obtained in this study at several closely-spaced angles along a given polar scan, and pronounced changes in the fine structure are evident.

A complete understanding of both of these effects within the context of a single model will no doubt involve a one-step description of the photoemission process that includes the presence of the surface, as well as both bulk- and surface-secondary scattering phenomena in the final state. Although models of this type have been discussed previously<sup>17</sup>, no detailed numerical calculations relevant to the present case have been carried out. At a somewhat simpler level very close to the often used three-step model of photoemission<sup>18</sup>, it is possible, however, to self-consistently explain the observed systematics of the two effects.

The angular-dependent valence-spectrum fine structure for Au has been successfully analyzed in terms of a direct-transition model<sup>3,4</sup> that is closely related to that used in prior angular-dependent ultraviolet photoemission (UPS) studies<sup>17,19</sup>. This model has been discussed in detail elsewhere<sup>3,4</sup>, but, in brief review, it yields a wave-vector selection rule of the form  $\vec{k}^i + \vec{g} + \vec{k}_{h\nu} = \vec{k}^f$ , in which  $\vec{k}^i$  is the initial state wave vector in a reduced-zone representation,  $\vec{g}$  is a reciprocal lattice vector,  $\vec{k}_{h\nu}$  is the (non-negligible) photon wave vector, and  $\vec{k}^f$  is the photoelectron wave vector. The strength of each direct transition will be proportional to the square of a matrix element between the initial- and final-states. A free-electron  $\vec{k}^f$  lying in the finite observation cone of the spectrometer, and a knowledge of the initial-state band structure  $E^i(\vec{k}^i)$  then specifies the allowed distribution of final photoelectron energies. If the matrix elements associated with the various direct transitions are assumed to be approximately constant, a direct prediction of angular-dependent valence spectra can

be made in this way. Good agreement is found between such calculations and XPS valence data for both Au<sup>3</sup> and Cu<sup>20</sup>. The additional effect of angular-dependent matrix elements has also been found to yield theoretical results in agreement with some aspects of angular-dependent XPS valence spectra from Au and Ag<sup>16</sup>.

The question thus arises as to whether the simple free-electron final state assumed in the direct-transition model is consistent with the more complex final state expected as a result of the multiple scattering effects producing Kikuchi phenomena. The XPS data obtained to date for these two types of effects can be explained if it is assumed that the x-ray photoemission process approximately separates into an initial direct transition ( $\vec{k}^i \rightarrow \vec{k}^f$ ) followed by secondary scattering ( $\vec{k}^f \rightarrow \vec{k}^{f'}$ ) that is dependent primarily on  $\vec{k}^f$ <sup>21</sup>. Secondary scattering would thus act to mix other plane waves into the final state description, so as to produce, for example, the secondary diffraction cones discussed by Mahan<sup>17</sup>, as well as Kikuchi-like effects. If constant matrix elements are further assumed, then the energy-integrated valence intensity before secondary scattering from noble metals with a filled set of d bands below the Fermi energy is predicted to be very nearly constant with angle. This is because the d bands contribute most of the XPS spectral intensity and all observed  $\vec{k}^f$  values can be projected back via suitable choices of  $\vec{g}$ 's to yield  $\vec{k}^{f'}$ 's associated with occupied initial states in each d band. Such a constant intensity with angle before secondary scattering is thus equivalent to the situation expected for core-level emission. (Note that the angle  $\alpha$  in Figure VII-1

is assumed to be constant, and so is not involved in the angular dependence of either core- or valence-intensities.) Inasmuch as the magnitude of  $\vec{k}^f$  is very nearly the same for all valence levels and high-lying core levels, it would thus further be expected that secondary scattering would tend to modulate the intensities at all points within the spectra from such levels by approximately the same factor at a given angle without, for example, introducing new structure in the valence spectra. This prediction is thus consistent with the essentially identical energy-integrated 4d-, 4f-, and valence-angular distributions shown in Figure VII-2.

Even in matrix-element anisotropies are a significant factor in producing valence fine-structure changes with angle, it is also possible to use the same two-step model to explain the observed phenomena, provided that a tight-binding description of the noble-metal d bands neglecting s, p hybridization is adopted. (Such a model has, for example, been used previously in deriving possible matrix-element effects<sup>16</sup>.) Such a description would suggest that the energy-integrated intensity over all d bands should have a single-crystal angular distribution very close to that from any filled high-lying core subshell, as is found to be the case. That is, in integrating intensities over all d bands for a given emission direction, the net result will involve summations over full sets of  $m_l$  values analogous to those producing core level intensities.

Although this model is no doubt somewhat oversimplified in its two-step separation, it is consistent with the available data, and may

serve as a useful first-order approximation in subsequent experimental and theoretical studies of such effects.

#### 4. Conclusions

The overall systematics of angular distributions of energy-integrated XPS intensities from gold 4d-, 4f-, and valence-levels are qualitatively very well described in terms of Kikuchi-band effects that are primarily controlled by the final-state character of the process. A plausible relationship between such angular distributions and the angular-dependent changes noted previously in XPS valence-spectrum fine structure has also been discussed. More quantitative experimental and theoretical studies will be necessary to fully characterize these effects, including theoretical calculations utilizing dynamical diffraction theory. A detailed understanding of such phenomena is essential for the quantitative interpretation of XPS data from any single crystal specimen.

REFERENCES  
SECTION VII.

1. K. Siegbahn, U. Gelius, H. Siegbahn, and E. Olsen, Phys. Lett. 32A, 221 (1970) and Physica Scripta 1, 272 (1970).
2. C. S. Fadley and S. A. L. Bergström, Phys. Lett. 35A, 375 (1971), and in Electron Spectroscopy, D. A. Shirley, Ed. (North Holland, Amsterdam, 1972) p. 233.
3. R. J. Baird, C. S. Fadley, and L. F. Wagner, in comments by C. S. Fadley appearing in Faraday Discussion No. 60 (1975), and Phys. Rev. Lett. 37, 111 (1976).
4. C. S. Fadley, in Progress in Solid State Chemistry, G. A. Samorjai and J. O. McCaldin, Eds. (Pergamon Press, New York, 1976) Volume 11, page 265.
5. J. Brunner and H. Zogg, private communication, and H. Zogg, Ph.D. thesis, Eidgenössische Technische Hochschule, Zürich, 1974.
6. J. M. Hill, D. G. Royce, C. S. Fadley, and F. J. Grunthaner, Chem. Phys. Letters, in press.
7. N. E. Erickson, private communication.
8. E. G. McRae, Surf. Sci. 44, 321 (1974) and references therein.
9. R. Baudoing, R. M. Stern, and H. Taub, Surf, Sci. 11, 225 (1968) and references therein.
10. R. J. Baird and C. S. Fadley, paper presented at the Northwest Regional Meeting of the American Chemical Society, Honolulu, June, 1975, and J. Electron Spectrosc., in press.

11. C. S. Fadley, R. J. Baird, W. Siekhaus, T. Novakov and S. Å. L. Bergstrom, *J. Elect. Spect.* 4, 93 (1974).
12. M. Mehta and C. S. Fadley, *Phys. Lett.* 55A, 59 (1975).
13. We have throughout used the standard notation for directions and planes: ( ) = a definite plane, { } = a set of symmetry-related planes, [ ] = a definite direction, and < > = a set of symmetry-related directions.
14. See, for example, C. B. Duke, *Jap. J. Appl. Phys., Suppl.* 2, Pt. 2, 641 (1974); J. B. Pendry, Low Energy Electron Diffraction (Academic Press, London, 1974); and references therein.
15. E. A. Stern, *Phys. Rev.* B10, 3027 (1974); and C. A. Ashley and S. Doniach, *Phys. Rev.* B11, 1279 (1975).
16. F. R. McFeely, J. Stöhr, G. Apai, P. S. Wehner, and D. A. Shirtly, *Phys. Rev. B*, to appear, and K. F. Berggren and F. Martino, private communication.
17. G. D. Mahan, *Phys. Rev.* B2, 4334 (1970); W. L. Schaich and N. W. Ashcroft, *Phys. Rev.* B3, 2452 (1970); and P. J. Feibelman and D. E. Eastman, *Phys. Rev.* B10, 4932 (1974).
18. C. N. Berglund and W. E. Spicer, *Phys. Rev.* 136, A1030, A1044 (1964).
19. P. O. Nilsson and L. Ilver, *Solid State Comm.* 17, 667 (1975); and L. Ilver and P. O. Nilsson, *Solid State Comm.* 18, 677 (1976).
20. L. F. Wagner, Z. Hussain, C. S. Fadley, and R. J. Baird, *Solid St. Comm.*, in press.
21. In essence, this model thus combines the second two steps of the three-step model (transport to the surface and escape from the

surface) into one, and adds the further simplification of a free-electron  $\vec{k}^f$ .

Figure VII-1 - Schematic illustration of the experimental geometry, with various pertinent angles defined. Rotation of the specimen on both axes noted was possible. The angle  $\alpha$  was fixed at  $72^\circ$ .

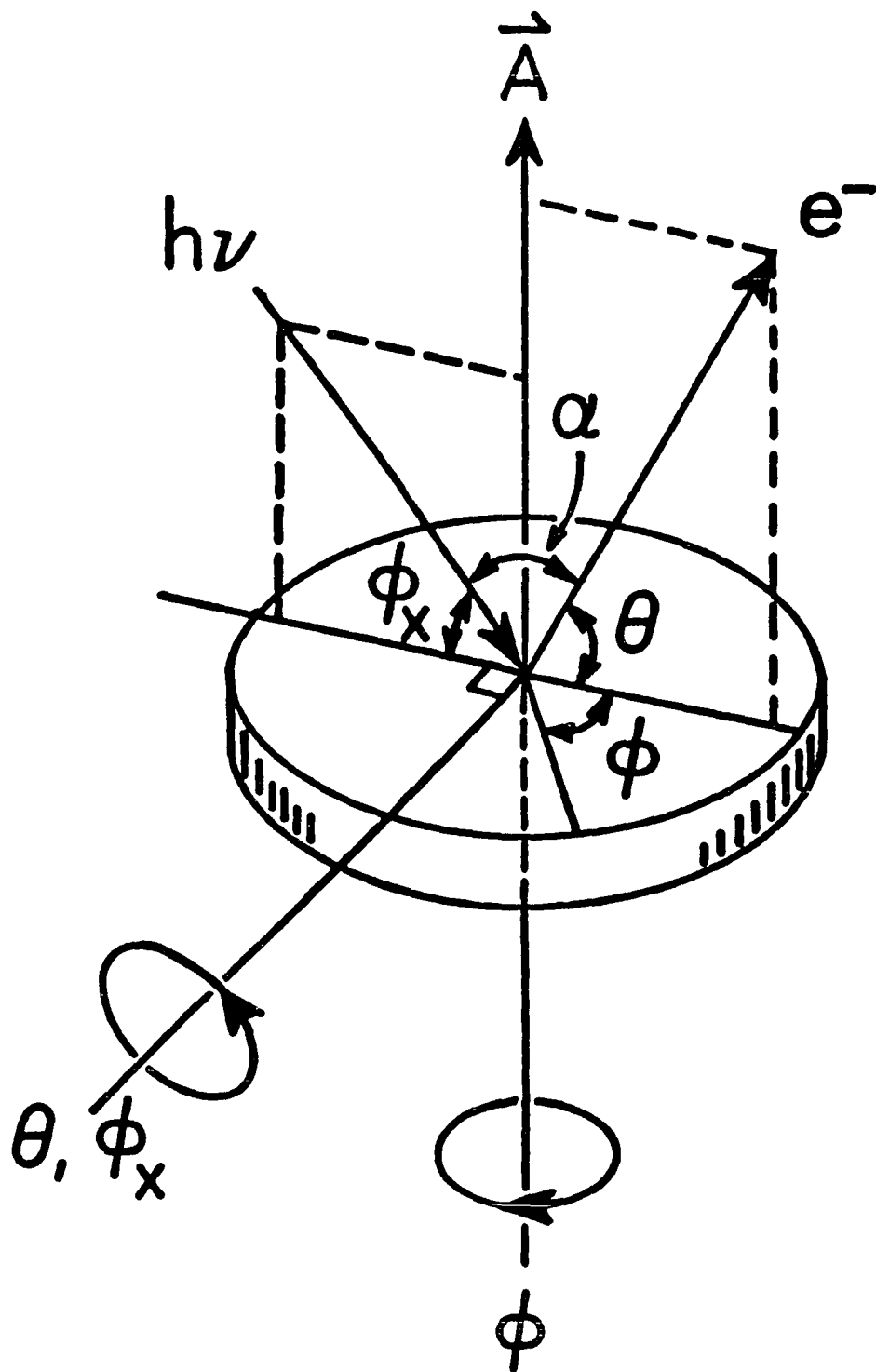


Figure VII-2 - XPS total peak intensities for Au4d-, Au4f- and Au valence-levels as a function of polar emission angle from a single crystal with very nearly [001] orientation.  $\theta$  is defined such that  $90^\circ$  represents emission along the surface normal, and peaks 5 and 10 occur for electron emission along the [001] direction. Results for two different polar-angle scans are shown, with A passing through the [001] and [111] directions and B including the [001] and [011] directions.

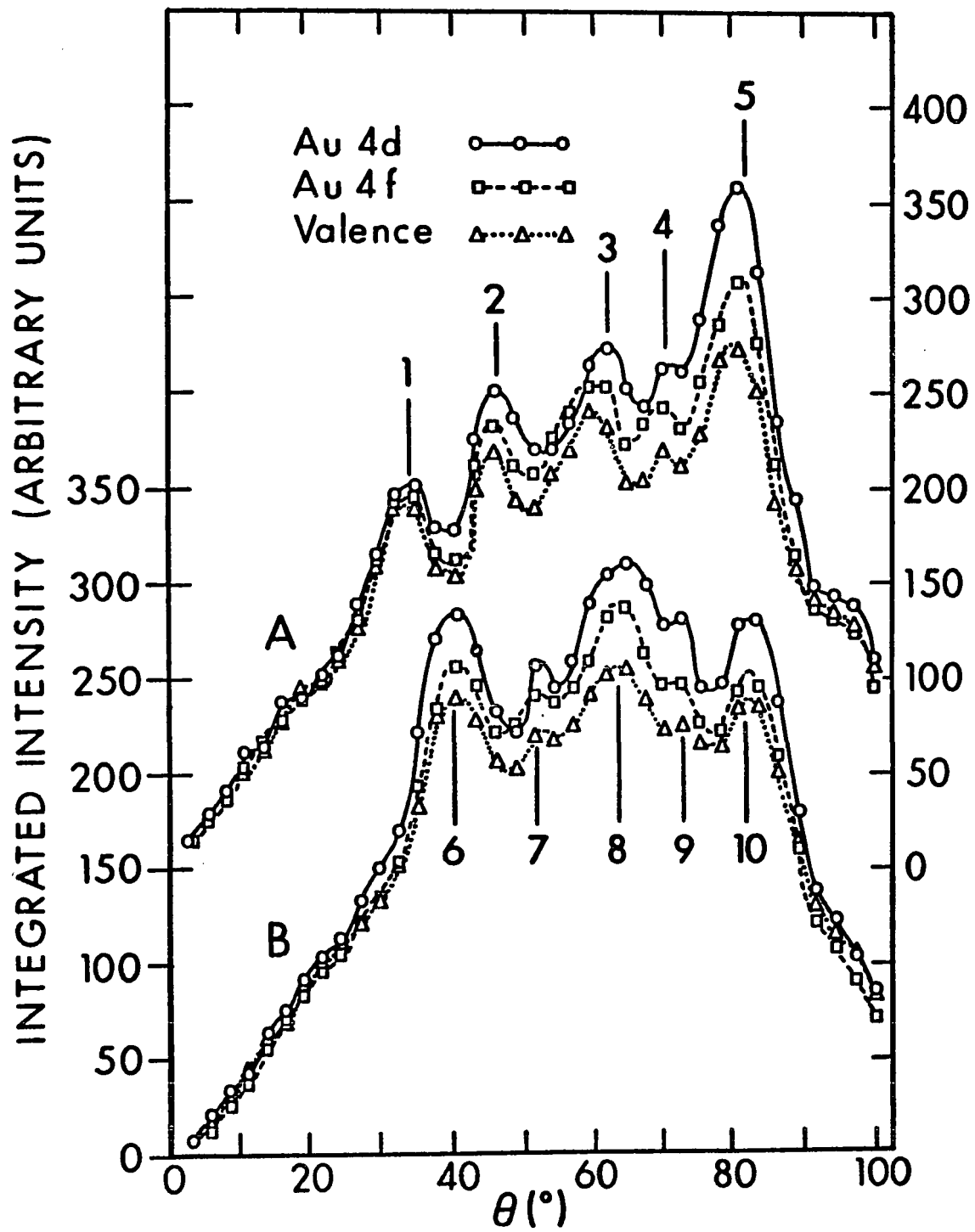


Figure VII-3 - Experimental Au4f XPS intensity contours for the single crystal of Figure 1, shown in stereographic projection. The dotted lines distinguish two sets of data with slightly different total intensities. Various low-index directions and planes are labelled, with [001] offset 9° vertically from the center. Intensity contours are expressed in arbitrary units, with those for 10 and 20 labelled; regions between 22 and 30 are shaded, and regions above 30 are shown in black.

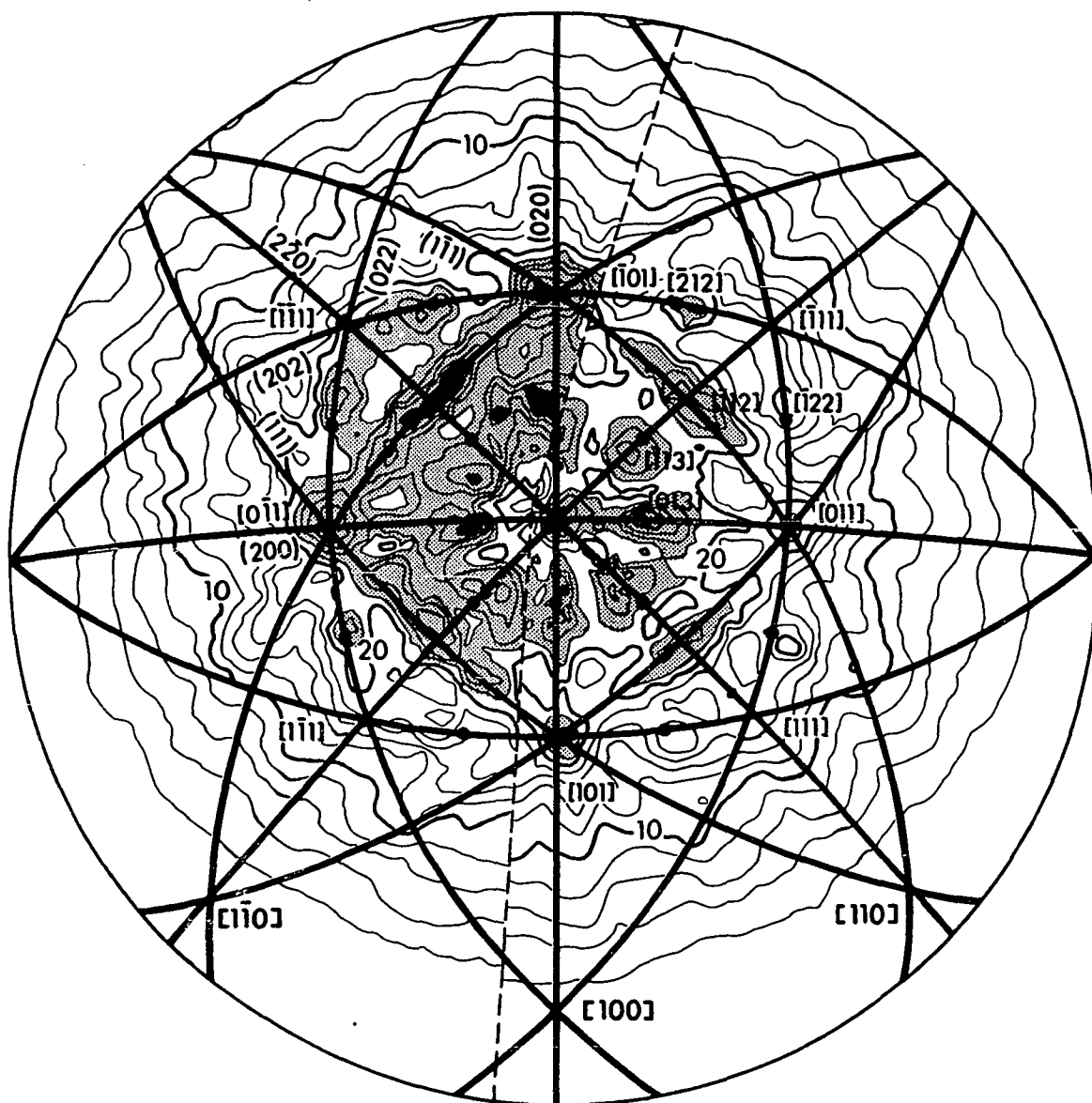


Figure VII-4 - Qualitative predictions of Kikuchi-band theory for the Au4f intensity distribution, also in stereographic projection. Shaded bands  $2\theta_{hkl}$  wide are shown for the principal low-index planes  $\{111\}$ ,  $\{200\}$ , and  $\{220\}$ . The dotted lines in the lower half of the figure indicate the locations of the centers of the bands associated with the higher-index  $\{311\}$  planes; the equivalent bands in the upper half are related by reflection symmetry. Low-index directions are indicated either by specific labels or, for  $\langle 310 \rangle$ ,  $\langle 311 \rangle$ , and  $\langle 221 \rangle$ , by dots at points corresponding to those shown in Figure 3(a).

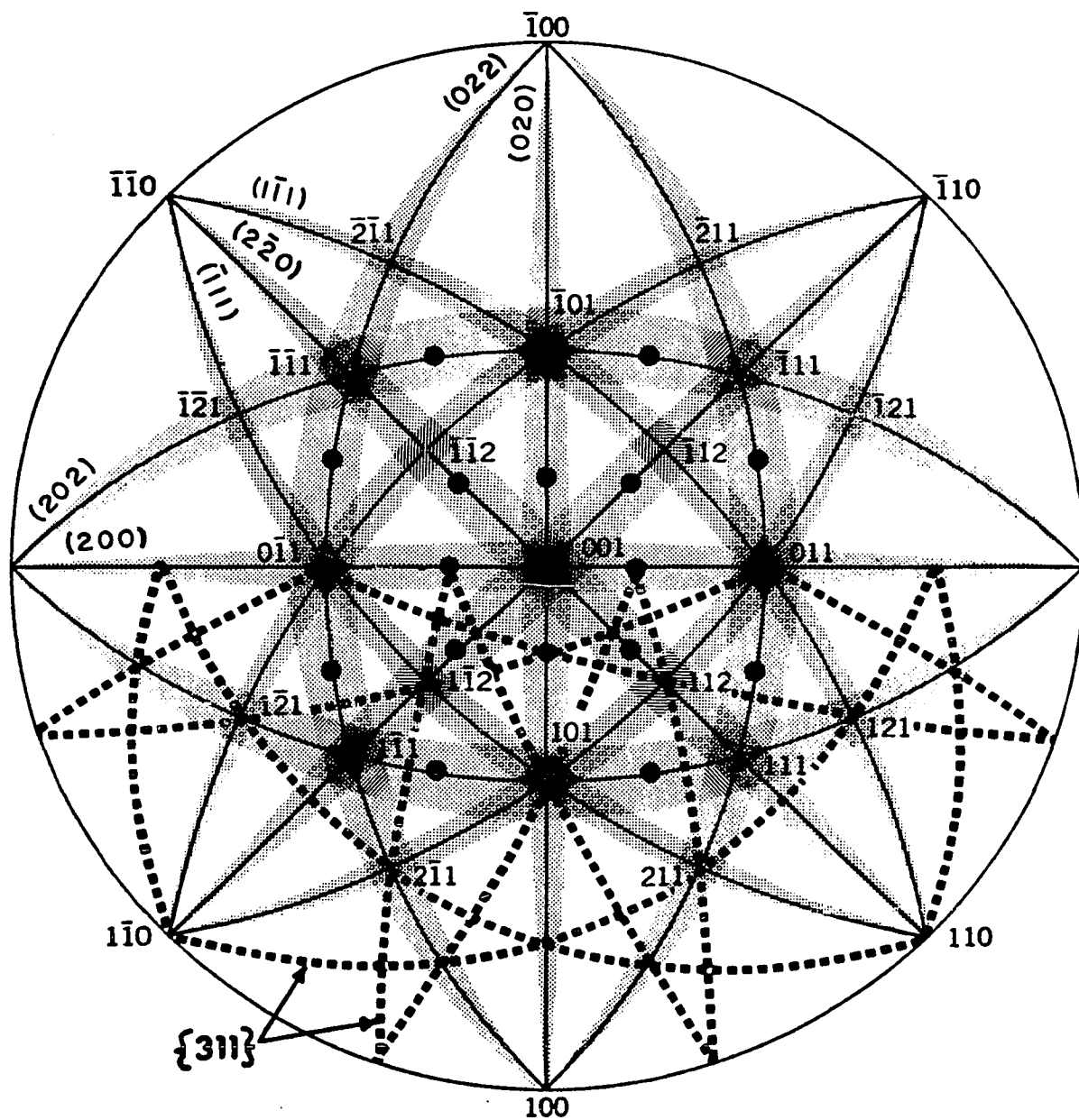
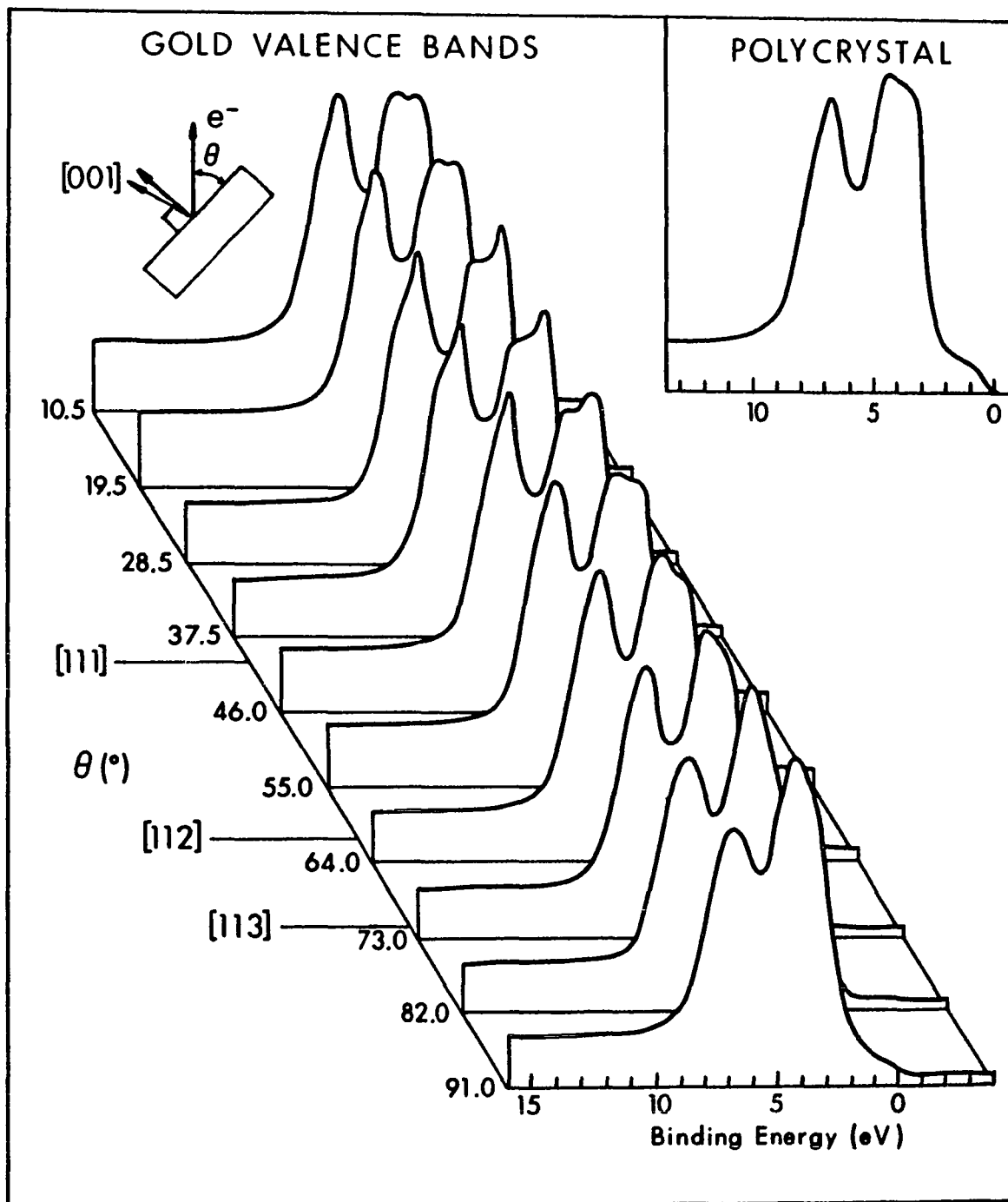


Figure VII-5 - Gold valence-band spectra are shown for various emission angles in a single polar scan. The location of certain low-index directions are indicated, and the scan was made in the same plane as that for curves A in Figure 2. The insert shows a polycrystalline spectrum for comparison. All spectra have been normalized to a constant maximum height. (See also references 3 and 4.)



VIII. ANGULAR DEPENDENCE OF XPS VALENCE  
SPECTRA FROM SINGLE-CRYSTAL GOLD †

We have recently first noted<sup>1</sup> that significant changes occur in valence-level x-ray-photoelectron (XPS) spectra when electron emission is varied from one low-index direction to another in a single crystal, with large differences being observed between Au valence spectra obtained along  $\langle 100 \rangle$  and  $\langle 111 \rangle$  directions. These results have subsequently been confirmed at somewhat lower resolution<sup>2</sup>, and similar effects have been noted in recent preliminary studies of Ag<sup>2</sup>, Cu<sup>3</sup>, Pt<sup>3</sup> and Si<sup>4</sup>. In this letter, we report more detailed observations of such effects in Au, including high-resolution spectra obtained along several directions, and also propose a theoretical explanation of such phenomena in terms of a direct-transition model.

The spectrometer utilized was a Hewlett-Packard 5950A with monochromatized AlK $\alpha$  radiation source (1486.6 eV) modified to permit azimuthal- and polar-specimen rotations in situ<sup>5,6</sup>. Polar rotations were about an axis perpendicular to the plane containing the fixed x-ray-incidence- and electron-exit-directions (separated by an angle of 108°). Resolution loss for operation at polar angles other than that permitting dispersion-compensation<sup>7</sup> was minimized by operating the electrons lens in two different modes<sup>5</sup>. All spectra were obtained under conditions such

† Based on a paper "Angular Dependence of XPS Valence Spectra from Single-Crystal Gold", R. J. Baird, L. F. Wagner, and C. S. Fadley, Phys. Rev. Letters 37, 111 (1976).

that the Au4f<sub>7/2</sub> full width at half maximum intensity (FWHM) was between 0.8 and 1.2 eV. (Single-mode operation yields Au4f<sub>7/2</sub> FWHM of up to 2.3 eV<sup>5</sup>.) All measurements were performed at room temperature and at pressures of 2-4 x 10<sup>-9</sup> torr.

A gold single crystal was mechanically polished with the surface normal tilted 8±1° away from [001] in a direction toward [ $\bar{1}\bar{1}1$ ] and etched in aqua regia to reduce surface disorder. This orientation enabled spectra to be obtained along several different  $\langle 100 \rangle$  and  $\langle 110 \rangle$  directions with reasonable intensity, as the photoelectron current becomes zero for grazing exit angles<sup>5,6</sup>. The only surface contaminant noted was carbon, with Cls/Au4f ratios lying in the range 0.03-0.04 (corresponding to ~1-2 monolayers coverage<sup>8</sup>). Relative photoelectric cross sections<sup>9</sup> thus indicate that the contaminant valence photoelectron intensity was negligible with respect to that of gold. When placed in a separate low energy electron diffraction (LEED) system and subjected to only light ion bombardment so as to remove the carbon present, this crystal gave a LEED pattern characteristic of the basic (001) symmetry. This pattern did not change with annealing. Kikuchi-band-like features in the energy integrated XPS core- and valence-peak intensities<sup>10,11</sup> were used to verify the orientation of the crystal to within ± 1°.

Valence spectra obtained along ten different directions in the crystal are shown in Figure VIII-1. No correction for inelastic scattering has been made. Although the basic two-component peak associated with the Au5d bands<sup>12</sup> is preserved in all spectra, clear differences in the relative intensities of these two peaks are seen, together with changes

in fine structure. Effects primarily associated with the bulk symmetry of the crystal are indicated by the fact that directions fully equivalent with respect to the crystal orientation in the spectrometer geometry (including its relationship to both x-ray-incidence- and electron-exit-directions), give essentially identical spectra; examples of this are [001] and [100], but not [102] and [201] or [101] and [110] (which do show slightly different spectra). The largest changes are observed between the  $\langle 100 \rangle$  and  $\langle 111 \rangle$  directions, for which more detailed spectra are shown in Figure VIII-2 in comparison to a spectrum from a polycrystalline specimen deposited in situ on a glass substrate.

All three experimental spectra in Figure VIII-2 exhibit the same five labelled features A-E, but changes in both relative intensity and position occur. A more quantitative comparison yields these observations:

- (1) For all three cases, the following spectral parameters do not change -- (a) the overall FWHM of the d-band peak, which is 5.3-5.4 eV; (b) the position of the spectrum minimum C, which is at 5.2-5.3 eV below the Fermi energy ( $E_F$ ); (c) the positions of features A and B at 6.4 and 7.2 eV below  $E_F$ , respectively; and (d) the slope of the leading edge of the d-band peak between 1.5 and 2.3 eV below  $E_F$ .
- (2) The two main components within the d-band peak have different relative intensities; as judged by maximum peak heights,  $A + B < D + E$  along [001],  $A + B \approx D + E$  along [111], and  $A + B \lesssim D + E$  in the polycrystalline case.
- (3) Peak D is more intense than peak E along [001], whereas the reverse is true along [111].
- (4) For emission along [111] only, a minimum exists between peaks D and E.
- (5) Relative to the maximum peak height, the

minimum C along [001] is deeper than that along [111]. (6) With respect to the polycrystalline spectrum, features D in the [001] and [111] spectra occur at essentially the same positions, whereas shoulder E in the [001] spectrum and peak E in the [111] spectrum are shifted to lower binding energies by approximately 0.3 3V (cf. also the [100] spectrum in Figure VIII-1).

These results can be explained in terms of a direct-transition model closely related to that utilized in interpreting angular-dependent ultraviolet-photoemission (UPS) data from single crystals of several materials<sup>13-15</sup>, including Au<sup>15</sup>. Wave-vector conservation in the photoemission process is assumed, so that  $\vec{k}^i + \vec{g} + \vec{k}_{h\nu} = \vec{k}^f$ , in which  $\vec{k}^i$  is the initial-state wave vector in a reduced-zone representation,  $\vec{g}$  is a reciprocal lattice vector,  $\vec{k}_{h\nu}$  is the photon wave vector, and  $\vec{k}^f$  is the wave vector of the photoelectron. The high photon energy in the XPS experiment implies that: (a)  $\vec{k}_{h\nu}$  cannot be omitted from the conservation equation as it is in UPS. For example, for AlK $_{\alpha}$  radiation,  $\vec{k}_{h\nu} = 0.49 (2\pi/a)$ , with  $2\pi/a \approx$  mean Au Brilluoin zone radius. (The inclusion of  $\vec{k}_{h\nu}$  prevents [102] and [201], as well as [101] and [110], from being equivalent in Figure VIII-1). (b) To a good approximation,  $\vec{k}^f$  can be assumed to be associated with a pure free-electron state. Secondary bulk-<sup>10,11,13</sup> or surface-<sup>13</sup>scattering events are thus also neglected. (c)  $\vec{k}^f$  changes very little in magnitude over the valence spectrum ( $12.84(2\pi/a) \leq \vec{k}^f \leq 12.88(2\pi/a)$ ). (d) Electron refraction at the surface is negligible for the exit angles considered here<sup>6</sup>.

The finite acceptance solid angle of the spectrometer (a cone of  $3.5^\circ$  half angle) distributes the observed  $\vec{k}^f$  values over an essentially planar, circular disc of radius  $0.78(2\pi/a)$ . The projection of this disc into the reduced zone with appropriate  $\vec{g} + \vec{k}_{h\nu}$  values specifies the set of  $\vec{k}_i$ 's contributing to photoemission. If matrix-element variations over these  $\vec{k}_i$  values are assumed small, the photoelectron spectrum will be proportional to the density of states on the projected disc. Utilizing the RAPW Au band structure of Christensen and Seraphin<sup>16</sup>, we have calculated such densities of states for emission along [001] and [111] directions. In addition, the density of states appropriate to an experiment on a polycrystalline specimen was calculated by permitting  $\vec{k}^f$  to have all directions with respect to the crystal axes. Finally, the total density of states as integrated over the complete zone was determined.

The results of these calculations (convoluted with a Gaussian of 0.80 eV FWHM to simulate minimum instrumental broadening) are shown in Figure VIII-2 together with the relevant experimental spectra. The experimental similarities and differences noted previously in items 1-6 are all qualitatively predicted by theory. The theoretical curves are completely consistent with observations 1, 3, and 5, as well as with the direction of the relative intensity change between [001] and [111] noted in item 2. The minimum between peaks D and E along [111] (item 4) is also predicted by theory, although an additional lower-intensity peak F is also found in both the [001] and [111] curves. However, peaks F and D may be highly overlapping in the [111] experimental spectrum, and in

fact a slight shoulder is observed near the predicted location for peak F. The relative energy shifts of features D and E in the [111] spectrum (item 6) are also predicted to be in the correct directions and of approximately the correct magnitudes if it is assumed that peaks F and D are overlapping. The direction of the shift of shoulder E in the [001] spectrum is also correctly indicated. The only minor point of disagreement is that the theoretical [001] curve indicates a shift of peak D to lower energy that is not found experimentally.

The polycrystalline theoretical curve differs very little from the total density of states. This result is consistent with prior XPS studies in which polycrystalline spectra have been compared to total densities of states<sup>12</sup>, but it also indicates for the first time that such comparisons are possible in the limit of rigorous  $\vec{k}$  conservation. Comparing experiment and theory for the polycrystalline specimen indicates that the A + B component is too intense relative to D + E in the theoretical curves, a discrepancy which has been noted in prior comparisons for gold<sup>12</sup>, and which is also qualitatively found in our results for both the [001] and [111] directions. Features A and B are also not as widely separated in the theoretical curves as they are in the experimental spectra, an effect which could be due to the particular band structure calculation utilized<sup>12</sup>. Because we are concerned primarily with predicting similarities or differences between spectra, neither of these discrepancies affects the previous discussion.

Additional factors which must be considered in making a more quantitative comparison of theory and experiment are: (a) Crystal alignment

errors in the experimental system -- the fine structure in theoretical curves is found to be weakly sensitive to changes of  $\sim \pm 2^\circ$  in the orientation of  $\vec{k}^f$  with respect to the crystal directions, although the basic shapes of the curves are preserved in such changes. (b) Effects due to secondary scattering -- these effects<sup>10,11,13</sup> would tend to make the experimental spectrum reflect more of a zone-averaged behavior, and may account for the fact that the differences between experimental spectra are in general less than those predicted by theory. The presence of Kikuchi-like fine structure in the angular distribution of integrated valence intensity which is essentially identical to that for high-lying core levels<sup>10,11</sup> also suggests that secondary scattering is not completely negligible. (c) Neglect of matrix-element variations -- McFeely et al.<sup>2</sup> have recently proposed an alternative explanation for such angular-dependent XPS valence spectra that considers only zone-averaged matrix elements for tight-binding d orbitals. It was predicted that only  $e_g$  character can be active along  $\langle 100 \rangle$  and only  $t_{2g}$  along  $\langle 111 \rangle$ , and partial densities of states for  $e_g$  and  $t_{2g}$  were compared respectively with a Au [001] spectrum obtained at much lower resolution than those shown in Figures VIII-1 and VIII-2 (Au4f<sub>7/2</sub> FWHM  $\approx 2.0$  eV), and with a [111] spectrum in good agreement with the present data. The theoretical results are in qualitative agreement with our observations 1(b), 1(c), 2, and 4, but significantly disagree with 1(a), 1(d), 3, 5, and 6. Thus, although some type of matrix-element anisotropy certainly may play a role in producing such angular-dependent spectra, the wave-vector selectivity of the direct-transition model is by itself much better able

to account for all of the experimental observations for gold.

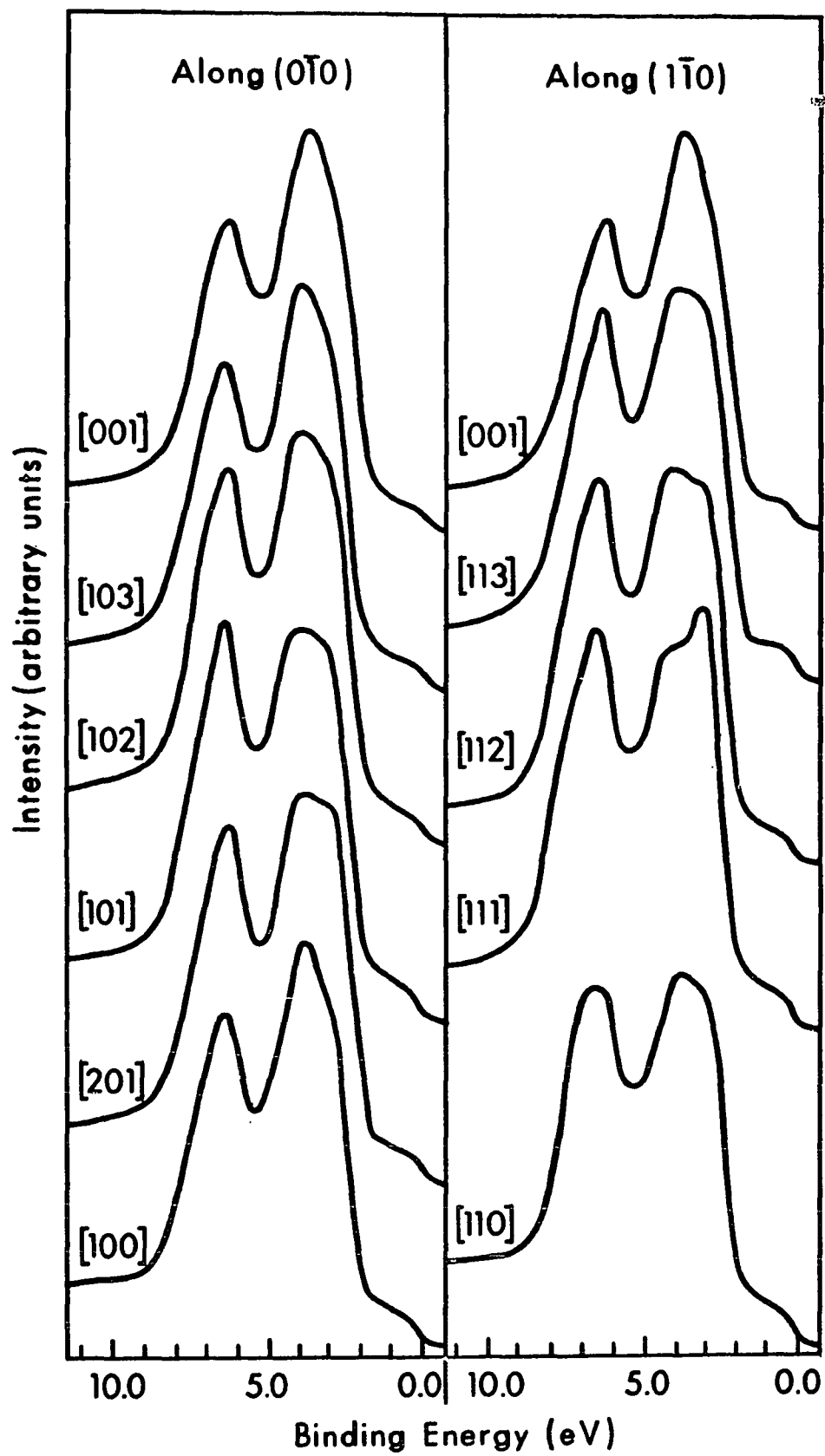
In conclusion, the angular-dependent changes noted in XPS valence spectra from single-crystal gold are qualitatively very well explained in terms of a straightforward extension of the direct-transition model. Such studies thus should provide another method for mapping energy-band characteristics throughout the Brillouin zone.

REFERENCES  
SECTION VIII.

1. R. J. Baird, C. S. Fadley, and L. F. Wagner, to appear in Faraday Discussion No. 60 (1976).
2. F. R. McFeely, J. Stöhr, G. Apai, P. S. Wehner, and D. A. Shirley, private communication.
3. Z. Hussain, L. F. Wagner, and C. S. Fadley, to be published.
4. N. E. Erickson, private communication.
5. R. J. Baird and C. S. Fadley, paper presented at the Northwest Regional Meeting of the American Chemical Society, Honolulu, June, 1975, and to be published.
6. C. S. Fadley, to appear in Progress in Solid State Chemistry, G. A. Samorjai and J. O. McCaldin, Eds1, Pergamon Press, New York, 1976, Volume 11, Part 3.
7. K. Siegbahn, D. Hammond, H. Fellner-Feldegg, and E. F. Barnett, Sience, 176, no. 7032, 245 (1972).
8. M. Mehta and C. S. Fadley, Phys. Lett. 55A , 59 (1975).
9. J. H. Scofield, Lawrence Livermore Laboratory, Report No. UCRL-51326 (1973).
10. C. S. Fadley and S. Å. L. Bergström, Phys. Lett. 35A, 375 (1971), and in Electron Spectroscopy, D. A. Shirley, Ed., North Holland Pub. Co., Amsterdam, 1972, p. 233.
11. R. J. Baird, C. S. Fadley, and L. F. Wagner, to be published.
12. D. A. Shirley, Phys. Rev. B5, 4709 (1972); R. A. Pollak, S. A. Kowalczyk, L. Ley and D. A. Shirley, Phys. Lett. 41A, 455 (1972).

13. G. D. Mahan, Phys. Rev. B2, 4334 (1970); W. L. Schaich and N. W. Ashcroft, Phys. Rev. B3, 2452 (1971).
14. T. Gustafsson, P. O. Nilsson, and L. Wallden, Phys. Rev. Lett. 37A, 121 (1971); B. Feuerbacher and B. Fitton, Phys. Rev. Lett. 30, 923 (1973); M. M. Traum, N. V. Smith and F. J. Disalvo, Phys. Rev. Lett. 32, 1241 (1974); and references therein.
15. P. O. Nilsson and L. Ilver, Solid State Comm. 17, 667 (1975); and references therein.
16. N. E. Christensen and B. O. Seraphin, Phys. Rev. B4, 3321 (1972).

Figure VIII-1 - XPS valence spectra for electron emission along various low-index directions from a gold single crystal with approximately (001) orientation. The two sets of spectra were obtained by sweeping the emission direction in a  $(0\bar{1}0)$  plane and a  $(1\bar{1}0)$  plane.



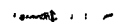
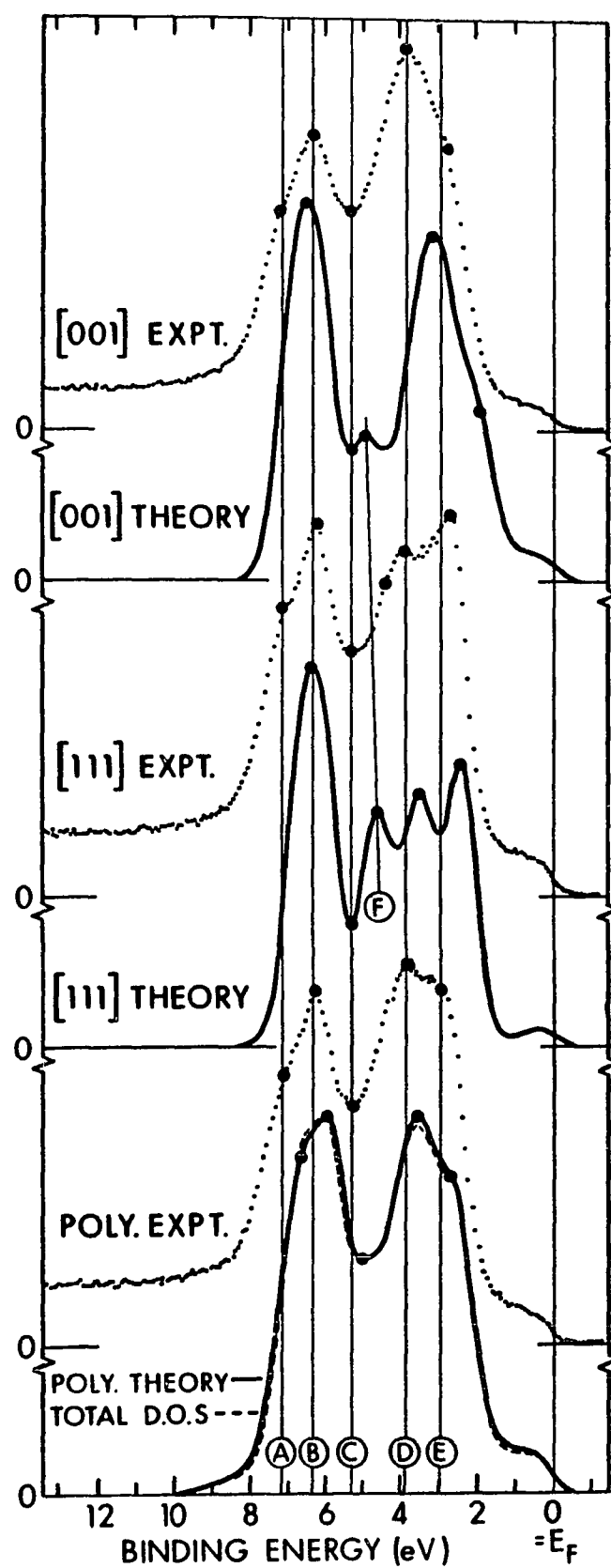


Figure VIII-2 - XPS valence spectra for the [001] direction, the [111] direction, and a polycrystalline specimen are compared to densities of states calculated over  $\vec{k}^1$  values allowed by the direct-transition model and to a theoretical total density of states.



## IX. CONCLUSIONS

In several ways angular-dependent photoemission studies have been shown to add another useful dimension to x-ray photoelectron spectroscopy. As discussed in Section II and demonstrated in section IV, instrumental effects on both intensity and linewidth must be well understood and carefully characterized in order to carry out well-defined angle-resolved measurements. However, the cancellation of the angle-dependent instrument response function in intensity-ratio measurements allows useful angular-distribution studies to be performed on spectrometer systems for which the response function is not known. The effects of sample surface roughness on angular-distribution measurements have been shown to be potentially very significant. Therefore, great care in sample preparation is required for quantitative angular-distribution studies, but since some surface enhancement has always been obtained at very low angles of electron emission, qualitative surface composition measurements appear to be possible even in the presence of surface roughness.

The ability to vary the effective depth of sampling in XPS angular-distribution studies also provides a sensitive method for investigating the depth dependence of inelastic loss processes of electrons in solids. In the study carried out on a free-electron-like metal, it was possible to selectively enhance either the surface- or bulk-plasmon contributions to the inelastic loss spectrum, thus allowing for direct and detailed comparisons between theory and experiment. This separation of bulk- and

surface-loss mechanisms further permits the depth of penetration of a surface-adsorbed atom to be estimated from its loss spectrum.

In applications to single-crystal specimens, angle-resolved x-ray photoemission studies have been shown to provide information about the interaction of the exiting electrons with the crystal lattice via multiple-scattering processes closely related to Kikuchi bands. These effects on total peak intensity measurements also provide an unambiguous method for establishing crystal orientation relative to the spectrometer for other experiments in which this orientation is significant. Also, angle-resolved studies of valence-band spectra have been found to exhibit pronounced changes in fine-structure that have been related to direct transition effects; such measurements thus provide an experimental method for probing the  $\vec{k}$  dependence of the valence-band density of states.

In summary, angle-resolved XPS has proven to be a powerful technique for probing the surface composition and electronic structure of solids, and its future application to a broad range of studies seems likely.